Recent Trends

in Charged Particle Optics and Surface Physics Instrumentation

Proceedings

of the 9th International Seminar,
held in Skalský dvůr near Brno, Czech Republic,
from July 12 to 16, 2004,
organised by
the Institute of Scientific Instruments AS CR and
the Czechoslovak Microscopy Society

held in honour of Professor Armin Delong
on the occasion of his 80th birthday

Edited by Ilona Müllerová

Published and distributed by the Institute of Scientific Instruments AS CR.
Technical editing by Marek Frank, printed by CCB Brno, Czech Republic.

ISBN 80-239-3246-2

Professor Armin Delong

PREFACE

Two years have elapsed, and once again we have the pleasure of welcoming participants to the Recent Trends seminar – the ninth in the series. From one point of view this seminar is to differ from those that have gone before, since we have taken the liberty of holding the meeting in honour of Professor Armin Delong on the occasion of his 80th birthday.

Professor Armin Delong was born on 29 January 1925 and began his career as one of a group of three students who built the first Czech electron microscope in 1950. Soon afterwards he became a leading light in the electron microscopy community in this country and enjoyed wide-ranging connections abroad. For nearly thirty years, between 1961 and 1990, he was director of our institute. During this time an unbelievably extensive range of original projects were undertaken in the fields of electron optics and microscopy with great success, either with his personal participation or at least at his initiative. From my perspective as his pupil (something of which I will always be extremely proud) another aspect seems equally, if not more, important – under his leadership the Institute of Scientific Instruments was for decades a shining island in a surrounding sea of repression of the intellectual life of a society dispossessed of its political freedom.

Eight is surely the roundest of numbers, so an eightieth birthday may also seem the "roundest", and the one most worthy of celebration. This is surely particularly true of the birthday of a man who remains creative to this day and shows no respect for his own oft-repeated tenet that "innovations can only be produced by those still young enough not to have learned that what they are aiming for is impossible". He learnt this long ago, but it doesn't seem to bother him.

In the first session of the seminar, explicitly dedicated to Professor Delong, we will have the pleasure of hearing about his recent developments and plans for the future. A number of us will also be adding comments and memories of our work with him and our shared experiences.

In other respects we are, at first glance at least, meeting up in an atmosphere not so very different from that at our previous gatherings. Can this really be true, when just a short time ago the Czech Republic finally joined the European Union? Perhaps greater changes will be seen in the everyday life of Czech scientists over the long term. So far all that has changed is that new administrative complications have been added to the huge number that already existed to burden the managers of scientific institutions. It seems that, for scientists at least, the crucial event was the fall of the Iron Curtain, after which things began to develop spontaneously of their own accord, as a result of which we have already felt ourselves to be part of the European scientific community for years. Hopefully the act of crossing the Czech border this time was simpler and a bit more pleasant for our foreign participants than it was before.

One other aspect should, however, be mentioned here. In the past, in a divided world, we Czechs often profited from various forms of help from our colleagues in the European Union, so we should ourselves now be ready to help those from less fortunate countries, or at least from countries that are experiencing a fate similar to our own, i.e. countries in which restrictions and a lack of freedom have been imported and supported from the outside. Hopefully next time we will be able to offer some financial support for the participation of young researchers from the third-world.

This brochure is being distributed to seminar participants on arrival, and this gives me the opportunity to thank them for including this event in their diaries, already so full of commitments and higher profile meetings, and to wish them a pleasant and fruitful week in the Highlands of Bohemia and Moravia.

Luděk Frank

CONTENTS

HUMIDITY MEASUREMENT AND ADJUSTMENT AT ENVIRONMENTAL CONDITIONS

Rudolf Autrata [a], Josef Jirák [a,b], Vilém Neděla [a], Jiří Špinka [a,b]

[a] Institute of Scientific Instruments AS CR, Královopolská 147, 612 64 Brno, Czech Republic
[b] Department of Electrotechnology, Faculty of Electrical Engineering and Communication, BUT Údolní 53, 602 00 Brno, Czech Republic, fax. +420 541 146 147,
e-mail: spinka@feec.vutbr.cz

When we are detecting signal electrons with an ionization detector in ESEM, the most advantageous is to use, with respect to the effectiveness of ionization, environment of water vapours in the specimen chamber. The most suitable are saturated water vapours (relative humidity of 100%). This environment is also advantageous for observation of specimens containing water. At pumping of the specimen chamber to the working pressure (typically around 1000 Pa), in the case of wet specimens, evaporation of specimen can occur, or on the contrary, condensation of water on them. It means, that in some cases the specimen will not remain in the original state. That is why we try to adjust and optimize the pumping procedure and pumping of water vapors to minimize deformation of the observed specimens.

For optimization of the pumping procedure we need to obtain information about amount of vapour in the vicinity of the specimen. To measure humidity of the environment the most common method used is the mechanism of absorption of water into polymer materials [1]. Impedance sensors, capacity sensors or sensors based on the measurement of changes of mechanical properties are used, as well as other types.

Impedance sensors use a polymer structure to which hydrophilic ions are bound, whose charge is compensated by opposite ions. When humidity is increased hydrophilic particles absorb water. A typical representative of such a material is Nafion as a cation exchanger with firmly bound sulpho groups, while hydrogen ions are the contraions. The impedance is then measured at an alternating current. The changes of the impedance of the detector can be up several orders. The dependence of the impedance on the humidity of the environment is usually non-linear, and such sensors show certain hysteresis.

Capacity sensors use a hydrophobic polymer as dielectric (a material with small permittivity is chosen) of the capacitor. Even a small amount of water absorbed on the surface of the detector, with regards to the high permittivity of water ($\varepsilon_r = 80$), significantly changes the permittivity of the configuration and, consequently, the capacity of the sensor. This dependence is linear. Polyamides or derivates of cellulose are used the most frequently.

The sensors based on changes of mechanical properties contain a polymer, e.g. polyvinylalcohol and finely dispersed carbon particles. Changes in volume of the polymer due to moistening or drying up, result in a change of ohmic resistance between conductive grains of carbon *(swelling-type sensors).* This resistance is then measured. Mechanical changes caused by change of humidity are also used in piezo-resistor sensors.

For our purposes we used the capacity sensor [2] equipped with a sensor for temperature measurement. All device is electronically controlled via a microprocessor. The output signal is voltage.

For optimization of the pumping and filling-in processes we utilized studies [3,4]. Temperature of water in the vapour developer, number of repetitions of cycles of pumping and filling-in water vapor, range of pressures used for cyclical pumping and filling-in water vapors as well as the level of initial humidity in the specimen chamber, all have influence on the pumping process. The lower is the temperature of the specimen, the better is the final result of the pumping process. However, it cannot be lower than the temperature at which water

condensates on the surface. The temperature of water in the vapor source is another important parameter of the pumping process. At intensive water evaporation intensive cooling occurs and it is not possible to achieve higher pressures, which is typical for work at pressures over 950 Pa. Thus it is important to ensure that the container of water is heated to a temperature over 23°C.

The range of maximal and minimal pressures when cycling (see the Fig.1) also has a significant influence on the resulting humidity in the specimen chamber. It is important to finish pumping at a pressure over the value of 609 Pa, which is a minimal pressure for keeping water in liquid state at 0°C. For comparison we have chosen pumping to the values of minimal pressures of 700 Pa, 800 Pa, 900 Pa. It is evident from the measurement results, that the best value is achieved at circulation in the range of 700 – 1100 Pa. For pressures in the range of 800 – 1100 Pa and 900 – 1100 we did not achieve such a humidity level as in the former case.

From the above-mentioned findings an optimum pumping procedure can be suggested. It consists of the following steps:

1. Inject a small amount of water before pumping of the specimen chamber (in our case for a volume of specimen chamber $2{,}8.10^{-3}$ m^3 is used a volume of 0.5 ml of water).
2. Close the chamber, then start pumping. Evaporation of water starts and will continue until the level of original humidity in the specimen chamber is achieved. After the evaporation of the water droplet the pressure begins to decrease. The pumping proceeds to the moment, when the pressure decreases to 700 Pa.
3. After achieving of 700 Pa open the irrigation valve and fill in water vapour from the developer to the chamber. The pressure increases. Fill in water vapour until pressure of 1100 Pa is achieved.
4. Repeat steps 2 and 3 at least four times, which should be adequate to achieve sufficient humidity.

This regime should create an environment of saturated water vapors and enable work with water containing specimens in order to prevent any significant changes and damage.

Fig.1 **Pumping cycle**

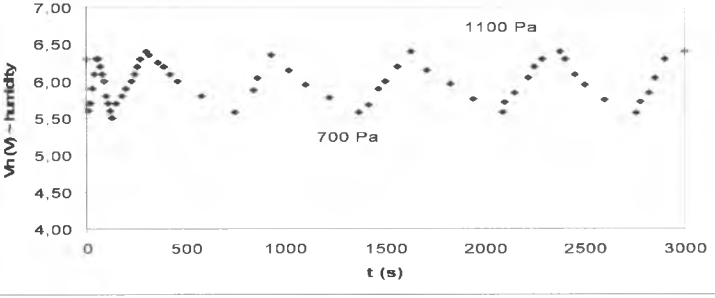

[1] Hrnčíková, P. – Opekar, F.: Senzory s tuhými polymery, Chemické listy 2000, p. 338-342.

[2] http://www.cometsystem.cz

[3] Cameron, R. E. – Donald, A. M.: Minimizing Sample Evaporation in the Environmental Scanning Electron Microscope, Journal of Microscopy Vol. 173, 1994, p. 227–237.

[4] Franz, N., Timm U., Hohenberg H.: Monitoring and Analysis of the Environmental for Biomaterials in the ESEM under „Wett Mode" Conditions, Microscopy and Microanalysis, 9, 2003, p.124-129.

This work was supported by the grant MSM 262200010.

OPTIMIZATION OF HYDRATION CONDITIONS IN ESEM

R. Autrata, V. Neděla

Institute of Scientific Instruments ASCR, Královopolská 147 Brno, Czech Republic, vilem@isibrno.cz

It is known, that study of samples containing big amount of water, e.g. soft biological tissues, can be realised by the technique of environmental scanning electron microscopy. This technique enables one to use high pressure of water vapour in the specimen chamber (10^3 Pa) and it thus creates conditions for minimization of water evaporation from the sample, the detection of signal electrons with sufficient efficiency and neutralization of a charge originating on the surface of insulation samples. Study of biological specimens of soft tissues with fine and very fine hydrated structure still remains a big problem because this structure can be easily damaged by dehydration during the initiating phase of vacuum pumping of a microscope. The attention is thus focused on setting up the conditions for complete dehydration of samples, ensuring the nature state of a sample during the critical phase of pumping of a microscope. Such conditions can be created by respecting the physical dependence of pressure of saturated water vapours on temperature, which is depicted by a curve presented in Fig. 1, and using special methods (water-containing gels, a chamber with a membrane, etc.), which minimize deviations of wetness in the vicinity of a specimen. Violation of the conditions presented in Fig. 1 leads to dehydration of a sample or to coating the surface topography of a specimen by water. These states are presented in Fig. 2., which presents a partially dried specimen of small intestine tissue, on which forming water drops are visible as a consequence of a condensation process and a beginning of coating the specimen with water.

A method of cyclical irrigation of the specimen chamber is one of the methods which preserve prolongation of a relatively natural state of a soft tissue sample. Experimentally set up amount of distilled water (approx. 0.5 ml for chamber of AQUASEM microscope) is inserted into the specimen chamber before the beginning of the pumping process. The pumping of the specimen chamber goes through the pressure limiting aperture, which separates the chamber of differential pumping from the specimen chamber. This pumping is accompanied by a decrease of the pressure down to the value of a pressure of saturated water vapours (2062 Pa) corresponding with a temperature of distilled water in the specimen chamber (18°C). Another decrease of the pressure in the specimen chamber occurs after evaporation of distilled water. In that moment filling-in of water vapour must start from the external reservoir of water, regulated by a valve. In order to achieve stabile high relative wetness in the specimen chamber, it is necessary to repeat the irrigation process several times.

Another method is based on observation of wet tissues placed on a special support from agar, whose area is a sufficient supplier of water, which gradually evaporates and thus hydrates the specimen. [1]. The agar successfully minimizes the influence of dehydration deviations on the observed specimen and, in connection with a method of cyclical irrigation of specimen chamber, creates a very good means of observation of biological tissues in ESEM. It is demonstrated in Fig. 3, in which samples of small intestine tissue observed at equal temperatures and pressures in the ESEM chamber are presented. The upper parts of figure Fig. 3 (a, b, c) presents samples placed on a classical cooled specimen holder and the samples placed on a special cooled agar base are shown in the bottom parts of Fig. 3 (d, e, f). It is

noticeable from Fig. 3 that samples placed on the agar support show (at the same values of temperature and pressure as in the case of samples placed on a classical holder) minimum damage of surface structure caused by dehydration.

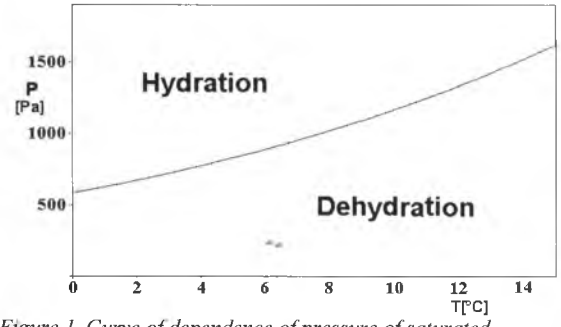

Figure 1. Curve of dependence of pressure of saturated water vapours on temperature

Figure 2. Water drops as a consequence of violation of conditions set up in Fig. 1

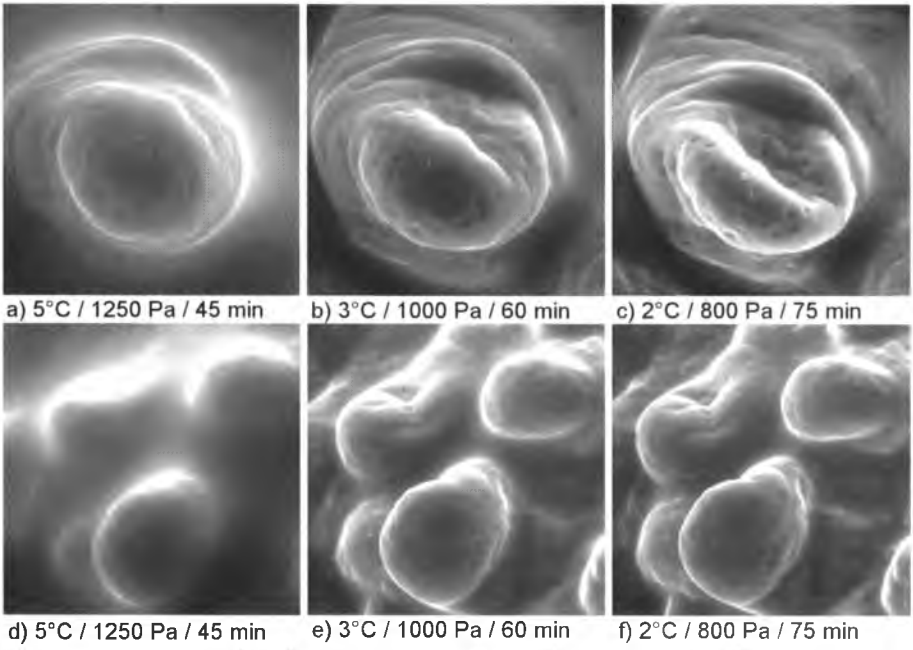

Figure 3. Sample of small intestine placed on a classical specimen holder (upper figures) and on a special base from agar (bottom figures) in ESEM. Mag. 800X

[1] Sanger, P., Ritter, M., Hohenberg, H.: Water Reservoir (Matrice) prezent Rapid Dehydration of Native Samples in the Environmental Scanning elektron Microscope (ESEM), Microscopy Conference 2003, Dresden, Germany, September 2003, Proceedings, 494-495.

This work was supported by Academy of Sciences of the Czech Republic, grant No. S2065102 and grant KSK2067107.

NEW TYPE OF YAG-II SCINTILLATOR FOR NANORESOLUTION BSE IMAGING IN SEM

R. Autrata, P. Schauer, P. Wandrol

Institute of Scientific Instruments, AS CR, Brno, Czech Republic, wandrol@isibrno.cz

Detection of backscattered electrons (BSE) in scanning electron microscopy (SEM) serves as an auxiliary method in the study of surfaces and composition of materials. Backscattered electrons have properties that are different from those of usually used secondary electrons. The achievement of the theoretical limit of resolution (0.6 – 0.8 nm for SE and 0.9 nm for BSE) depends not only on the properties of the electron source, properties of electron optics, specimen preparation technique, type of electrons, but also on the detection system efficiency.

Several types of detection systems have been designed for detecting signal electrons in SEM. Even though in the last few years the noise and time characteristics of semiconductor detectors and the properties of channel plate detectors have been considerably improved and even though a great number of SEMs are equipped with semiconductor detectors to detect BSEs, the scintillator-photomultiplier still possesses the best signal-to-noise ratio and bandwidth characteristics [1] The most important part of such system is the scintillator. Powder P47 and yttrium aluminium garnet (YAG) single crystal are the most efficient scintillators even if powder material of P47 is suitable only for SE detectors.

It was shown [2] that BSE detectors based on YAG single crystal enable to achieve very high detection quantum efficiency (app 0.75 at 10 keV). The efficiency of the YAG – BSE detector depends not only on the optical properties of the whole detector system but also (and especially) on the efficiency of electron – photon transfer in a scintillator. This efficiency is the limiting factor for the achievement of a high BSE resolution.

Working out technology of the preparation of the YAG scintillator with the highest light output after an impact of BSEs was our aim.

For crystal growth a small volume of water vapour in the growth atmosphere was used. Due to the additional treatment of the YAG discs in oxygen and hydrogen atmosphere at very high temperatures, the colour centres in the YAG crystal lattice were suppressed. Polishing process of the YAG surface was improved. It was found that this process caused penetration of the polishing microparticles into the surfaced microcracs. These particles can be removed by the washing process in a special mixture of acids only at a suitable temperature.

Thanks to these steps, the light output from the modified scintillator was increased about double times, in comparison with the older YAG (type I). The decay time 1/e was decreased and moves in the range 60-70 ns. Long time afterglow is also shorter.

The modified single crystal, named as YAG II scintillator, was used to design the planar YAG-BSE detector that is tightly placed under the pole piece of the SEM.A smaller hole in the centre of the YAG has been used for the reason of higher collection of BSEs trajectories. DQE coefficient of this detector was increased from the original value 0.75 at 10keV to 0.85 at 10keV.

Thanks to the improved properties of the YAG-BSE detector, it was possible to operate with lower PMT amplification, lower beam current and lower accelerating voltage. All these conditions are suitable for the receiving of higher BSE image resolution.

[1] R. Autrata, R. Hermann, M. Müller, An efficient single crystal detector in SEM, Scanning 14 (1992), 127-135

[2] R. Autrata, P. Schauer, Single crystal scintillator detectors for LVSEM, Proc. 14th International Congress EM, Cancun (1998) 437-438

[3] This work was supported by Academy of Sciences of the Czech Republic, grant No. S2065102.

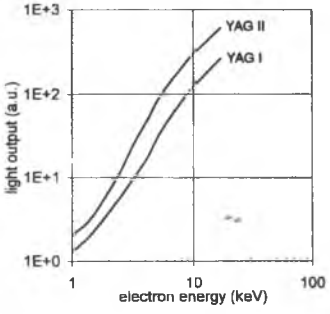

Figure 1. Relative light output of single crystals versus energy of incident electrons.

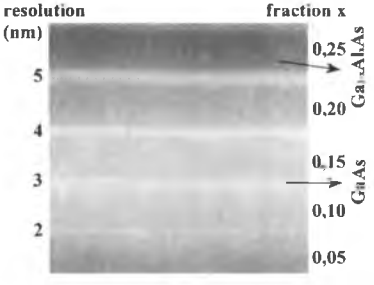

Figure 2. Superlattice structure of GaAs and $Ga_{1-x}Al_xAs$ recorded with planar YAG-BSE deteetor.

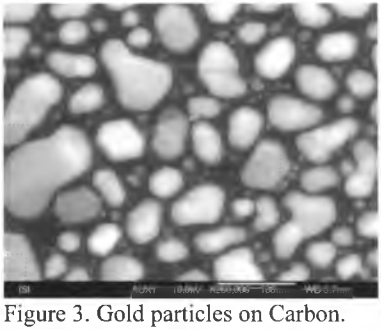

Figure 3. Gold particles on Carbon.

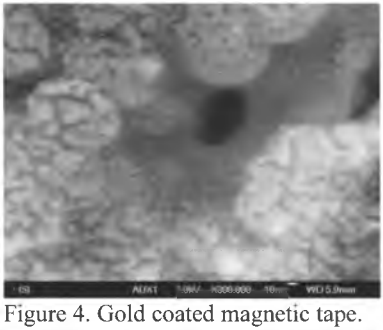

Figure 4. Gold coated magnetic tape.

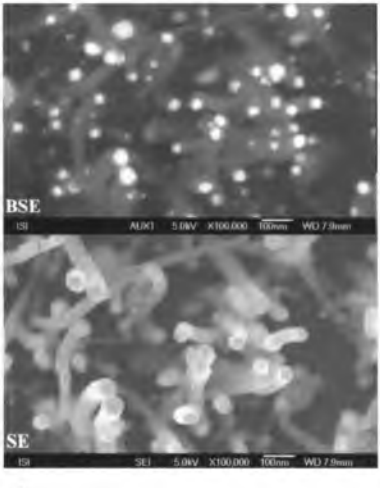

Figure 5. Carbon nanotubes.

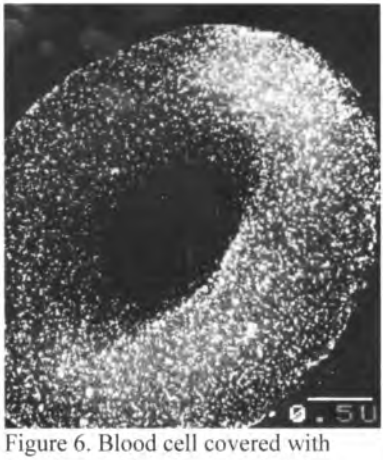

Figure 6. Blood cell covered with protein particles A marked with colloidal gold 5-10 nm.

A TOOL TO CALCULATE THE PARAXIAL PROPERTIES OF ELECTRON OPTICAL SYSTEMS

Jan Bärtle

Institute of Applied Physics, University of Tübingen
Auf der Morgenstelle 10, D-72076 Tübingen, Germany; eMail: jan.baertle@uni-tuebingen.de

Introduction

In the first design steps towards a novel electron optical system or component, initial paraxial calculations are usually performed under assumptions, e.g. thin lens, deflectors with sharp cut off fringing fields (SCOFF approximation). If the requested paraxial properties (such as stigmatic imaging, magnification, dispersion etc.) are obtained, the system or component may be improved further on using more elaborate techniques [1-9].
When dealing with electron monochromators or energy filters, not only the four geometric fundamental rays x_α, y_β, x_γ, and y_δ are required, but also the two dispersive fundamental rays x_κ and y_κ are of interest. These two rays emerge in dispersive electron optical components such as electrostatic toroidal condensers, magnetic sector fields or Wien filters. However, these components usually introduce second order aberrations not described in the paraxial domain. The elimination of at least the most disturbing one of these aberrations is mandatory for the overall system performance. This influences the fundamental rays: to cancel some of the aberrations special symmetry conditions concerning the course of the fundamental rays have to be met – despite of using stigmator elements which increase the system complexity. To obtain a system fulfilling all desired requirements, especially the symmetry of the fundamental rays, one has to calculate the properties of the electron optical system over a large parameter range.
The program *Paraxial* was developed to provide such calculations.

Program principle

It is advantageous to describe the paraxial properties of the electron optical components of interest in terms of transfer matrices allowing rapid calculations of the fundamental rays [10, 11]. The components have certain user defined properties e.g. their lengths or their excitations. These properties affect the matrix elements of the transfer matrices and hence influence the fundamental rays.
Besides the properties of the components, the geometric fundamental rays or their first derivative may be subject to conditions the user is supposed to enter. Typical conditions are the generation of intermediate stigmatic or astigmatic images. A simplex algorithm [12] is employed to vary the system under consideration to fulfil these conditions. A suitable system can be found semi-automatically.

Program features

Paraxial handles the dispersive electron optical components mentioned above, additional quadrupole lenses, and thin (rotation free) round lenses as well. The operation of *Paraxial* and the input of the data is performed interactively using a modern graphical user interface. Simultaneous calculation of the rays is performed as well as the graphical display of the results, so the user may directly control the consequences of his input. It is of interest to know exactly the position where the rays intersect the optical axis (the ray value is zero in this case). *Paraxial* detects these positions, not only zero but every user defined ray value.
The user can influence the program execution via options. Furthermore, dedicated output options in modern file formats are available to control the calculated fundamental rays and

their first derivative thus providing a reliable dataset with regard to further investigations. Special efforts have been spent on the efficiency of the ray calculation. This enables the simplex algorithm to test larger parameter ranges in a short time. The obtained relative accuracy is in the range of 10^{-10} and better. *Paraxial* performs a complete system calculation in fractions of seconds on modern PCs (depending on the amount of electron optical components, of course). With a suitable set of start parameters (= matrix elements) for the initial value problem, the simplex algorithm calculates typically about 500-1000 different system configurations in some few seconds until reaching optimal values.

Program limitations

Systems with a curved optical axis must have vanishing torsion, electrostatic quadrupole lenses have to fulfil even symmetry ($\phi_2 = \phi_{2C}$), magnetic ones have to fulfil odd symmetry ($\Psi_2 = i\Psi_{2S}$), the *standard orientation* in [13]. The electric fields of the Wien filters have to fulfil either even or odd symmetry whereas the magnetic fields are rotated azimuthally by 90° about the optical axis with respect to the electric field and have to fulfil opposite symmetry ($\phi_1 = \phi_{1C}$ and $\Psi_1 = i\Psi_{1S}$ or $\phi_1 = i\phi_{1S}$ and $\Psi_1 = -\Psi_{1C}$).
Paraxial has no option to calculate small angle deflections and no cylinder lens component is available (but can be generated in *Paraxial* using a quadrupole lens and a thin round lens).
Due to the nature of the periodic solutions of the paraxial ray equations, the simplex algorithm may fail to give correct solutions, especially when using inadequate start parameters.

Program implementation

A modern software development tool (Borland® Delphi™, [14]) was used to provide seamless integration of *Paraxial* into the Microsoft® Windows™ operating system. A regular windows user with electron optical knowledge should be able to use the program within a short time.

Program results

To demonstrate the results obtained with *Paraxial*, some already published electron optical systems have been calculated and the results are compared with the original data. Program performance tests using different example systems are also presented.

Referenees

[1] O. Scherzer: *Über die theoretische Elektronenoptik*, in Busch und Brüche: *Beiträge zur Elektronenoptik*, Verlag Johann Ambrosius Barth, Leipzig (1937).
[2] M. van der Stam: *Computer Assistance for the pre-design of Charged Particle Optics*, Ph.D. thesis, University of Technology, Delft (1996).
[3] F. Kahl: *Design eines Monochromators für Elektronenquellen*, Ph.D. thesis, University of Darmstadt (1999).
[4] E. Munro, in: Proc. of SPIE, Vol. 2014 (1993), 2.
[5] B. Lencová, in: Proc. 13th ICEM, Vol. 1 (1994), 145.
[6] J. Rouse, Adv. Opt. Electron Microsc. **13** (1994), 1.
[7] E. Plies, Adv. Opt. Electron Mircosc. **13** (1994), 123.
[8] M. van der Stam, J. E. Barth, P. Kruit, in: Proc. of SPIE, Vol. 2858 (1996), 90.
[9] E. Munro, in: Handbook of charged partiele optics, CRC Press, Boca Raton (1997), 1.
[10] H. Wollnik: *Optics of charged particles*, Academic Press, London (1987).
[11] E. Plies: *Teilchenoptik II*, Lecture held at the University of Tübingen (1997).
[12] W. Press et. al.: *Numerical Recipes*, Cambridge University Press (1989).
[13] P. Hawkes: *Quadrupoles in electron lens design*, Academic Press, London (1970).
[14] Borland Inc.: www.borland.com/delphi.

3D BEM FIELD SOLVER WITH ELIMINATION OF SINGULARITIES NEAR THE SURFACE

A.S.Berdnikov

Institute of Analytical Instrumentation, Rizhskij pr. 26, 198103 St.Petersburg, Russia. Email: asb@iota.ru

The report describes new BEM algorithm for 3D Laplace equation. The main goal of our investigation is to create the software which enables to calculate electric field with high accuracy up to the boundaries of the electrodes. BEM is unbeatable as soon as we consider the accuracy as the main point. But to get the highest possible accuracy, especially combined with the requirement to calculate the field accurately *up to the boundaries*, a lot of mathematical and algorithmical work should be done.

The list of possible sources of BEM errors include:

- approximate representation of true boundaries by the discretized surfaces,
- approximate representation of *continuum* set of charge densities by the discrete subset of charge density functions,
- deviations of numerically calculated integrals from analytically strict expressions,
- increased inaccuracies of numerical integration procedure near the boundaries and at the boundaries due to singular behavior of BEM kernel functions at these points,
- approximate representation of *continuum* boundary condition by discrete subset of collocation points or by some other fitting criterion,
- violation of true boundary condition if collocation or fitting points are shifted with respect to their nominal positions after approximate representation of the boundaries,
- inaccuracy of charge density values calculated by 3D solver which accumulate all these approximations and inaccuracies,
- increased errors in charge density values near the edges of the boundaries due to singular behavior of true charge density at these points,
- inconsistency of BEM representation with particular problem if its mathematical peculiarities are skipped by the programmer and selected BEM model is too narrow (for example, it is impossible to represent by charges the potential which is constant everywhere).

While some of errors are inevitable, others may be eliminated by intelligent BEM model. Let us consider it can be done.

1. To minimize the inaccuracy the boundaries are considered "as they are", assuming that they are represented by general parametric expressions like

$$\Omega(p,q)=\begin{cases} x=X(p,q) \\ y=Y(p,q) \\ z=Z(p,q) \end{cases}$$

– for each parametric point (p,q) from 2D rectangle $p_b \le p \le p_b$, $q_b \le q \le q_b$ we can calculate the surface point (X,Y,Z) (and tangential and normal vectors of the surface as well, if necessary).

2. Since our boundaries are as general as possible, there is no possibility to calculate BEM integrals analytically, and numerical integration is inevitable. To minimize the integration error *Gaussian qudratures* are used which enables to make the integration twice more accurate than the number of integration nodes. To make the charge density approximation to be consistent with the numerical integration routine, the charge values at integration nodes are taken as the "unknowns", so that the details of high order polynomial approximation are hidden inside integration nodes and weights. (Moreover, it makes the approximation scheme to be always of the same convergence order and accuracy, as the numerical integration procedure.)

3. The main improvement of new BEM algorithm is the elimination of irregularities and singularities of the integral kernel when the probe point is near the surface. When the probe point is near the surface, denominator of integral kernel behaves like

$$\tilde{K}(p,q) \approx \frac{\sigma(\bar{p},\bar{q})\, d\bar{p}\, d\bar{q}}{\sqrt{\bar{p}^2+\bar{q}^2+2\cdot c\cdot \bar{p}\cdot\bar{q}+\varepsilon^2}}$$

where $\bar{p}$ and $\bar{q}$ are normalized deviations from (p_0,q_0) – the surface point, which is the nearest nelghbor to probe point (x,y,z). The following terms are suspicious to behave irregularly during numerical integration at $\varepsilon \to 0$, and should be eliminated:

$$\frac{1}{\sqrt{p^2+q^2+\varepsilon^2}},\ \frac{p}{\sqrt{p^2+q^2+\varepsilon^2}},\ \frac{q}{\sqrt{p^2+q^2+\varepsilon^2}},\ \frac{p^2}{\sqrt{p^2+q^2+\varepsilon^2}},\ \frac{pq}{\sqrt{p^2+q^2+\varepsilon^2}},\ \ldots$$

To eliminate these singular and irregular terms special approach which we call *library of singularities* is created. Suppose that we have such analytical expressions $\varphi_k(p,q,x,y,z)$ that they can be integrated analytically over the surface and have near the probe point (p_0,q_0) a desired singular behavior. We can subtract the singularities from the kernel by proper selection of coefficients λ_k in modified expression for $U(x,y,z)$:

$$U=\iint_\Omega\left(\frac{\sigma(p,q)}{\sqrt{\Delta x^2+\Delta y^2+\Delta z^2}}-\sum_k \lambda_k\varphi_k(p,q,x,y,z)\right)dp\,dq+\sum_k \lambda_k \iint_\Omega \varphi_k(p,q,x,y,z)\,dp\,dq\,.$$

The first component of U is regular and is calculated numerically with the inaccuracy of the integration rule, while the second component *a priori* can be calculated analytically – i.e., with no additional errors. Field components U_x, U_y, U_z are calculated in a similar way although the library of singularities should be extended to include additional functions.

Experiments with analytical test cases demonstrated good accuracy (4^{th} order convergence) and stability for charge density and potential calculation. The resulting accuracy of potential near the boundary surface (i.e., when the distance between the probe point and the surface is much smaller than the distance between neighboring surface points with reference charges) for test cases was of $\sim 10^{-5}$. Due to harmonic properties the of point charge potential this error is much lower ($\sim 10^{-15}$) when the probe point is far from the surface. Although this work is definitely not finished yet and the solver requires more rigorous investigation of its properties, the new algorithm seems to be a very promising tool for high precision calculations of 3D electrostatic fields with almost arbitrary shape of boundary surfaces.

Acknowledgements

I would like to thank Shimadzu Research Laboratory (Europe), Ltd. for the support, and Dr. Michael Sudakov for very useful and important discussions during this investigation.

ELECTRON MICROLENSES AND MICROLENS ARRAYS

M.J. van Bruggen, B. van Someren, P. Kruit

Delft University of Technology, Faculty of Applied Sciences, Particle Optics Group
Lorentzweg 1, 2628 CJ Delft, The Netherlands

Introduction

Present day Micro Electrical Mechanical Systems (MEMS-) Technology allows the fabrication of microsources, -lenses and –multipoles, with dimensions in the micrometer range. Miniaturization of these electron optical elements is favorable, because the spherical and chromatic aberration coefficients scale correspondingly, leading to a superior performance over conventional electron optical systems[1]. In addition, miniaturized columns have a strongly reduced length and thus are less prone to external stray fields. Those micro-elements are perfectly suited to be fabricated in an array, achieving throughput enhancement in lithography applications.
There are several groups in the world working on the development of microsources and microcolumns[2-4]. Using such columns in an arrayed form is also under investigation for application in lithography[5] and for microscopy purposes[6].

Electron optics

Scaling laws can be derived which show that the electron trajectory scales with the lens dimensions if all relative potentials stay the same[7]. If we want to keep the same electron energy, it means that all lens potentials also stay the same. In that case, the electric field will scale inversely proportional with the lens dimensions. This constant potential scaling mode is favorable, since both the coefficients and aberration disks of the spherical and chromatic aberration scale by the same factor.

Practical challenges

While the constant potential scaling mode gives the best results in terms of spherical and chromatic aberration improvement, the electric field between neighboring electrodes will scale up, resulting in a situation in which that field might become larger than the breakdown field. Chang and coworkers used a selective scaling approach to circumvent this problem[8]. They mention a guideline of 10^4 V/mm for the maximum field between electrodes. However, this breakdown field scales better than linear with the inter-electrode spacing[9].
To prevent breakdown along the surface of the insulating spacers between the electrodes, they preferably have to be mounted at the peripherals of the lens assembly, where they can be scaled up. Not only will this be more and more difficult at lens downscaling, also the effect of electrode bending under the relatively high fields will become more pronounced: there is a constant trade off between prevention of electrical breakdown and this bending.
In the fabrication of microlenses, severe requirements are posed on the roundness and roughness of apertures and the alignment between them. Using an electron beam for patterning, in combination with self-aligned Reactive Ion Etching (RIE), some claim that a roundness and alignment with an accuracy of about 1 nm is possible, while edge roughness could be in the order of 10 nm[1]. Taking into account tolerances of 0.1-1 %, this limits the downscaling of lens apertures to the micrometer regime.
There are more problems that arise when operating micrometer-sized lenses, such as heating, charging of the insulating material and contamination of the electrodes by the electron beam. The influence of these effects on the performance of the system depends very much on the specific configuration at hand and research will be necessary to say something about it.

At this moment, we are developing a multibeam source module that splits up the broad beam of a Schottky source into multiple subbeams, individually focused by microlenses. By incorporating this module in a standard electron microscope (see fig.1), we want to be able to perform sub-10 nm lithography.

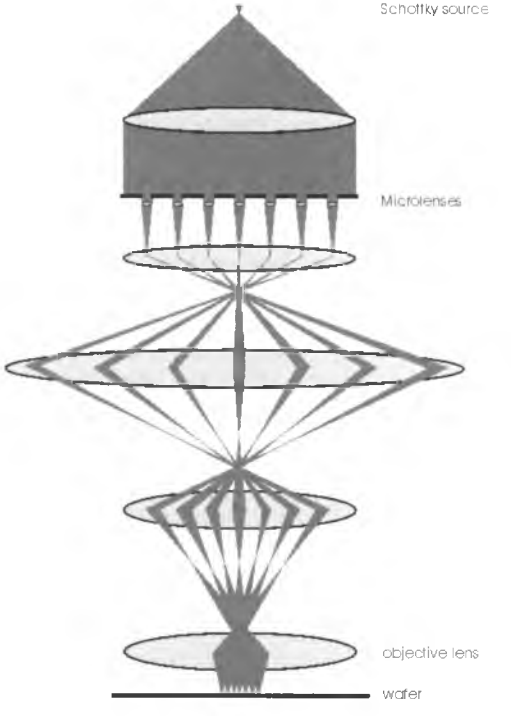

Figure 1. Schematical overview of the proposed multi-electron beam nanolithography concept, with a system of micro-apertures and –lenses to split up and focus the plurality of subbeams.

[1] Chang, T.H.P.; D.P. Kern; M.A. McCord; J. Vac. Sci. Technol. B 7(6), Nov/Dec, 1855 (1989)
[2] McCord, M.A.; T.H.P. Chang; D.P. Kern; J.L. Speidell; J. Vac. Sci. Technol. B 7(6), Nov/Dec, 1851 (1989)
[3] Park, J.-Y.; H.-J. Choi; Y. Lee; S. Kang; K. Chun; S.W. Park; Y. Kuk; J. Vac. Sci. Technol. A 15(3), May/Jun, 1499 (1997)
[4] Crewe, D.A.; M.M. Ruffin; A.D. Feinerman; J. Vac. Sci. Technol. B 14(6), Nov/Dec, 3808 (1996)
[5] Chang, T.H.P.; D.P. Kern; L.P> Muray; J. Vac. Sci. Technol. B 10(6), Nov/Dec, 2743 (1992)
[6] Feinerman, A.D.; D.A. Crewe; A.V. Crewe; J. Vac. Sei. Technol. B 12(6), Nov/Dec, 3182 (1994)
[7] Szilagyi, M.; Electron and ion optics, Plenum Press, New York, 1988
[8] Chang, T.H.P.; D.P. Kern; L.P. Muray; J. Vac. Sci. Technol. B 8(6), Nov/Dec, 1698 (1990)
[9] Ma, X.; T.S. Sudarshan; J. Vac. Sci. Technol. B 16(2), Mar/Apr, 745 (1998)

ON THE PERFORMANCE OF AN ENERGY FILTER FOR A HIGH BRIGHTNESS ELECTRON GUN

D. Cubric[a,*], S. van Kranen[b], P. Kruit[b] and S. Kumashiro[a]

[a] Shimadzu research Laboratory (Europe), Wharfside, Trafford Wharf Road, Manchester M17 1GP, UK
[b] Delft University of Technology, Faculty of Applied Sciences, Lorentzweg 1, 2628 CJ Delft, The Netherlands
* E-mail: dane.cubric@srlab.co.uk

Summary:
A high brightness electron source energy filter has been built and tested. The filter is of the Wien fringe filter type described previously [1]. The optics of the filter is designed to particularly suit the Schottky electron source. A particular new feature incorporated into the filter is an electrically isolated exit slit. Together with the independent control of several electric multipole fields at a single octupole unit, this enables detailed inspection of the beam profile and beam stabilization within the filter that in turn makes the filter usable in commercial instruments.

1. Introduction

A motive for this work is to use the filter for high-resolution low voltage scanning electron microscopy. The basis of this application is in decreasing effects of chromatic aberration and consequently in improvements of the spatial resolution [2]. A high resolution LVSEM requires both high source beam brightness and low electron energy spread. Our filter limits the brightness loss by matching the dispersion to the image size of the source and by reducing the Boersch effect through reducing the beam current entering the filter. The source image at the exit slit is very small hence only little dispersion is needed and a short Wien filter operating in low-excited mode is used.

2. Experimental results and discussion

The electron optical transfer part of the energy filter is built as a small one-lens SEM and it can image an exit slit (nanoslit) and surrounding parts by measuring the electric current received by the slit at each beam position. Figure 1 shows the sample current images obtained around the nanoslit holder tube. The sample current increases from white to black. Figure 1a shows various nanoslit structures that could be used for tuning and beam monochromatization. Figure 1b shows the top edge of the nanoslit holder tube imaged using the same process as before. Cleanness of the inlet aperture of the monochromator could significantly influence the beam profile and consequently the beam brightness. We have used a beam profile measurement to measure and quantify this effect. The beam profile at the nanoslit can well be described with a bell function S(x):

$$S(x) = \frac{I}{(1+4(2^{1/p}-1)(x/FWHM)^2)^p}$$

where p is a shape parameter; p=1 gives a Lorentzian and p>>1 gives a Gaussian distribution, the FWHM is a full width at half maximum and I is maximum intensity. Figure 2 shows the focused beam profiles at the nanoslit for two inlet aperture conditions. The difference in the shape and in the peak intensity comes from the inlet aperture charging effect. The shape parameters for the two measurements are 5 and 0.7, respectively. The brightness could easily decrease by 10 times due to the aperture effect. It is therefore important to have a means of testing the performance within the filter, as we have, and to identify and rectify the effect.

Figure 3 shows non-dispersed and dispersed beam shapes at the nanoslit. These are measured over a 500 nm slit. Further details on the brightness measurements dispersion and the energy spread will be presented at the conference.

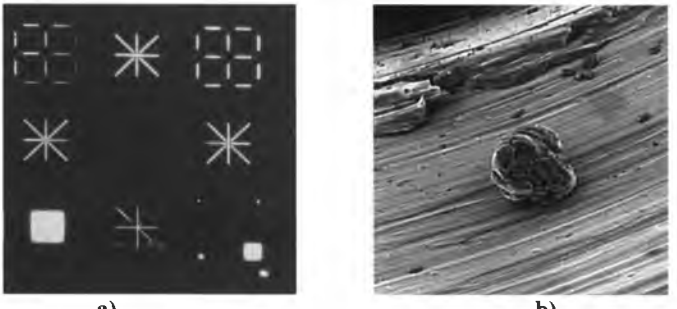

a) **b)**

Figure 1. The sample current images obtained around the nanoslit holder tube.
Field of view is 100 μm.
a) Nanoslit, b) at the top edge of the nanoslit holder tube.

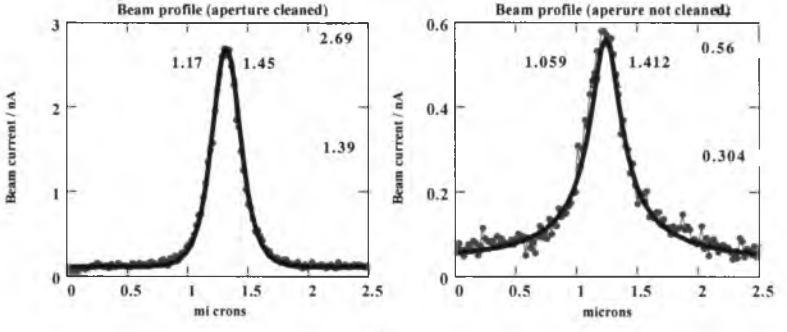

Figure 2. Beam profile at the nanoslit for differently eleaned inlet apertures. Measured over a 150 nm slit.

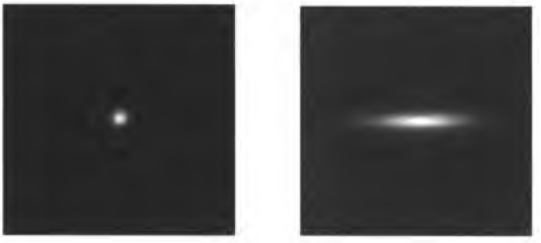

Figure 3. Beam profile measured over a 500 nm slit, of non-dispersed (left) and dispersed (right) beams. The dispersion is 2.72 μm /eV. Field of view is 10 μm. Scan contains 128x128 points.

Referenees

[1] H. W. Mook and P. Kruit, Nucl. Instr. And Meth. A, 427 (1999) 109
[2] J.E. Barth, M.D. Nijkerk, H.W. Mook and P. Kruit, EUREM XII, 2000, 1437

THE OPTICAL PART OF THE MULTICHANNEL ELECTRON ENERGY ANALYZER

Petr Čižmár

Institute of Scientific Instruments, ASCR, Královopolská 147, 61264 Brno, Czechia
cizmar@isibrno.cz

Our version of the multichannel energy analyzer[1][2] consists of two main parts. At first it is an electron optical part, which separates the entering electrons by their energy. Then the electrons land onto a scintillating screen. Secondly there is the optical part, which should project the light signal on the scintillator onto a detecting CCD. There are several ways how to do this.

In order to determine, which design is more useful for the multichannel analyzer, we need to know the efficiency and the resolution of the optical system. By efficiency the ratio between the light energy leaving the scintillation screen and that reaching the CCD is meant. The efficiency can be estimated from the maximum angle α between two rays emitted from one point reaching the first optical element. The efficiency primarily depends on the size of the first optical element. If there were no other loses the efficiency would be:

$$\varepsilon = \frac{1}{2}\left(1 - \cos\frac{\alpha}{2}\right)$$

For the resolution calculation, where we need to determine the size of the spot, to which one point is projected, we need to trace the rays. There were two designs calculated: the two-lens design and the elipsoidal-mirror design.

In the two-lens design the resolution depends on the shape of the lenses, as seen in figs 1 and 2 as well as on the distance from the central point. In both designs the spot size exceeds 10mm. It is possible to decrease the spot by reducing the size of the lenses, which decreases the efficiency.

The other possibility is to use an elipsoidal mirror to reflect the beam and to focus it onto the CCD. The shape of the mirror follows from the request to project the point X_0 to one point on the CCD. Then the shape is elipsoidal. Sizes of spots on the CCD were calculated with result in figs.3, 4, 5 and 6. Obviously, the resolution depends on the distance from X_0, where there are no aberrations, and on the size of the mirror. The nearer to the X_0, the better the resolution is. The only aberrations needed to be considered are the missalignment ones, unlike with the lens systems.

References:

[1] M.Jacka, M.Kirk, M.M.El Gomati, M.Prutton , Rev. of Sci. Instrum. 70(1999)2282
[2] F.H. Read, Rev. of Sci. Instrum. 73(2002)1129
[3] The work is supported by the ASCR Grant Agency under grant no. IAA1065304

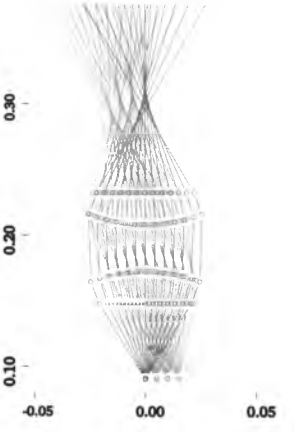

Fig. 1: Two-lens telescope design

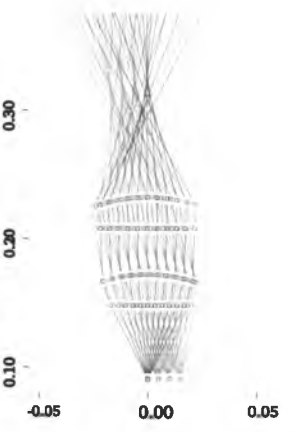

Fig. 2: Two-lens design with equaly oriented lenses

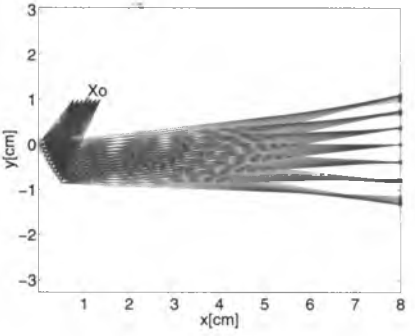

Fig. 3: Reflection and focus - mirror size: 1cm

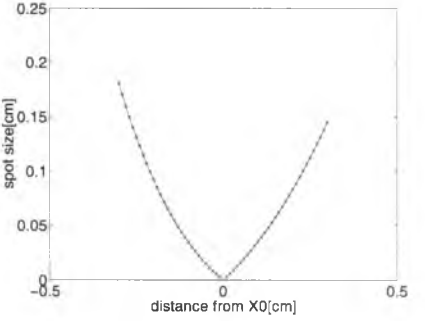

Fig. 4: Spot size dependence on the distance form the central point - mirror size: 1cm

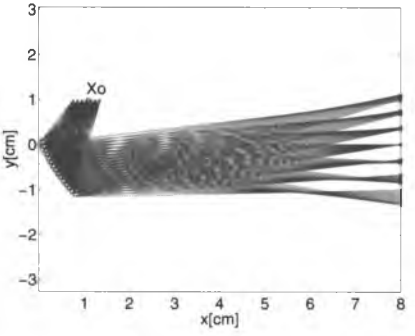

Fig. 5: Reflection and focus - mirror size: 1.5cm

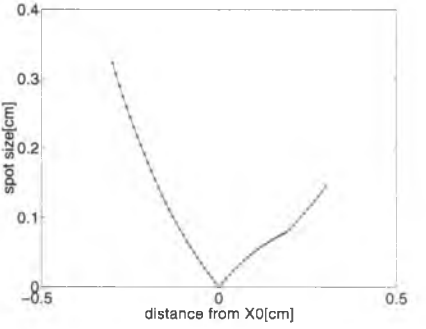

Fig. 6: Spot size dependence on the distance form the central point - mirror size: 1.5cm

FIELD EMISSON CATHODES FOR ELECTRON MICROSCOPES

Armin Delong and Vladimír Kolařík

DELONG INSTRUMENTS a.s., Bulharská 48, 612 00 Brno, vladimir.kolarik@dicomps.com

1. Introduction

Field emission emitters have significantly improved the coherence of electron guns in electron microscopes and allowed to reach atomic-scale resolution in the case of crystal imaging. Even now, thirty years after the first application of field emission emitters, one can hardly say that the development of electron emitters has been finalized.

2. Cold field emission emitters

The principle of cold field emission from the point of view of physics is relatively simple and depends theoretically on two parameters only: the work function and the electric field gradient close to the cathode surface. However, the real situation is much more complicated. A more realistic description of field emission of electrons is as follows: being emitted in a real technical dynamical vacuum, electrons are accelerated and hit the anode with an energy of several kVs. Their energy is sufficient for ionization and desorption of adsorbed gases and vapors on the surfaces being hit by the electron beam. Desorbed ions are accelerated and not only destroy the cathode by sputtering, but change at the same time the work function of the cathode surface. Emission current fluctuations are the results of this effect. This noise deteriorates different applications of electron beam devices.

Two parameters can to a certain extent improve the unfavorable situation. It is first of all the improvement of the vacuum by heating the electron gun to temperatures over 100°C for several hours. As an acceptable approach, vacuum systems pumped by ion getter pumps may be considered. The attainable pressure should not be worse than 10^{-8}–10^{-9} mbar. The second parameter, which can improve the emission properties, is the choice of suitable material of which the emitter is to be made. It is to be noted that the proposed solution should have one important property: emitters must be realized without any special and expensive equipment. Manufacturing costs, especially material costs, should be acceptable. Schottky emission cathodes which are widely used are too expensive and far away of the idea of using such cathodes with the aim of improving the parameters of simple instruments, which could be cheaper at the same time.

3. Material for cold field emission emitters

The improvement of field emission emitters, especially their emission current stability is made possible by choosing a suitable material, which will better resist the ion bombardment. Such materials are carbides of transition metals [Zr, Hf, Nb, Ta]. They feature significant advantages against the formerly used ones: reduced work function, more stable emission and resistance to ion bombardment. There are different ways to realize such emitters [1],[2].

It appears that the main problem connected with the realization of cold field emitters with sufficiently stable emission current is the ion bombardment. The idea of an appreciable pressure decrease has been rejected, being time consuming and expensive. Fortunately, one option still exists: to cover the point of an electron emitter with a dielectric layer which will protect the emitting tip from foreign material adsorption, ion bombardment or even act as a radiator thus protecting the tip against overheating [3]. Electrons from the tip are emitted into the conduction band of the dielectric and under the influence of the field, they are transported through the conduction band to the surface from which they escape into the vacuum [fig.1]. Electrons are heated during their transport with no change in their energy

distribution. There are several papers describing the results which have been achieved with this type of emitter. It is a matter of time only to find such a combination of materials, which will be able to meet most of the requirements for a simple and inexpensive realization of emitters.

An especialy interesting emitter type appears to be the emitter described in the literature [4]. In this case, the tip is prepared from carbon fiber, which is normally used for strengthening different materials [e.g. polymers]. The diameter of this fiber is about 7μm and is very easy to get. As a base for the emitter, a standard loop filament was used [fig.2]. The carbon filament was stuck to conducting epoxy and the tip was etched electrolytically in 0.1 mol water solution of NaOH. After ultrasonic cleaning the tip was dipped into epoxy resin with a viscosity, which gave a 0.2 μm layer after polymerization. After heating the emitter for several hours at 200 °C in vacuum, the emitter is ready for use.

Conclusion

Our experience gained with these emitters shows that such a kind of electron source can improve all kinds of electron microscopes especially those which are intended for routine work. We were able to get reliable operation in a vacuum of 10^{-7} mbar. The principle of this emitter seems to be very encouraging and further research will surely bring new achievements in this field. It can be expected that the cold field emission emitter will be much cheaper, requiring moderate vacuum only.

References

[1] Yada K.,A new preparation method of refractory carbides and their thermionic emission properties, J.Electron Microsc.,Vol.31,No 4, 349- 359, 1982

[2] Charbonnier F.M., Mackie W.A., Xie T.,and Davis P.R., Enhanced field emission from carbide-coaed field emitters and device applications, Ultramicroscopy 79, 73-82, 1999

[3] Zhirnov V.V., Wojak G.J., Choi W.B., Cuomo J.J., and Hren J.J., Wide band gap materials for field emission devices, J. Vac. Sci. Technol. A(15) 3, May/Jun 1997

[4]. Mousa M.S.,and Kelly T.F., Stabilisation of carbon-fiber cold field-emission cathodes with a dielectric coating, Ultramcroscopy 95, 125-130, 2003

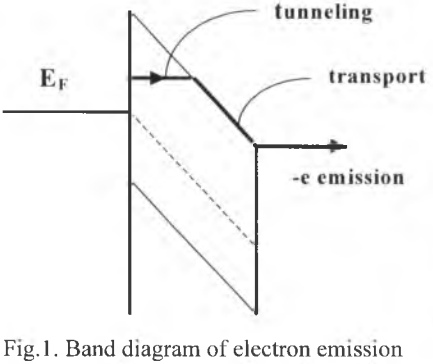

Fig.1. Band diagram of electron emission from an emitter coated with a dielectric layer.

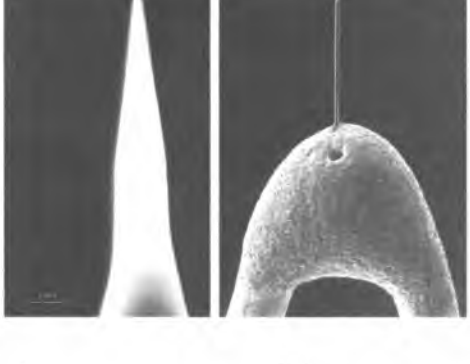

Fig.2. Carbon fiber field-emission cathode.

NANOESCA: A NEW ENERGY FILTER FOR IMAGING XPS

M. Escher[1*], M. Merkel[1], N. Weber[1], S. Schmidt[2], F. Forster[2], F. Reinert[2], C. Ziethen[3], P. Bernhard[3], G. Schönhense[3], B. Krömker[4], D. Funnemann[4]

[1]Focus GmbH, 65510 Hünstetten Germany
[2]Universität des Saarlandes, FR 7.2. Experimental Physik, 66041 Saarbrücken
[3]Johannes Gutenberg Universität Mainz, Institut für Physik, 55099 Mainz, Germany
[4]Omicron NanoTechnology GmbH, 65232 Taunusstein, Germany
* m.escher@focus-gmbh.com

A new instrument for Imaging XPS has been developed in close cooperation between the University of Mainz, the University of the Saarland, Focus GmbH and Omicron GmbH – the NanoESCA. The instrument consists of a Photo Emission Electron Microscope (PEEM) optic as entrance lens and a newly developed double pass energy filter (patent pending) that consists essentially of two hemispherical analysers. The energy filter is designed to give an achromatic image that is corrected for the aberration of dispersion of a single hemispherical analyser.

The microscope allows imaging with chemical contrast (Imaging ESCA) by energy filtering of photoelectron images at kinetic energies up to 1.6 keV, which are typical for XPS. Additionally, non energy-filtered PEEM imaging and a pulse counting mode for quantitative small spot spectra are implemented into the instrument. A schematic layout of the instrument showing the electron paths of the three different modes is shown in Fig. 1.

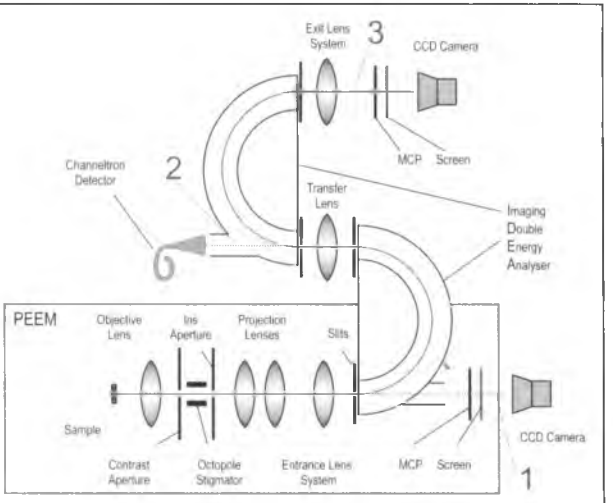

Fig. 1: Schematic layout of the nanoESCA instrument. The three paths of the electrons are indicated:
1. PEEM-Mode, 2. Selected area spectroscopy,
3. Energy filtered ESCA imaging. The grey box envelops the elements of the PEEM mode.

First characterization measurements were carried out at the Bessy II synchrotron radiation source (Berlin) and with laboratory sources. Fig. 2. shows measurements made on a $Cu_{0.98}Bi_{0.02}$ poly-crystal that proof the segregation of the Bi towards the grain boundaries of the crystal. The low background intensity of the Bi 4f-spectra taken on the Cu-grains demonstrates the very good capability of the instrument for spectroscopic imaging. We obtained an analyser energy resolution of $\Delta E \leq 190$ meV (FWHM). This was derived from the width of the Fermi edge at room temperature assuming a photon line width of 80 meV. The measure-

ment was taken at about 600 eV kinetic energy with a pass energy of 50 eV [1,2]. This is consistent with the expected energy resolution of a single conventional hemispherical analyser assuming the same pass energy and slit widths. As the instrument is designed for a minimal pass energy of 20 eV we expect to obtain energy resolutions below 100 meV.
Using the Imaging ESCA-mode we have successfully resolved 300 nm line structures taken at the Al 2p core-level with a contrast of (58±3) %. The lateral resolution of imaging XPS-electrons is up to now limited by mechanical vibrations in the synchrotron environment. Measurements with a laboratory UV-source indicate that the PEEM imaging is not deteriorated by the energy filter (lateral resolution 40-60nm).

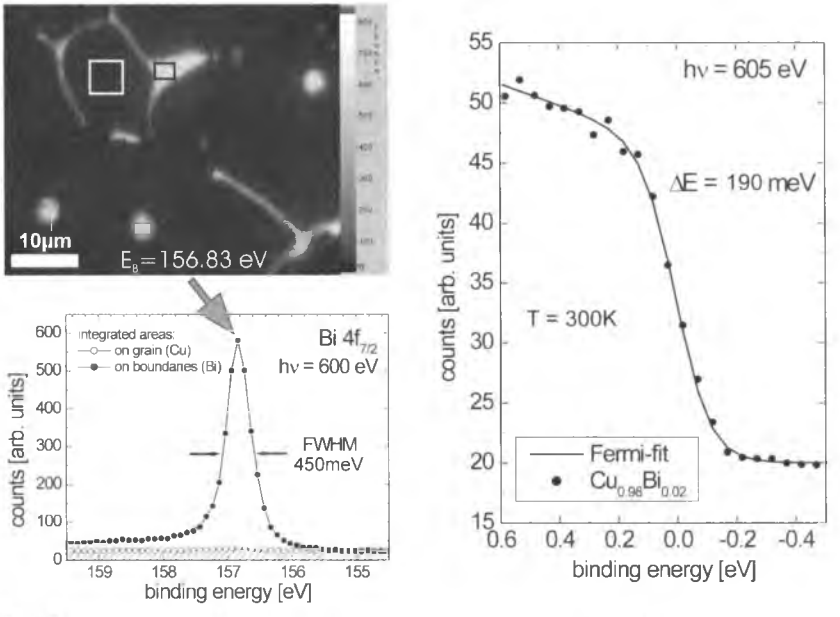

Fig. 2: Spectroscopic investigations of a $Cu_{0.98}Bi_{0.02}$ poly-crystal. The measurements were made with 50eV pass energy and slits of 1mm width.
Left: Imaging at the Bi4f7/2 core-level on the grains (open dots) and on the grain boundaries (filled dots), visible bright in the Bi image.
Right: Fermi-edge of the same sample (dots). The analysis of the data leads to an analyser resolution of ΔE_{fwhm} =190 meV.

This project was partly funded by BMBF, grant FKZ-No.13N7864

[1] D. Funnemann et al., Bessy Annual Report (2002), p. 350f.
[2] S. Schmidt et al., Bessy Annual Report (2002), p. 179f.

NANOSAM: SCANNING AUGER MICROSCOPE WITH SUB 10 NM RESOLUTION AND VARIABLE BEAM ENERGIES

A. Feltz, U. Roll, G. Schäfer, J. Westermann

OMICRON NanoTechnology GMBH, Limburger Str. 75, 65232 Taunusstein, Germany

During the last few years, we have developed a new electron column as an excitation source for UHV applications such as low voltage SEM, SAM, small spot Auger spectroscopy, cathodoluminescense and others. The instrument was developed in a cooperation between LEO (now ZEISS SMT-NTS), CEOS GmbH and OMICRON NanoTechnology GmbH.
Although the instrument is based on the LEO Gemini electron and uses a similar electron optics, it is constructed almost entirely from different parts and materials to make it UHV compatible and bakeable to 180°C.

FIG 1.: SEM image and lineprofile

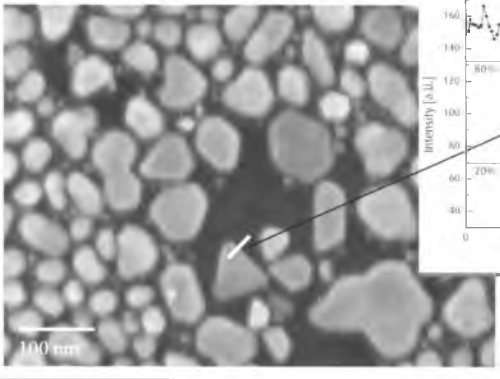

Gold islands on graphite, raw data. 15 keV beam energy, 400 pA beam current, 8 mm working distance.

One main feature of this electron column is the ability to achieve <3 nm ultimate spot size at working distances as large as 8 mm, but it is also capable of small spot sizes at low beam energies, such as <10 nm at 1 keV and 1 nA.

In the present work we now report about the results obtained with Auger spectroscopy and scanning Auger microscopy utilising this source. The ultimate spatial resolution in scanning Auger mode was so far found to be below 10 nm (see Fig. 2.).
We explicitly distinguish between the spatial Auger resolution and the probe diameter. The latter is related to the SEM resolution, which has been found to be 6 nm for this measurement (10 keV, 1 nA). The spatial Auger resolution however is also influenced by the energy dependent interaction volume, edge effects, image contrast and other Auger-intrinsic parameters [1, 2, 3, 4]. Although these early papers describe many of the effects that we see, no studies are so far available in our parameter space with sub 10 nm probe sizes, beam currents in the range of 1 nA, and beam energies from 30 keV down to 1 keV.

As an example we present a combined SEM, SAM, and Auger spectroscopy experiment (Fig. 3.). The aim of this experiment was to determine why the growth of Ag islands on this Si substrate showed such irregular island shapes. Usually the islands are well orientated alongside the corner hole directions ({2,-1,-1} and {1, 1,-2}) of the underlying Si(111) surface (compare with Fig. 2). The spectra and SAM images revealed a contamination of the sample with Molybdenum and Sulfur.

FIG 2.: Ultimate SAM resolution

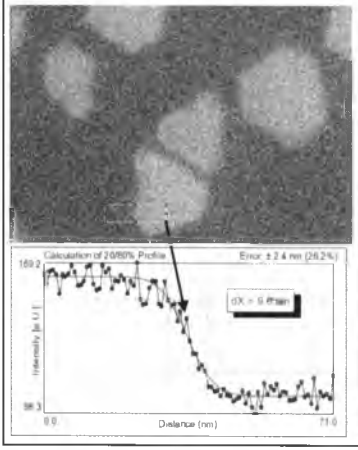

Silver nanocrystals on silicon substrate,
9 nm edge resolution (20%-80%).
Ag MNN, 352 eV, background at 390 eV,
(P-B)/(P+B), 512x384 pixel, 13 min per frame,
beam energy 10 keV, 1 nA beam current.

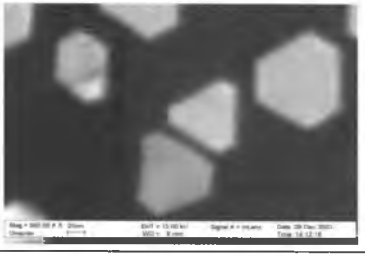

The corresponding SEM image reveals a resolution of 6 nm.

FIG 3.: SAM images and spectra

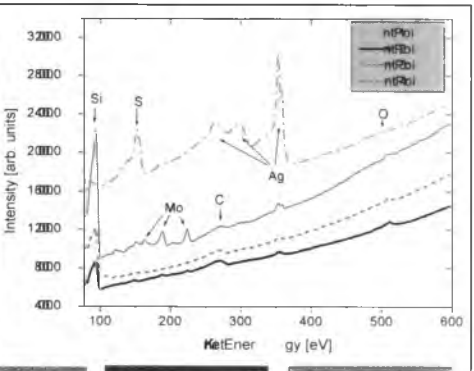

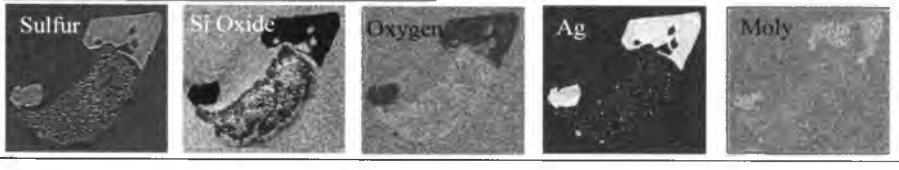

Besides for SEM and Auger applications, the UHV Gemini has also been used in combination with STM. The combination of STM and SEM has been found extremely helpful for e.g. tip positioning, and it enables a zoom from mm scale down to 10 pm resolution on the same sample spot. However, the key application for this combination will be the STM investigation of nanostructured resist layers (Self Assembled Monolayers, EBL).

[1] J. Cazaux, Surface and Interface Analysis, Vol. 14, 354-366 (1989)
[2] J. Cazaux, Surface Science 125 (1983) 335-354
[3] M.M. El Gomati et al, Surface and Interface Analysis, Vol. 11, 251-265 (1988)
[4] M.M. El Gomati et al, Surface Science 85 (1979) 309-316

A STABLE MODE FOR AN ELECTROSTATIC STORAGE RING

P Hammond[1*], F H Read[2], T J Reddish[3] and P J Harvey[2]

[1]Department of Physics, University of Western Australia, Perth WA 6009, Australia.
[2]Department of Physics and Astronomy, University of Manchester, Manchester M13 9PL, UK.
[3]Department of Physics, University of Windsor, Windsor, Canada N9B 3P4.
*email address: Hammond@physics.uwa.edu.au

Most storage rings and circular charge particle accelerators use magnetic fields but for studies in atomic and molecular physics a purely electrostatic storage ring has the advantages of small size, low power consumption, no magnetic hysteresis and the ability to store ions of any mass as electrostatic deflection depends on energy and not on momentum. The '*ELISA*' storage ring [1] was the first of this type and other similar electrostatic ion storage systems are being designed and constructed [2,3].

Conventional 180° hemispherical deflectors were not used in *ELISA* because it seems that their 'strong focusing' property [1] causes instabilities. Instead 160° sector hemispherical deflectors were used initially because of their equal focussing in the 'vertical' and 'horizontal' directions. Later the deflectors were changed to a cylindrical geometry [4] to avoid the reduction of the beam lifetimes at high beam intensities caused by the existence of narrow beam waists.

We have designed (and are constructing) the electrostatic ring *'ERS'* (Electron Recycling Spectrometer) that will be used initially as a novel source of mono-energetic electrons and later as a storage device for positrons and polarised electrons. The *ERS* incorporates 180° hemispherical deflectors because of their good energy dispersion. In the present paper we consider the stability of the *ERS* and describe a new mode that has been found to be stable.

The *ERS* is intended primarily for use with low-energy electrons. A cut-away view of it is shown in Fig. 1. It consists of two hemispherical deflection analyzers (HDA) between which are electrostatic lens systems. The CPO3D program [5] has been used to model it.

View of one half of the Electron Recycling Spectrometer showing one of the hemispherical deflection analysers and the lens stacks at its entrance and exit.

The obvious way to study the stability of the device is to use a simulation program to integrate the trajectories through large numbers of revolutions, which we have done, but this has the disadvantage of cumulative numerical errors. We have therefore developed a method that uses transfer matrices that are established by an accurate simulation of a single revolution.

Using the conventional definitions [6] for the transfer matrices of the lenses and the HDA the combined matrix for the transfer matrix from the source to the target (which are in the middle of the upper and lower arms respectively) is

$$M_{st} = \frac{1}{f_1 f_2}\begin{pmatrix} f_1 f_2 - 2K_1K_2 & 2K_1(f_1 f_2 - K_1K_2) \\ -2K_2 & f_1 f_2 - 2K_1K_2 \end{pmatrix}$$

where

$$K_1 = P - F_1, \qquad K_2 = Q - F_2$$

and where P and Q refer to the positions of the source and the entrance to the HDA. It is assumed here that the system is symmetric so that the electron energy at the target is the same as that at the source. The overall transfer matrix from the source back to the source is then

$$M_{ss} = M_{st}\, M_{st}$$

and the general condition for the stability of the orbits [7] is

$$\frac{1}{2}\left|Tr(M_{ss})\right| \le 1$$

We have chosen to satisfy this stability condition in a novel way by using the following form for M_{st}

$$M_{st} = \begin{pmatrix} 0 & u \\ \dfrac{-1}{u} & 0 \end{pmatrix}$$

which gives

$$M_{ss} = \begin{pmatrix} -1 & 0 \\ 0 & -1 \end{pmatrix}$$

for any value of u and which can be satisfied for the present system if $u = K_1$ and if the following condition is satisfied

$$f_1 f_2 = 2K_1K_2$$

The image is then inverted after one revolution but is restored after two revolutions. We find that this mode of operation remains stable when the parameters of the lenses and the HDA vary slightly, which is not the case for the more conventional mode in which M_{ss} is the unit matrix.

The properties of this new mode will be discussed in detail include (1) the effects of aberrations, (2) the energy resolution of the spectrometer and (3) the behaviour when the target energy is different from the source energy.

References

[1] S. P. Møller, Nucl. Inst. Meth. **A 394**, 281 (1997).
[2] T. Tanabe, K. Chida, K. Noda, I. Wantanabe Nucl. Inst. Meth. **A 482**, 595 (2002).
[3] C. P. Welsch, A. Schempp and H. Schmidt-Böcking Hyp Inter **146** 253 (2003).
[4] S. P. Møller and U.V Pederson Phys Scr **T92** 105 (2001)
[5] CPO Programs, available on the Web site http://www.eleetronoptics.com/
[6] J. H. Moore, C. C. Davis and M. A. Coplan, *Building Scientific Apparatus*, 2nd Ed., Perseus Books, Reading Massachusetts, 1989.
[7] J. D. Lawson, *The Physics of Charged Particle Optics*, Clarendon Press, Oxford, 1988.

CATHODOLUMINESCENCE OF POLYSILANES

P. Horák, P. Schauer

Institute of Scientific Instruments AS CR, Brno, Czech Republic, horak@isibrno.cz

Polysilanes – a broad class of organic materials whose basic building block is a chain built up of silicon substituted by alkyl or aryl groups. Properties of these substituents significantly affect properties of polysilanes. This material is very interesting because of its chemical, electrical and optical properties [1]. In spite of great research interest in recent years cathodoluminescent (CL) properties of polysilanes were not yet studied. Poly[methyl(phenyl) silane] (PMPhSi) is a typical representative of polysilanes which was prepared by the Wurtz coupling polymerization. Thin layers of PMPhSi were prepared from toluene solution by a spin coating technique [2]. The material was applied on the quartz glass substrate and covered with the aluminium (Al) film. The Al film protected the specimen from charging and reflected photons emitted under the specimen surface towards the quartz glass substrate.

The method of PMPhSi study was based on the measurement of CL intensity after passing through the specimen (Figure 1). Electron beam, emitted from a wolfram cathode, accelerated and focused in the excitation part, struck the Al deposited specimen. Emitted photons which passed through the specimen and through the substrate were led by a light guide to the detection part.

The excitation part was based on the rebuilt electron microscope TESLA BS 242. Electron beam energy was variable from 1 to 60 keV. The deflecting system allowed modulation of the electron beam and enabled measurement, not only in the continual mode, but also in the pulse mode. This was very important for the measuring in the synchronous mode as well. The detection part was based on a photomultiplier tube [3].

The first PMPhSi specimens of the thickness of 2 μm covered with 50 nm of the Al film were measured using the photomultiplier tube TESLA 65 PK 415. The excitation energy of 10 keV was used for cathodoluminescence intensity measurement in the continual mode (i.e. the deflecting system is switched-off). Current density of the incident electron beam was approximately 5 nA / mm^2. The CL emission from PMPhSi was smaller by 2 orders of magnitude in comparison with the CL emission from the YAG:Ce single crystal and measured under the same conditions [4]. Strong influence of the background, above all of the cathode light, was proved and also measured by switching off high voltage (only wolfram filament is heated).

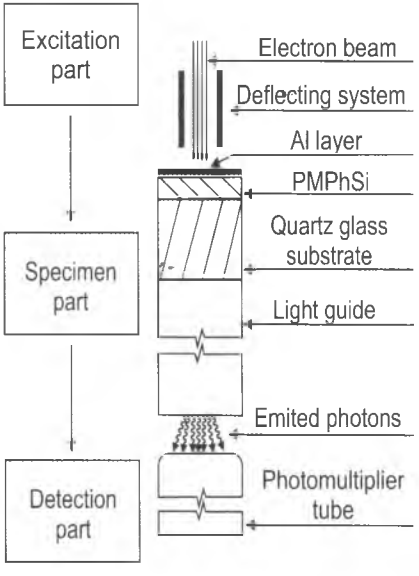

Figure 1 *Layout of the experimental arrangement for the study of cathodoluminescent properties of polysilanes including the specimen part details.*

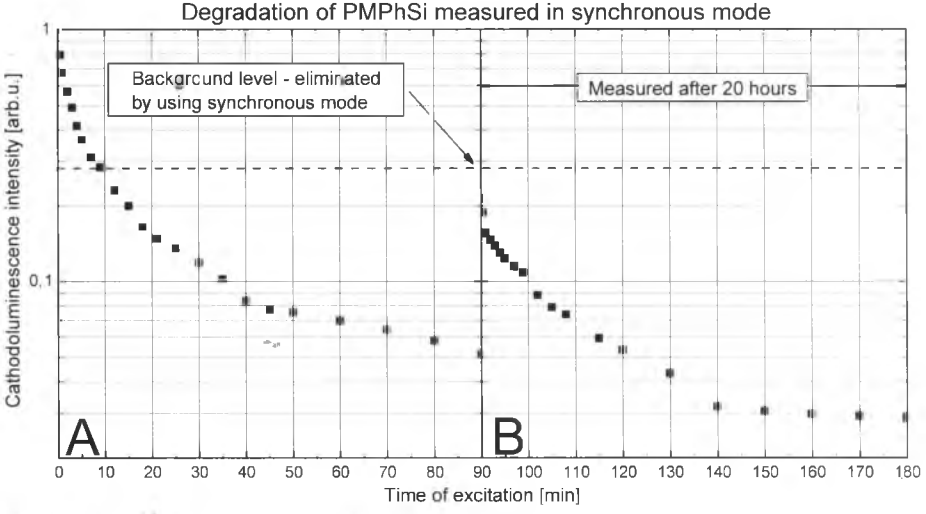

Figure 2 *Time dependence of PMPhSi CL intensity measured for 90 minutes (part A) and subsequently after 20 hours of leaving in a vacuum chamber of microscope at room temperature for next 90 minutes (part B).*

Measuring in the synchronous mode was used to eliminate the influence of the background and noise. The electron beam was modulated using the pulse generator TR-0331. The frequency of modulation was 1 kHz. The reference pulse taken from the trigger output of the pulse generator was connected to the reference input of the lock-in nanovoltmeter UNIPAN 232 B. The change of the PMPhSi CL intensity was measured using this lock-in nanovoltmeter and plotted on semilogarithmic graph (Figure 2).The experimental conditions at this measurement were as written above (10 keV, 5 nA / mm^2, 1 kHz).

The decrease of CL intensity of PMPhSi was assigned to a material degradation. The fastest degradation of the new specimen (part A of the graph) was seen in the first 10 minutes (about 70% decrease of the intensity). The degradation of PMPhSi was still going on, but much more slowly, after 50 minutes of excitation (about 1% in 10 minutes). After 20 hours of no excitation, with the specimen left in the vacuum chamber of the microscope at room temperature, the PMPhSi was again excited by the electron beam under the same conditions (part B of the graph). Partial recovery of the CL intensity (20%) was observed. The CL intensity value in 120^{th} minute was nearly identical to that in 90^{th} minute of the previous measurement. After 140 minutes of electron beam excitation, the CL intensity was almost invariable, but reached only 1% of the initial intensity value. The changes of the slope of the curve in the 10^{th} and 40^{th} minute (part A) as well as in the 140^{th} minute (part B) may indicate creating metastable states.

References

[1] Miller R.D., Michl J.: Chem. Rev. **89** (1989), 1359-1410.
[2] Nešpůrek S.: Mater. Sci. and Eng. **C 8-9** (1999), 319-327.
[3] Schauer, P.; Autrata, R.: Proc. of 7th Inter. Seminar on Recent Trends in Charged Particle Optics and Surface Physics Instrumentation, Skalský Dvůr (2002), 67-70.
[4] Autrata, R.; Schauer, P.: Scanning Microscopy (Supplement) **9** (1996), 1-12.

VERY LOW ENERGY SCANNING ELECTRON MICROSCOPY

P. Hrnčiřík and I. Müllerová

Department of Electron Optics, Institute of Scientific Instruments of the Academy of Sciences of the Czech Republic, Královopolská 147, Brno 61264, Czech Republic
email: pecan@isibrno.cz

The inelastic and elastic mean free paths (IMFP and EMFP) determine the largest sample thickness usable for transmission electron microscopy (TEM). At primary electron energies normally used for TEM (>50 keV), both mean free paths decrease as the primary energy is lowered. If the primary energy is lowered to below about 100 eV, IMFP is predicted to stop decreasing and to begin growing again [1, 2]. This opens up the exciting possibility of very low voltage TEM of sufficiently thin samples, with poorer resolution but greatly reduced radiation damage compared to conventional TEM.

Previous investigations of this effect employed electrons field-emitted from a nanotip [3]. The incident electron energy was determined primarily by the tip-to-sample distance, and was not adjustable below about 40 eV. Similar experimental set-up as ours was proposed in [4], but with no experimental results at that time.

In our arrangement, we have used a scanning low energy electron microscope (SLEEM) designed for the operation down to zero landing energy [5]. An addition detector of transmitted electrons modifies this microscope. The resulting combination of SLEEM / SLETEM (scanning low energy transmission electron microscope) uses the cathode lens to decelerate the primary electron beam just in front of the specimen surface, and is able to reach a resolution of a few nm even at landing energies in units of eV. This provides with flexibility to investigate the transmission of electrons through thin samples at electron energies as low as 1 eV.

A set up of the detection part of the instrument is shown in Figure 1. The primary electrons at 10 keV are decelerated by finely adjustable negative bias to the specimen. Signal electrons, both reflected and transmitted, are accelerated to detectors at ground potential. The SLEEM detector is formed by an annular disk of YAG single crystal with the diameter of the opening around the optical axis of 0.3 mm; the SLETEM detector consists of a PIN diode collecting the total transmitted signal. The geometry of SLETEM and the collection efficiency of the transmitted detector were optimised by using SIMION 3D software [6].

The experimental instrument is based on the ultrahigh vacuum SEM Tesla BS350 that was equipped by a Schottky field emission gun. The vacuum system and control electronics were fully renovated, too.

We have shown first images at low energies of a holey carbon foil approximately 20 nm thick [7]. In this study we used a 5 nm carbon foil; the images recorded at different energies are shown in Figure 2. Unfortunately, no indication of increase in the foil transparency at 1- 2 eV compared to 20-100 eV was shown again. At certain energies we have noticed a higher contribution of secondary electrons to the total signal from the specimen. The signal from the foil is then higher than that from places where is no foil. Landing energy, at which this effect appears, depends on the foil thickness. This could be very easy method how to measure the sample thickness.

More detailed study is necessary in the future in order to understand the inherent phenomena.

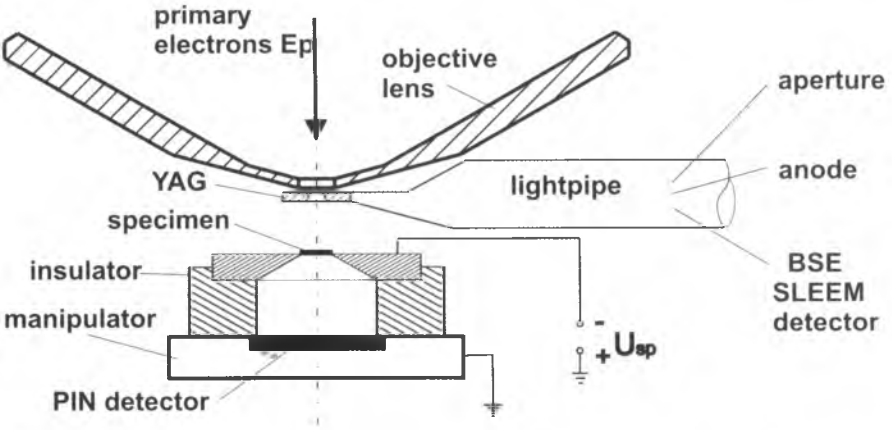

Figure 1: The experimental set-up of detection parts of the SLEEM / SLETEM instrument.

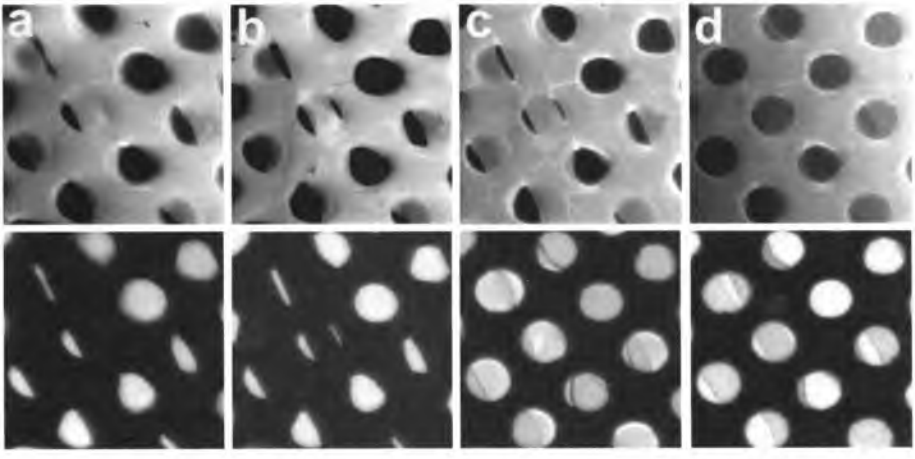

Figure 2: SLEEM (above) and SLETEM (below) images of a carbon foil of a thickness of 5 nm on a copper grid of 83 μm period, taken at the landing electron energy of a) 2 eV, b) 40 eV, c) 700eV, and d) 3 keV.

References

[1] Kanter H., Physical Review **B 1** (1970) 522.
[2] Ding Z.J. and Shimizu R., Scanning **18** (1996) 92.
[3] Spence J.C.H., Micron **28** (1997) 101.
[4] Rensen M.J.M. et al. in: Proc. of 8th Internat. Seminar on Recent Trends 2002, Brno, 5.
[5] Müllerová I. and Frank L., Adv. in Imaging and Electron Physics **128** (ed. P.W. Hawkes), Elsevier 2003, 309.
[6] Dahl D.A., 43rd ASMS Conference on Mass Spectrometry and Allied Topics, 1995, Atlanta,Georgia, 717.
[7] Hrnčiřík P. et al., in: Proc. of EMC 2004, Antwerp, Belgium, in press.

This work is supported by research project No. B 2065405 of Grant Agency of AS CR.

A 2D INTERACTIVE MESH GENERATOR FOR FINITE ELEMENT PROGRAMS

Jiang Jinhua and Anjam Khursheed

National University of Singapore, 4 Engineering Drive 3, Singapore 117576.
e-mail: eleka@nus.edu.sg

The finite element method is a powerful numerical method widely used to solve field distributions in charged particle optics [1, 2]. One of the most challenging aspects of using the finite element method is to create a suitable mesh. This is a non-trivial task since there are several requirements that must be simultaneously satisfied. Firstly, for reasons of optimizing program run-time and minimizing memory usage, the mesh should be concentrated in areas of high field strength. Secondly, the mesh spacing should change smoothly, particularly in and around regions of high field strength. Thirdly, the mesh should fit a wide variety of electrode shapes, both polygon shapes as well as curved boundary shapes. Fourthly, the mesh should be structured, this makes it easier to use high-order interpolation techniques for plotting accurate trajectory paths of charged particles [3]. Lastly, the mesh generator should be interactive and easy to use. This paper describes how such a mesh generator was developed within the Electrical and Computer Engineering department of the National University of Singapore. The mesh generator was written on a visual C++ platform.

The mesh generator functions by highlighting region blocks on a background region block mesh and locally modifying or transforming it to the desired shape. Figs 1a and 1b illustrate this process for polygon electrodes, while Figs 2a and 2b illustrate this for elliptical shapes.

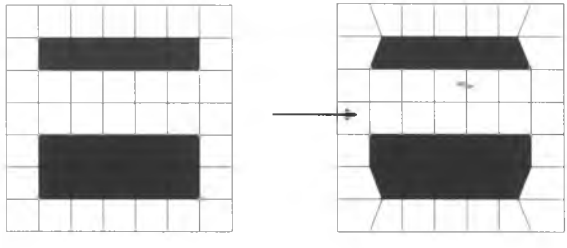

Figure 1: Creating polygon shapes

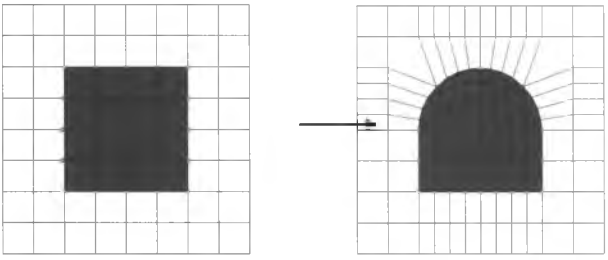

Figure 2: Creating elliptical shapes

The mesh generator incorporates the ability to grade the mesh. Several high density regions can be simultaneously specified and the program will create a mesh whose density changes smoothly. The following is a quadrupole example which involves transforming square electrodes to be circular and grading from a high density square region at the centre, as shown in Figs. 3a and 3b. Fig.3 c shows the equipotential lines of a finite element solution using this mesh.

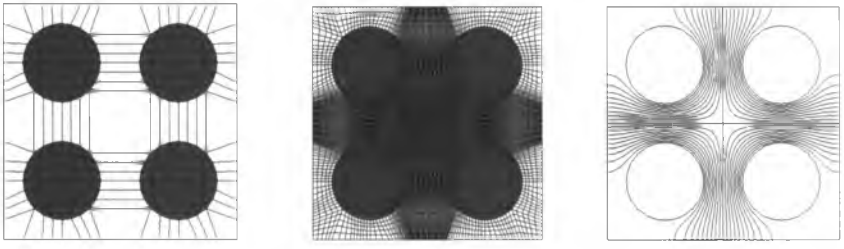

(a) (b) (c)

Figure 3: A Quadrupole example
(a) Region Blocks (b) Fine Mesh (c) Equipotential lines from an FEM solution

References

[1] A. Khursheed, The Finite Element Method in Charged Particle Optics, Kluwer, Boston, 1999.

[2] B. Lencova, Recent Trends in Charged Partiele Optics and Surface Physics Instrumentation, 8th Seminar Proceedings, p13-14

[3] Chapter 11.4 of Ref. 1

SIGNAL DETECTION USING SEGMENTAL IONIZATION DETECTOR

J. Jirák, P. Černoch*, R. Autrata

Institute of Scientific Instruments ASCR, Královopolská 147, 612 64 Brno, Czech Republic
*Department of Electrotechnology FEEC BUT, Údolní 53, 602 00 Brno, Czech Republic
jirak@feec.vutbr.cz

For signal electrons detection at environmental conditions, it is often used a detector that utilizes impact ionization in the gaseous environment of a specimen chamber for a signal amplification. An electrostatic field created in a space between a grounded specimen and a detector electrode provides the energy needed for efficient ionization of secondary electrons. A voltage of several hundred volts is attached to the detector electrode. Danilatos [1] proposed an electrode system of a ionization detector with several concentric electrodes, where a higher diameter of the electrodes brings a higher contribution of backscattered electrons to the detected signal.

In our experiments, the properties of the electrode system consisting of four concentric electrodes were studied. The electrode system showed in Fig. 3 was created by the printed circuit board technology. The inner diameter of the smallest electrode is 2.5 mm; the outer diameters of the electrodes are 4, 9, 14 and 19 mm. The gap between the electrodes is 0.5 mm. For this electrode system, a dependence of a signal level from a golden foil specimen on pressure was measured at the varied interconnections of the electrodes. Results of the measurement where the signal was detected from the electrode A which was on a potential of 400 V and outer electrodes were either not contacted or grounded are plotted in Fig. 1. In following measurements, the signal from the electrodes A and B on the potential of 400 V, respectively from the electrodes A, B and C on the same potential (Fig. 2), was detected and the outer electrodes were not contacted or grounded. The measurements show the increase of the detected signal level caused by adding of additional electrodes. The configuration with the grounded outer electrodes provides always a higher signal level in comparison with not contacted outer electrodes. Also the maxima of the signal level occur at a higher pressure for all measurements with grounded outer electrodes.

A similar electrode system with electrodes divided into two halves – right and left halve – was prepared for other experiments. A specimen, consisting of Al metallization on a silicon substrate, was observed by this electrode system. An image of the specimen at the electrodes interconnection, where the signal was detected from the left halve of the inner electrode with a voltage of 300 V and all other electrodes were grounded, is shown in Fig. 4a. The same specimen and similar detection conditions but with 300 V potential also on the right halve of the inner electrode is pictured in Fig. 4b. A shadow effect visible in this figure shows that in the case of signal detection with a ionization detector, when the process of impact ionization takes place in the space between the specimen and the detector, the effect of the position of the detection electrode on the image contrast manifests itself.

This research has been supported by Grant Agency of Academy of Sciences of the Czech Republic, grant No. S2065107.

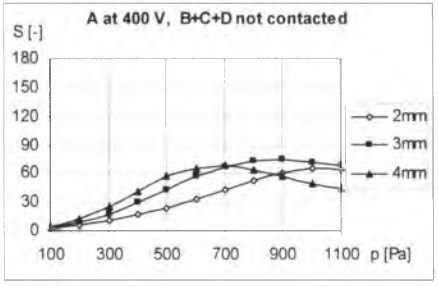

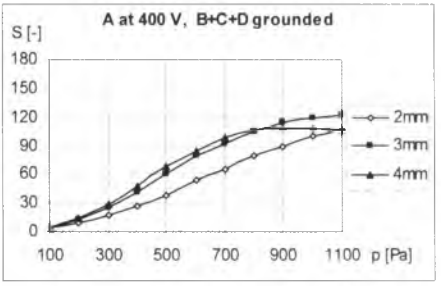

Fig. 1. Dependences of golden foil signal level on pressure of water vapors, detection electrode A at 400 V, electrodes B, C, D not contacted or grounded

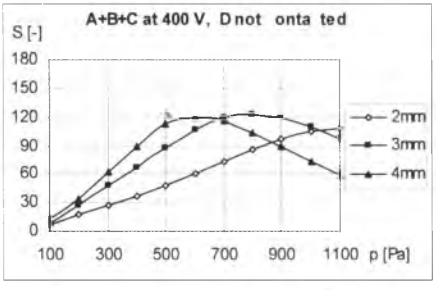

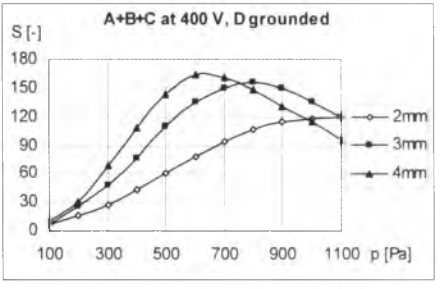

Fig. 2. Dependences of golden foil signal level on pressure of water vapors, detection electrodes A, B, C at 400 V, electrode D not contacted or grounded

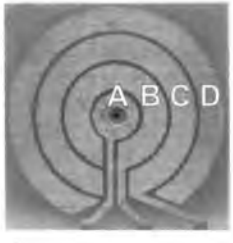

Fig. 3. Segmental ionization detector

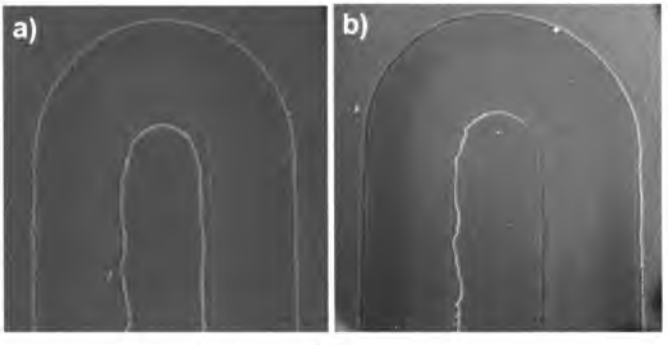

Fig. 4a,b. Al metallization on silicon substrate detected by halved segmental ionization detector, shadow effect on Fig. 4b

[1] DANILATOS, G. D.: Foundations of Environmental Scanning Electron Microscopy. Sydney, Academic Press, 1998, 250 p.

THE SPECTROSCOPIC SCANNING ELECTRON MICROSCOPE (SPSEM)

Anjam Khursheed

National University of Singapore, 4 Engineering Drive 3, Singapore 117576. eleka@nus.edu.sg

In principle, many analytical techniques can be combined with the normal operation of the SEM, but in practice, they are limited to a few routinely used add-on attachments [1]. The main reason for this lies in the way SEMs are currently designed. At present, the SEM column typically consists of an electron gun, electromagnetic lenses, scan coils and apertures, see Fig. 1. The purpose of this column is to produce a highly energetic (1- 30 keV) beam of electrons that is successively focused into a sub-micron probe and raster scanned over the sample's surface. The problem with this conventional SEM design is that most the electrons and photons scattered back from the sample travel towards the column and are therefore difficult to detect and analyze. Moreover, the distance between the lower pole-piece of the objective lens and the surface of the sample, commonly called the working distance, is relatively small, typically restricted to be between 3 to 25 mm. There is therefore little room in this design to mount detectors and spectrometers that can efficiently collect the scattered electrons and photons generated by the primary beam-specimen interaction or analyze their energy spectra with high resolution.

The SEM proposal described here does not restrict detectors or spectrometers to be located in the small space between a conventional SEM objective lens and the specimen. The new SEM design layout is depicted in Fig. 2. The central concept behind the design is to lie a conventional SEM column on its side, so that the primary beam initially travels in a horizontal direction and then to turn it through 90 degrees by magnetic sector plates so that the primary beam strikes the specimen in the normal vertical direction. The specimen in this case is located inside or just above the objective lens, which is integrated with the specimen chamber. The scattered electrons and photons are therefore not obstructed by the SEM column which lies in a horizontal direction located well away from the sample. The scattered electrons and photons are directed on to a hemispherical region above the specimen, unobstructed by the SEM column. An array of electron and photon detectors/spectrometers can be mounted on this hemispherical collection surface, essentially unrestricted by space constraints.

The new SEM design has several advantages over conventional designs. Firstly, it is predicted to have high transport efficiency for all scattered electrons and photons, typically over 80%. Secondly, the energies of the scattered electrons can be analyzed with high precision, where the energy resolution is expected to be typically better than 10^{-4}. Thirdly, it provides for better separation between different types of scattered electrons. Fourthly, the new SEM design can easily be extended to incorporate time multiplexed columns and multi-column arrays. The redesigned SEM presented here is referred to as the "Spectroscopic SEM", or simply "SPSEM", since it naturally combines SEM imaging information with energy spectroscopy.

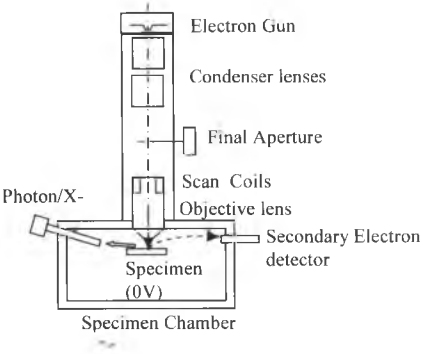

Figure 1: Conventional SEM

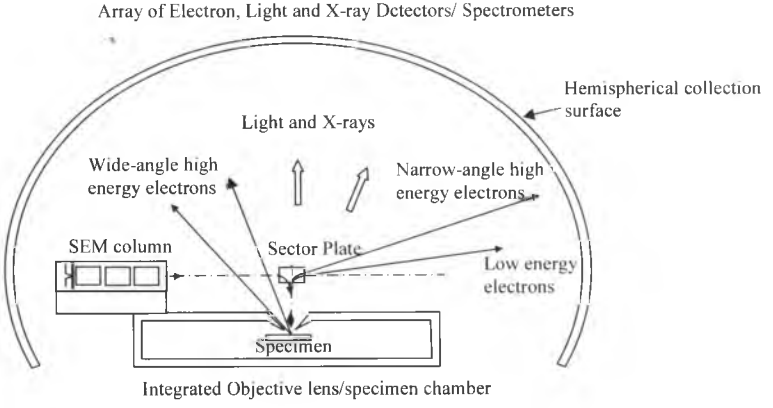

Figure 2: SPSEM layout

References

[1] M. T. Postek, Chapter 9, Handbook of Charged Particle Optics, edited by J. O. Orloff. CRC Press, New York, 1997.

COLLECTION EFFICIENCY OF THE DETECTOR OF SECONDARY ELECTRONS IN SEM

I. Konvalina and I. Müllerová

Institute of Scientific Instruments, Academy of Sciences of the Czech Republic, Královopolská 147, 612 64 Brno, Czech Republic; e-mail: kimiki@isibrno.cz

In order to collect the secondary electrons (SE), scanning electron microscopes (SEM) are equipped with the Everhart-Thornley (ET) type detector [1]. The electrostatic field of the front grid, biased to a positive potential of several hundred volts (see Fig. 1), is to attract all SE of kinetic energy below 50 eV or at least those from the SE spectrum peak at 1÷3 eV. However, the detection quantum efficiency (DQE) of such detectors has been found to be significantly lower than one [2], which is mainly given by their low collection efficiency. The electrostatic field of the grid cannot sufficiently penetrate toward the specimen and influence the trajectories of SE owing to grounded electrodes surrounding the specimen (specimen alone and its holder, specimen stage, pole piece of the objective lens, etc).

We calculated the collection efficiency (CE) of the ET detector as a function of working distance (see Fig. 2), for the arrangement shown in Fig. 1. Software SIMION ver. 7.0 [3] was used for the simulations of trajectories and equipotentials. An example of the potential distribution around the grid on a positive potential is shown in Fig. 3. The CE drastically drops down to several per cent with small working distances necessary for SEM to operate in a high-resolution mode. Results are in good agreement with the previous work [4] and also fit well our measured data of DQE [5]. The whole energy spectrum of SE was taken into account, too, but it does not influence the results too much in comparison with the case when only one SE energy (E_{SE} = 5 eV) was used. Moreover, the influence of the specimen diameter on CE was examined [6].

Now we test the impact of parameters of the grid [7] and scintillator on CE (see Fig. 4). There is no grid in the example in Fig. 5 and the scintillator of 10 mm in diameter and biased to +10 kV is simply immersed into the tube at a ground potential. Fig. 6 shows the field penetration from the scintillator (again at +10 keV) through the grid at a ground potential.

Recently, new sophisticated configurations of SE collection systems have appeared in the commercial SEMs that transport particles by electrostatic and magnetic fields toward an "in lens" detector with high collection efficiency. It is evident from the example shown in Fig. 7, that CE remarkably increases for the upper "in-lens" detector (better signal to noise ratio of the image - SNR) but unfortunately the contrast of submicrometer crystals disappears due to influence of a strong magnetic field at the specimen surface that extracts SE toward the upper detector and suppresses shadowing phenomena. High topographical contrast remains for the lower SE detector of a configuration similar to that in Fig. 1 but SNR is, of course, low. Several other examples led us to study the collection efficiency of the SE detectors in more details. [10]

[1] T.E. Everhart and R.F.M. Thornley, J. Sci. Instrum. **37** (1960) 246.
[2] D.C. Joy et al, Scanning **18** (1996) 533.
[3] D.A. Dahl, in: Proc. 43rd ASMS Conf. on Mass Spectrometry and Allied Topics, Atlanta (1996) 717.
[4] M. Balasubramanyam et al, Nucl. Instrum. and Methods in Phys. Res. **A 363** (1995) 270.
[5] L. Frank et al, in: Proc. of EMC 2004, Antwerp, Belgium, in print.
[6] I. Konvalina and I. Müllerová, Microsc. Microanal. **9** (suppl. 3) (2003) 108.
[7] F.H. Read et al, Nucl. Instrum. and Methods in Phys. Res. **A 427** (1999) 363.
[8] K. Matsuda et al, in: Proc. of EMC 2004, Antwerp, Belgium, in press.
[9] H. Kazumori, JEOL News **37E** (2002) 44.
[10] The study is supported by FEI Czech Republic, Ltd.

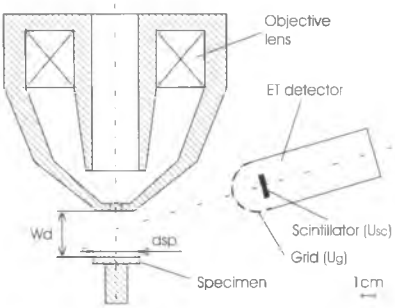

Fig. 1. Cross-section of the arrangement used in simulations. Wd is the working distance and dsp is the specimen diameter.

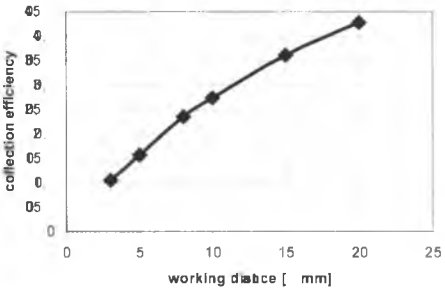

Fig. 2. Calculated CE versus Wd for E_{SE} = 5 eV, dsp = 10 mm and Ug= +300 V.

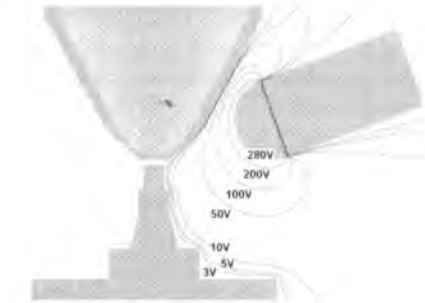

Fig. 3. Calculated equipotentials for the grid simulated by an electrode at +300 V (dsp = 10 mm, Wd = 3 mm).

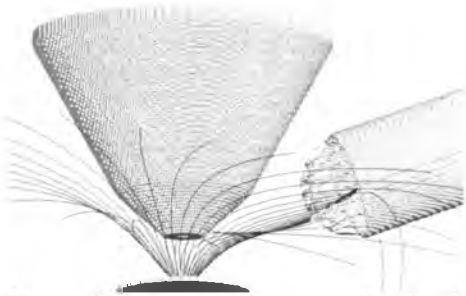

Fig. 4. 3D view of a bundle of simulated SE trajectories with true shaped wires of the grid (E_{SE}=5 eV, Wd = 20 mm, dsp = 50 mm, Ug= +300 V, U_{SC}= +10 kV).

Fig. 5. Calculated equipotentials for the scintillator at +10 kV, immersed by 10 (left) or 20 mm (right) in a grounded tube, Wd = 20 mm, dsp = 10 mm.

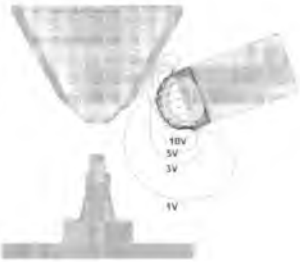

Fig 6. Penetration of the field from a scintillator at +10 kV through the grid at a ground potential.

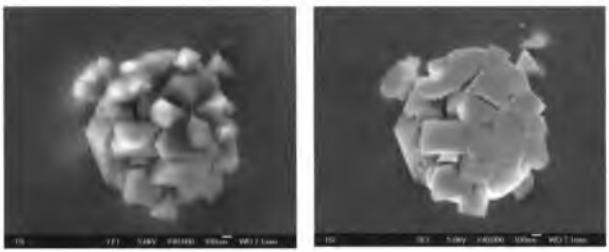

Fig. 7. Ceramic particle in the Al_2O_3/Al-Mg-Si MMC [8], taken by the standard lower SE detector (left) and by an "in lens" upper detector of SE (right) [9] in the JEOL 6700F SEM.

RECENT DEVELOPMENT OF SOFTWARE FOR PARTICLE OPTICS

B. Lencová

Institute of Scientific Instruments, AS CR, Královopolská 147, 612 64 Brno, Czech Republic, e-mail: bohunka@isibrno.cz

1. Introductory remarks

In the time of mainframe computers one of the principal reasons for writing one's own programs was the price of the software and the fact that general-purpose software was not often available. Homemade programs provided complete control over all input (data structure, interface) and output and the implementation of specific algorithms [1]. Very often they were just a product of student's work, which was not completely debugged and in no way user-friendly; this was not too serious, because the author was mostly the user of the software. Such programs were frequently short-lived, undocumented and unsupported after the student finished. This approach is certainly not optimal and it had to be changed. "Modern" computations in electron optics were largely influenced by the first order Finite Element Method (FEM) software developed by Munro, for which the source code was published [2].

With the arrival of PCs, much programming effort is being invested in interfaces, examples being SIMION based on the Finite Difference Method (FDM) [3] and CPO programs based on the Charge Density Method (CDM) [4]. The appearance of interfaces changes as operating systems develop, and backward compatibility is not completely guaranteed. The programming languages also develop with time. The programming skills of students are rather decreasing because many of the problems that had to be solved before by programming can now be analyzed with Maple, Matlab, or even Excel. In my opinion the popularity of Linux among physics students also channels their interest into a different direction. It is also difficult to oblige students to contribute to the existing software: even if they spend most of their time sitting behind a PC, they are frequently unwilling or unable to do serious programming work. For a new student the use of Fortran can be an obstacle; in reality it is rather the lack of experience in any programming language and technology and often the lack of "sitzfleisch". The size of most existing packages is also too big to allow additions.

Electron optics (EO) as such is not of great commercial interest and thus only limited funding is available. A consequence of this is that the existing software is not easy to combine with programs like AutoCAD, Matlab, Maple, or Excel. Each EO program uses a slightly different approach and terminology. It is also not simple to jump from one EO computation package to another. The EO programs are often not the primary activity of their authors, who are mostly busy with other tasks, primarily teaching and research. Also not too many citations can be made on software („program writers" tend not to cite anybody else's work, commercial users of available software often do not cite in publications their tools). Writing software has a low status because it is considered to be a routine task rather than scientific work.

Applications of EO software, ranging from detector design via computations of individual lenses to system optimization, are just too numerous to be covered by a single software package. A qualified and proper use of programs for particle optics needs some previous knowledge; in general this level of knowledge and education in particle optics is on the decrease. Most specific applications that can be analyzed with specialized EO software are not very transparent to students who prefer to use programs like SIMION, with which reasonable-looking output can be produced in a short time [5, 6].

2. Software for Particle Optics Computations

Let us now discuss briefly our set of programs called Software for Particle Optics Computations (SPOC), partly developed at ISI, TU Delft, and subsequently by the two principal authors [7]. The use of graphical user interface for the generation of input mesh, automatic generation of fine mesh, and the graphical outputs of results significantly improve the work with the programs.

The problems that can be solved with SPOC cover the field computation in 2D, the computation of optical properties and ray tracing. Fields are obtained by the first order FEM, which has the advantage that it is fast and simple. The computation accuracy is improved by using large meshes; typically the computation in a mesh with 200000 points needs around 30 seconds, mesh sizes close to one million points are possible. This is mainly because computers are getting faster; an overnight computation of Tsuno in 1985 [8] of a saturated 200 keV lens in a mesh of 6000 points can now be done in less than 1 second on a PC. Unique feature recently introduced in SPOC is the automatic accuracy estimation for field computation of rotationally symmetric elements [9, 10]. For example, the Tsuno lens computed with 80000 mesh points provides accuracy of the axial field better than 0.01 % of field maximum [11]. Multipole field components for simple electrostatic and magnetic deflectors or multipoles of quite a high-order are not difficult [12]. Another positive feature of the SPOC is that all the modules work satisfactorily, high accuracy of fields can be reached, the software is reasonably doeumented, executables for all computations are all in Fortran and thus easy to modify and compile with a new and faster compiler. It is then easy to add new features in the computations, even if they are seemingly fixed by a rigid structure of program packages. An example is a computation of two-lens electrostatic system with fixed object and image position, where we want to know the dependence of the optical properties on the voltage of one of the lenses. For this we have added an extra loop over the voltage in the computation of optical properties by shooting, which finds the voltage on the other lens, and an EXCEL output of the results. The large amount of output results is reduced to a simple table, which enables easy visualization of the results and processing of outputs. The extra loop is added within the current user interface by specifying a suitable comment in the data input: most software users do not use this comment.

Obsolete features of SPOC are the rigid structure of all the packages, consisting of several user interfaces and executables for computations that are mutually connected via a DOS batch file. Each of the packages uses a DOS interface written in Borland Pascal for FEM programs (slow graphics, low compatibility with modern graphics drivers, 32-bit Windows or LINUX, graphical outputs of geometry and results into HPGL files instead of Windows metafiles, zoom is limited on mesh lines, no output in correct ratio of r and z coordinates, no use of mouse, limit on mesh size with 200000 points), and another DOS interface for creating data for computation of optical properties and to display results. The programs were used in particle optics courses at TU Delft and Brno, so they are partly student-proof However, they require a slightly different type of thinking than common CAD programs and some off-line processing of results, so they are not very enthusiastically received by students, who seem to prefer a program such as SIMION.

Ray tracing is yet another story. One of the biggest obstacles is the need to understand well the 2D interpolation in FEM meshes by the slice [13] or ZRP [14] methods used in TRC/TRASYS package of SPOC. Ray tracing solves the particle equation of motion in any combination of focusing and deflection fields, even in the fields of higher multipole elements (quadrupoles, sextupoles and octopoles) can be used with any of the interpolation methods.

The next problem is to use efficiently the large amount of output provided by ray tracing. "Single ray tracing" of up to 20 rays with many possible outputs of trajectory and other data after some given step has the disadvantage of off-line graphics and large output files to process; graphics output needs an external 2D program SGPlot for DOS or Windows, which is no more supported. The "multi ray tracing" has as a result just the final positions available only in one selected plane and some care is needed with the interpretation of results. On the other hand, the accuracy of the ray tracing results can be very high, so that we can easily derive from the final positions the geometrical aberration coefficients of the 5^{th} order and the chromatic aberrations of the 4^{th} rank [15, 16].

A drawback of SPOC is that it is still incomplete. The programs for computations of fields of misaligned lenses and deflectors, for computations of aberrations of deflectors in electrostatic lenses or for computations of combined electrostatic and magnetic lenses with or without deflectors are still unfinished.

3. Electron Optical Design (EOD) program

A windows version of SPOC is badly needed, because "standard" user knows how to click with a mouse and expects to find everything in Help file. Unfortunately even the Windows themselves develop, e.g. a change from Windows 2000 to Windows XP for most programs written for them was not completely smooth. Compilers also change (we wanted to stay with Visual Fortran, but our compiler changed the producer from Microsoft via Digital and Compaq to Intel); their graphical possibilities improve so that the same results as with more popular C or C++ compilers can be obtained. Then there are common problems as with any software – debugging and testing of complex programs is tedious, proper documentation is boring, sufficient number of illustrative examples is a must if the programs are to be distributed.

What is EOD? As announced in 2000 [17], it was then about to be released soon. The main intention was to combine a new Windows interface with the FEM field computations as well as with the computation of optical properties and ray tracing, i.e. virtually combining all what is in the five SPOC packages in a single program written in Visual Fortran and using a lot of graphics. In reality, since then even more features were implemented, like the use of dielectric materials, Neumann boundary condition, accuracy check, 3D display of traced rays. The critical part was not the new interface; in fact it was written (by J. Zlámal) in quite a short time at the beginning of his PhD study in ISI (for the FEM programs in SPOC all four packages have their separate interface programs although most of the program features are the same). With the new interface the number of lines and points in the mesh for FEM computations is limited only by the allocated computer memory.

Ray tracing has been programmed anew. The slice method used in accurate ray tracing by TRASYS [13] was not implemented and it will probably even not be required. The ZRP method was newly programmed and recently complemented with bi-cubic and bi-quintic 2D interpolation. The variable-step 7^{th}-8^{th} order Runge-Kutta-Fehlberg method, in TRASYS rigidly implemented to comply with the required output step, can also be used in EOD as well as 4^{th}-5^{th} order variable-step Runge-Kutta procedures allowing easier interpolation of results.

Unfortunately for the release of EOD, attention was then concentrated on successful implementation of space charge computations in ion and electron beams [18]. Current effort is directed back on finishing EOD with procedures to evaluate, from ray tracing results, paraxial optical properties and aberrations as well as on implementing the "standard" procedure based

on solving paraxial trajectory equation and getting aberration coefficients from the aberration integrals.

4. Conclusions

As shown above, the development of software for electron optics in ISI is a never-ending process. New problems and applications force us to improve existing programs, to get better results from them, and from time to time we are obliged to abandon current projects aimed at filling the gaps in the software or improving it. Obviously we are also trying to catch up with the trends of using Windows, even if we are again diverted from time to time from the straight path. It also makes sense to use as much as possible other well-known tools like EXCEL to take over some of the processing of outputs.

References

[1] B. Lencová and M. Lenc, SEM 86, Part III, 1986, 897.
[2] E. Munro, CUED/Elec TR45 Report, U. Cambridge 1975.
[3] D. A. Dahl, Proc. 43rd ASMS Conf. Mass Spectr., Atlanta 1995, 717.
[4] F. H. Read, CPO-2DS program, see http://www.electronoptics.com.
[5] P. Wandrol and R. Autrata, these proceedings.
[6] I. Konvalina and I. Müllerová, these proceedings.
[7] B. Lencová and G. Wisselink, Nucl. Instr. Meth. in Phys. Res. A298 (1990) 56.
[8] K. Tsuno and K. C. A. Smith, Inst. Phys. Conf. Ser. No. 78, 1985, 121.
[9] B. Lencová, Ultramicr. 93 (2002) 263.
[10] B. Lencová, Nucl. Instr. Meth. in Phys. Res. A519 (2004) 149.
[11] B. Lencová, ISI AS CR brochure, 2004.
[12] M. Lenc and B. Lencová, Rev. Sci. Instrum. 68 (1997) 4409.
[13] J. E. Barth, G. Wisselink and B. Lencová, Nuel. Instr. Meth. Phys. Res. A298 (1990) 263.
[14] J. Chmelík and J. E. Barth, SPIE 2014 (1993) 133.
[15] B. Lencová and J. Zlámal, Proc. "Recent trends", Brno 1996, 55.
[16] M. Oral, these proceedings.
[17] B. Lencová and J. Zlámal, Proc. EUREM 2000, Brno, Vol. I, 101.
[18] B. Lencová, P. Jánský and J. Zlámal, these proceedings.

SELECTED EXAMPLES OF OUR COMPUTATIONS

B. Lencová, P. Jánský and J. Zlámal*

Institute of Scientific Instruments, AS CR, Královopolská 147, 612 64 Brno, Czech Republic. E-mail: bohunka@isibrno.cz.
*Institute of Physical Engineering, Faculty of Mechanical Engineering, TU Brno, Technická 2, 616 96 Brno, Czech Republic. E-mail: zlamal@ufi.fme.vutbr.cz.

What is EOD? The program Electron Optical Design contains interface in Windows, all programs for 2D computations by the first order FEM, ray tracing in computed fields, simulation of electron and ion sources, and computation of space charge limited beams – for further details see [1]. Most parts of the software are in the beta development phase, and they are already used in a number of projects. For example, in order to simulate properly the behavior of ion optical systems for ion beam deposition at TU Brno, the ion source computations were started by including the plasma creation inside the ion gun [2]. We can then start the computations on the plasma meniscus and take into account the emission properties of the gun as well as space charge effects in ion beams transported in the system. Intensive boron beam transport was studied with EOD as a part of a diploma project in cooperation with Salford University; the space-charge limitations were quite severe [3].

Ion sources and beam transport simulations are more critical on the proper evaluation of the space charge than electron guns and transport of beams we want to analyze for the electron beam welding applications [4], because the electrons are lighter particles and they are soon accelerated to a sufficiently high energy. First, in order to test the performance of EOD, we have checked our results on the computation of a Pierce gun used as a test 20 of CPO-2DS program [5]. Figure 1 shows the geometry of a simplified gun; proper voltages at selected points are introduced with auxiliary electrodes and the Neumann boundary condition is used on the outer radial boundary. The left part shows the beam in the first step of the iterative procedure; the current in the beam and the emitting area are adjusted automatically to provide vanishing field on the emitting surface. The final result provides the beam shown on the right-hand side of figure 1. The current transported in the gun is 9.1 μA at 10 V on anode, 98 % of the expected value [5]. In realistic electron guns we have to pay attention to the mesh used in the immediate vicinity of the emission surface in order to get accurate results. The geometry of the problem can be approximated very accurately as the number of coarse mesh lines defining the problem can be very large. There is more freedom now in the selection of the fine mesh. The mesh size is limited only by the amount of memory that can be allocated to the computations and eventually by round-off errors. The graphical outputs of EOD are also improved: figure 2 shows a cut-away 3D display of the gun geometry. The gun analyzed [4] is intended for 60 keV beams with maximum power up to 2 kW.

The EOD program is planned to replace soon the SPOC packages [1]. Before that, still more testing with all relevant examples studied before has to be done, Help must be further improved, and the evaluation of the optical properties finished.

[1] B. Lencová, these proceedings.
[2] J. Zlámal, PhD Thesis, TU Brno 2003
[3] P. Jánský, diploma thesis, TU Brno 2002.
[4] P. Jánský, B. Lencová, and J. Zlámal, Microscopy and Microanalysis 9 [Sup. 3], p. 22-23 (Proc. MC2003, Dresden).
[5] CPO-2DS program, see http://www.electronoptics.com.

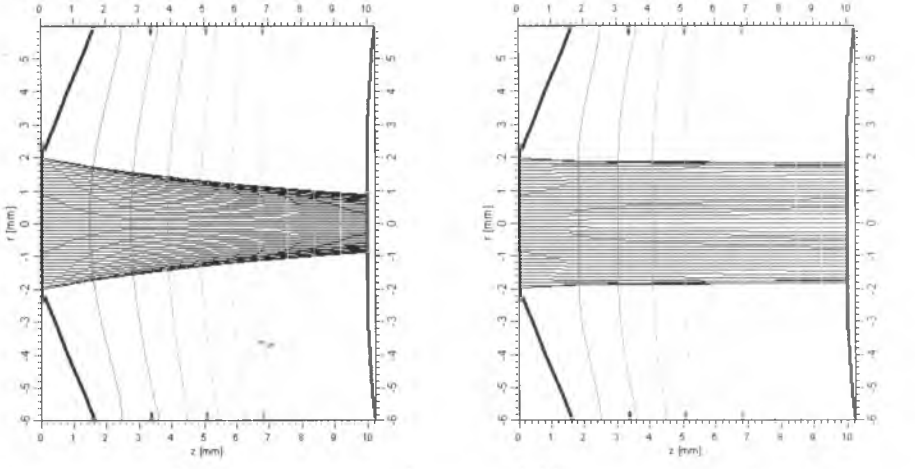

Figure 1: Computations of the cylindrical Pierce gun – initial set of electron trajectories at the left, final self-consistent result at the right.

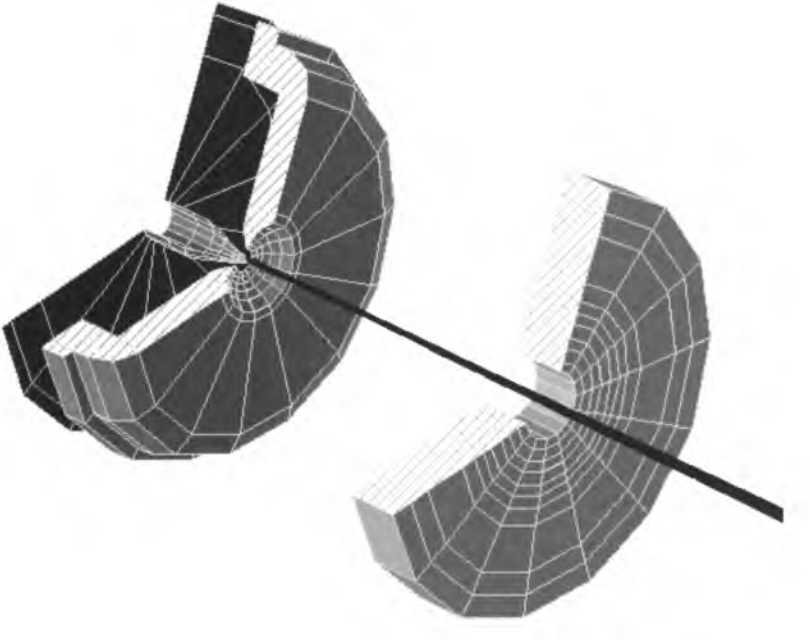

Figure 2: Cut-away 3D display of the electron gun for E-beam welding (60 kW, power 2 kW).

APPLICATION OF THE SPECTROSCOPIC LEEM IN CATALYSIS AND SENSOR TECHNOLOGY

G. Lilienkamp

Technical University of Clausthal, Institute of Physics and Physics Technologies,
Leibnizstrasse 4, D-38678 Clausthal-Zellerfeld, Gerhard.Lilienkamp@tu-clausthal.de

Within the last twenty years Low Energy Electron Microscopy (LEEM) and Photo Electron Emission Microscopy (PEEM) have been applied to numerous experiments in basic physics and chemistry. Especially LEEM and PEEM have brought new insights in fields like metal and semiconductor epitaxy, catalytic reactions at solid surfaces and magnetic properties of thin films. Due to the parallel image acquisition LEEM and PEEM have an outstanding performance in studying dynamic processes. The wide range of accessible contrast mechanisms allows the examination of the surface topography on a mesoscopic scale as well as the determination of details on the atomic level such as monoatomic steps and the local periodicity (by μ-LEED). The spectroscopic version of the LEEM has already shown its value in NEXAFS studies or imaging of characteristic photoelectrons excited by synchrotron radiation. Parallel imaging Auger electron microscopy using the LEEM gun as primary electron source is also possible. However, there is still a lack of chemical information without an access to synchrotron radiation.

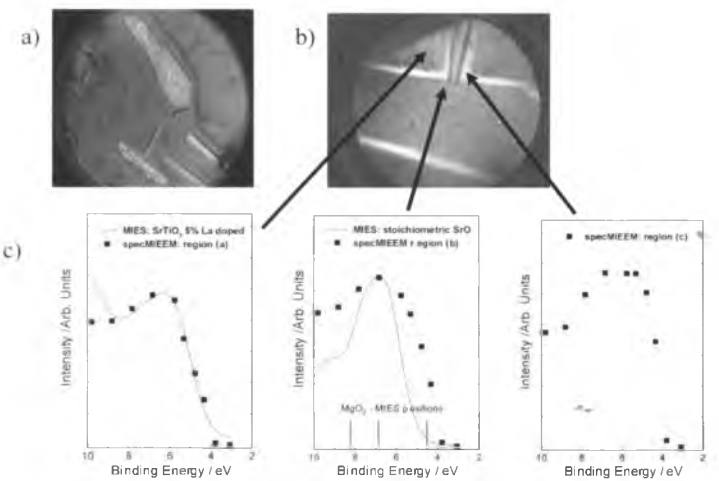

Fig.1: a) PEEM image showing the segregation of SrO islands on $SrTiO_3$. b) MIEEM image of a segregated island. Field of view 50 μm. Binding energy 13.8 eV. c) Spectra obtained from a MIEEM image series for the regions (a), (b) and (c)(see text).

In the present work we have used metastable (^{3}S) He*-atoms to excite surface valence band electrons and thereby achieve a spectroscopic contrast. We call this surface probe Metastable Impact Electron Emission Microscopy (MIEEM). Fig.1. shows a first example: images and spectra taken from a La doped $SrTiO_3$ (001) single crystal after heat treatment in ambient air at 1300°C for 120h. In the PEEM image islands of different size and contrast are clearly visible. An Auger analysis shows that these islands mainly consist of Strontium Oxide. A series of MIEEM images (one of these images is shown in Fig.1 b)) gives additional

information as can be seen in Fig.1 c). The spectra were extracted from the image sequence by integrating the intensity in different regions of interest. A comparison with spectra from known objects reveals that the SrO islands are terminated by SrO_2 and that they are surrounded by a 2-3 µm wide border zone of Ti-rich phases such as TiO_2 or Ti_2O_3 [1]. These results could not be achieved by a previous Auger investigation.
Fig. 2 shows a second application of MIEEM namely the catalytic hydrogen oxidation on a potassium precovered Rh(110) surface. The motivation of this experiment is the study of alkali promoted catalytic reactions. In principle this reaction can also be imaged by PEEM but with the presence of potassium the relation between contrast and coverage of the surface is no longer unambiguous. MIEEM makes a clear assignment possible and allows also imaging of the potassium redistribution during the reaction [2].

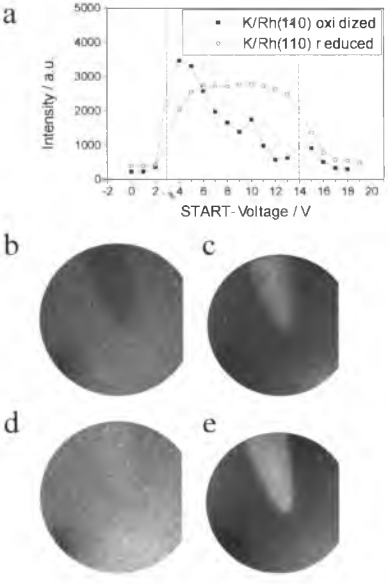

Fig.2: H_2-Oxidation on K/Rh(110). a) Electron emission spectra of the oxidized and hydrogen-reduced surface obtained by He(2^3S) excitation. b) MIEEM-image at a START-Voltage (STV) of 14 V, c) STV=3V, d) STV=6V, e) PEEM image.*

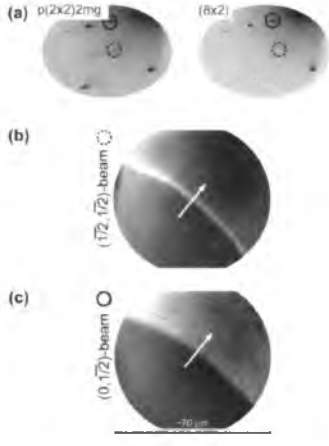

Fig.3: H_2-Oxidation on K/Rh(110). The arrow is pointing in the direction of the movement of the reaction front. a)µ-LEED patterns with different K-density, E=49eV. b) dark field image, using the (-1/2,-1/2) spot, E=29eV, the bright stripe reflects the extension of the p(2x2)2mg structure, c) same as in b) but with the (0,-1/2) beam, the bright area is reflecting the 8x2 superstructure.

Fig. 3 points out that with LEEM it is also possible to achieve information about the local distribution of the atomic order by µ-LEED and dark field imaging. That means spectroscopic data, topographical details on a nm-scale and the atomic order are simultaneously accessible from the same sample area.

References:

[1] Han Wei et al. Journal of Electroceramics, 8 (2002) 221-228
[2] G. Lilienkamp et al. Surface Science 532-535 (2003) 132-136
[3] H. Marbach, G. Lilienkamp, Han Wei, S. Günther, Y. Suchorski, R. Imbihl PCCP 5 (2003) 2730-2735

CONTRAST GENERATION IN LOW ENERGY SEM IMAGING OF DOPED SEMICONDUCTOR

F. Mika and L. Frank

Institute of Scientific Instruments ASCR, Královopolská 147, 612 64 Brno, Czech Republic.
fumici@isibrno.cz

Functional details of semiconductor structures keep decreasing in size, now to the low order of 10^2 nm. Among the structure elements the locally doped patterns play crucial role so that tools are needed for their observation. For fast diagnosis and quality check of the semiconductor structures the scanning electron microscope is useful because of its wide range of magnification, availability of different signal modes, speed of data acquisition and non-destructive nature of the technique in general, especially at low voltage operations. The dopant concentration in semiconductor is quantitatively determined via acquisition of signal of the secondary electron (SE) emission [1] in such a way that the image contrast is measured between areas of different type or rate of doping.

The contrast mechanism was assigned to presence of external patch fields above the specimen surface [2], which balance the local differences in the inner potential connected with the doping. The new theory relies upon subsurface fields formed between semiconductor and the carbon contamination layer, which behaves similarly to a metal and grows on the specimen surface owing to electron impact under standard vacuum conditions [3,4]. Evidences have been collected about crucial influence of surface overlayers on the contrast, however suspicion has arisen that the contrast formed in this way is not inherent to all SE emission but exhibits some angular sensitivity. A part of the study reported here was oriented to determining the relation between the p/n contrast and the polar angle of signal emission.

By means of the standard side-attached Everhart-Thornley detector, the range of acceptance in polar angles can be varied by changing the working distance - this was checked by 3D simulation of the signal electron trajectories by means of the SIMION 7.0 program package (see Fig. 1A,B). Evidently, at larger working distances smaller polar angles (taken from the surface normal) are accepted. Experiments were made on boron-diffused p^+ type patterns into phosphor doped n type Si (111) substrate with the surface passivated by etching in HF. The device was CFE SEM JEOL 6700F at the primary energy 1 keV. Micrographs in Fig 2 show a strong dependence of the contrast on the working distance, namely its decrease toward longer working distances, inversion and increase to high levels with the p type brighter, as anticipated on the basis of previous results [4].

Further confirmation was sought by repeating the experiment in other two SEMs with different working distances and detector geometries (Tescan 5130 Vega and Tesla BS 343) and the contrast was measured in dependence of the electron energy. Fig. 3 shows again much higher contrast at a long working distance. High p/n contrast with p type brighter is obviously concentrated to low polar angles of the SE emission, which is in accordance to the model relying upon subsurface fields streaming the slow electrons toward surface.

References:

[1] Perovic, D., D. et al. *Ultramicroscopy.* 1995, vol. 58, p. 104-113.
[2] Sealy, C., P. et al. *Journal of Electron Microscopy* 2000, vol. 49, p. 311-321.
[3] El-Gomati, M. M., et al. *IEEE Transactions: Electron Devices.* 2004, vol. 51, p.288-292.
[4] Müllerová, I., El-Gomati, M..M., Frank, L. *Ultramicroscopy.* 2002, vol. 93, p. 223-243.
[5] Support of GA CR under the Programme for Support of the Targeted Research and Development, no. S2065301, is gratefully acknowledged.

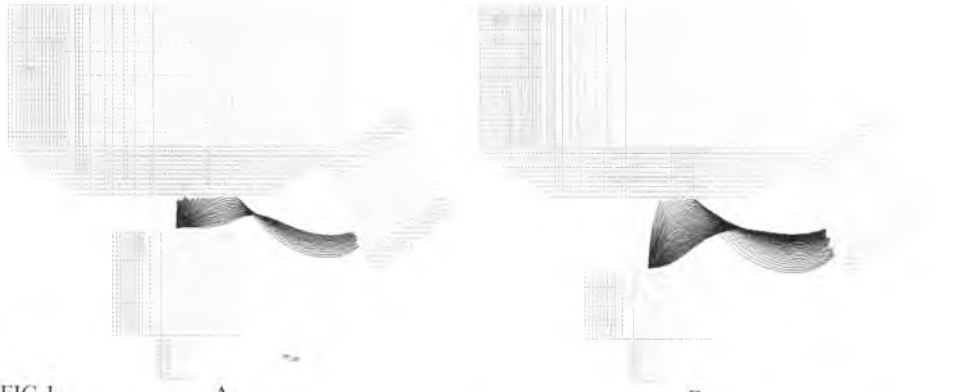

FIG 1 A B

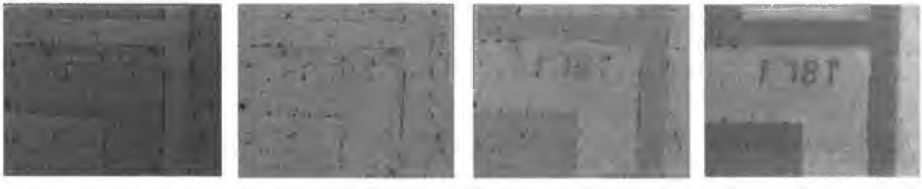

FIG 2

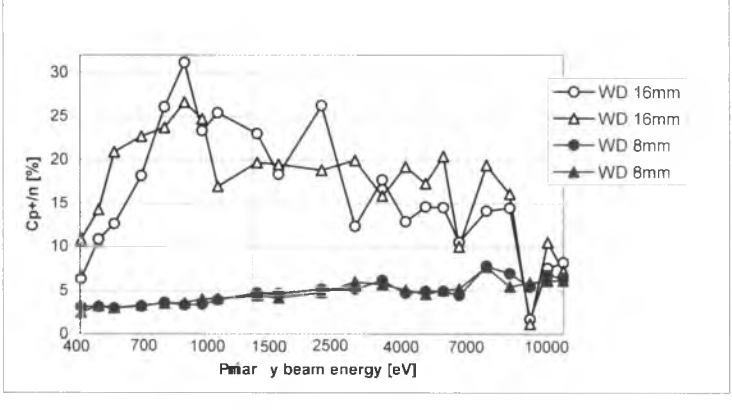

FIG 3

FIG 1: 3D simulation of the signal electron trajectories with SIMION 7.0 for two different working distances.
FIG 2: Patterned boron diffusion into n type Si (111) substrate, imaged with the "lower" ET detector in JEOL 6700F SEM at 1 keV for the working distances (from the left) 8.3, 14.4, 18.7 and 22.9 mm.
FIG 3: The energy dependence of the P/N contrast for two different working distances (approx. 8 and 16 mm).

CALCULATION OF CURRENT DENSITY PROFILES OF CHARGED-PARTICLE BEAMS

Martin Oral

Institute of Scientific Instruments, AS CR Brno, Czech Republic

Today, when computers become faster, it is possible to simulate the behavior of a great number of particles in a beam. Direct ray tracing through an optical system is very accurate, but still slow for some simulations, even with up to 100 particles calculated in a second. The calculation of particle positions in a spot profile with the use of aberrations gives information about a few millions of particles per seconds. It is still not feasible to deal with every single particle in a real beam, but the available computing power allows us to analyze an ensemble adequately representing all particles in the beam. Then we can calculate a current density profile in a beam with a high accuracy. For this purpose, a program was developed.

A simple algorithm of the profile computation was developed and tested. The method assumes a general particle source of finite size and energy width and an optical system with deflectors. The profile is recorded in a given plane perpendicular to the optical axis.

Real sources emit particles from a finite area with a given density in coordinates, slopes and energy. The method assumes the source to be defined in a plane at z_o with coordinates x_o and y_o and slopes x'_o and y'_o with energy E (figure 1). In general, the density distribution function of the source is therefore a function of all those coordinates, slopes and energy. The program assumes that the density function is separable, i.e. a product of three functions of only coordinates, only slopes and only energy. The considered source is rotationally symmetrical. In addition, the Gaussian distribution $g_0(t) = (1/\sqrt{2\pi}\sigma)\exp[-t^2/(2\sigma^2)]$ with $\sigma = \mathrm{FWHM}/\sqrt{8\ln 2}$ is used for coordinates and energy, the distribution in slopes is expected to be uniform within a given aperture angle. The overall density distribution function of the source is (written without the respective FWHMs)

$$g(x_o, y_o, x'_o, y'_o, E) = g_0(\sqrt{x_o^2 + y_o^2}) \cdot [(z_a - z_o)/(\pi R_a^2)] \cdot g_0(E - E_0),$$

where E_0 is the mean energy of the beam and the term in the square brackets is the reciprocal solid angle, to which particles are emitted, with the assumption $R_o << R_a$. It is the distribution in slopes, z_a is the position of a (virtual) aperture, R_a its radius.

The optical system is described by transfer matrix and aberration coefficients (calculated i.e. with [6]), geometrical aberrations of the third order and chromatic aberrations of the first order are assumed [1-5]. The positions in the desired target plane are calculated as a paraxial position plus the aberrations. The aberration formulas used in the program can be found in [2] and in manuals [3]. For systems with small starting positions x_o and y_o the computation of off-axial aberrations can be switched off to speed up the simulation slightly.

The profile computation begins with the division of the planes in the source, in the aperture and in the target into small regions (figure 1); the energy range is subdivided into sufficiently small intervals. Then from a center of a square on the source is started a test particle, whose direction is chosen to go through centers of all of the squares on the aperture. The position of the particle at the target is calculated with the aberration expression and its current is added to an appropriate square on the target. The initial energies of the particle are set to mean energies of single energy subintervals. The energy division is made so that each k-th subinterval has the same energy volume, i.e. $\int_{E_k}^{E_{k+1}} g(E - E_0)\,\mathrm{d}E = \mathrm{const}$. The current contribution ΔI of that test particle corresponds to current contributions of all the particles that would travel from the same source square, through the same aperture square with energies

from the same subinterval, so $\Delta I = Ig(x_o, y_o, x'_o, y'_o, E)\Delta x_o \Delta y_o \Delta x'_o \Delta y'_o \Delta E$, where I is the total current of the beam at the target. The deltas are steps in the division of corresponding quantities. The product $\Delta x'_o \Delta y'$ is the elementary solid angle (the pyramid in the figure 1). The profile is finished after this procedure has been done for all the possible combinations of squares and energy subintervals. Only squares within the radii R_o and R_a are considered in the computation. Results of current density profiles computed with the method are in figure 2. [8]

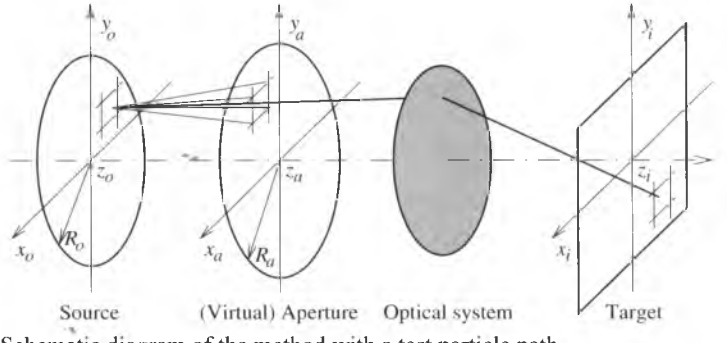

Figure 1: Schematic diagram of the method with a test particle path.

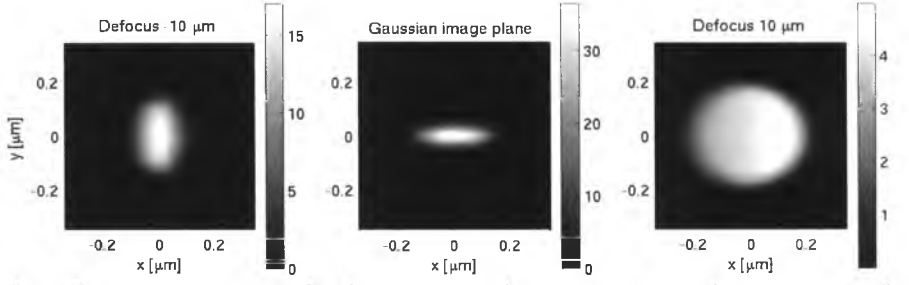

Figure 2: Calculated beam profiles in an electrostatic two-lens system with double deflection and 10 mm working distance. The mean energy of the beam is normalized and set to 1 eV, energy FWHM is 0.5 meV, and the virtual size of the ion source (FWHM in coordinates) is 50 nm (a typical value [7]). The aperture angle is 1 mrad. The deflection distance is 432.36 μm, centers of the defocused spots are shifted by ± 0.65 μm. The gray-level bars show normalized beam current density $j(x,y)/I$ in μm^{-2}.

[1] E. Munro, H. C. Chu: Numerical analysis of electron beam lithography systems, Part I: Optik 60, No. 4 (1982) 371-390, Part II: Optik 61, No. 1 (1982) 1-16, Part III: Optik 31, No. 2 (1982) 121-145, Part IV: Optik 61, No. 3 (1982) 212-236

[2] B. Lencová, M. Lenc: Computation of properties of electrostatic lenses. Optik 97, No. 3 (1994) 121-126

[3] B. Lencová: Programs for particle optics computation (ELD, Eprop, Prop, Combi), version 3.70 user manuals, Brno 2002

[4] B. Lencová, Trasys 3.70 user manual, Brno 2002

[5] J. Orloff et al: Handbook of Charged Particle Optics, CRC Press LLC, 1997, ISBN 0-8493-2513-7

[6] M. Oral, B. Lencová: Calculation of Aberration Coefficients by Ray Tracing, Microscopy and Microanalysis 9 [Sup. 3] - S. 26-27 (2003)

[7] J. Orloff et al.: Handbook of Charged Particle optics, CRC Press, 1997, ISBN 0-8493-2513-7

[8] Supported by the project KSK 2067107.

AN ADD-ON SPECTROMETER/LENS-SECTOR PLATE ATTACHMENT FOR THE SEM

M. Österberg and A. Khursheed

National University of Singapore, 4 Engineering Drive 3, Singapore 117576.
eleka@nus.edu.sg

This paper presents a magnetic spectrometer/lens unit intended to acquire both image as well as spectroscopy information inside a SEM. The unit is small enough so that it can be placed inside the specimen chamber as an add-on attachment and comprises of deflection plates that function together with a low aberration add-on miniature permanent magnet immersion lens [1].

Although various spectrometers have been previously proposed for the SEM in the context of techniques such as voltage contrast, auger analysis and depth profiling, they do not presently exist as SEM add-on attachments, nor are they capable of capturing the full energy spectrum, from the low energy secondary electrons to the elastic backscattered electrons. Not only does the attachment proposed here aim to acquire high resolution spectral information over the entire energy range, but it also aims to capture high resolution topographic images, typically in the nanometer resolution range.

The attachment proposed in this paper works by providing a stigmatic-free 90 degrees deflection of the primary beam in the SEM. In this respect, it resembles the LEEM setup [2]. The deflector unit works much like a round lens and can give magnification or demagnification of the probe. Normally one thinks of magnetic deflection as only being able to focus an electron beam in a plane parallel to the deflector plates, called in-plane focus. However, by making use of the fringe fields that are always present at the edges of magnetic sector plates, one can obtain out-of-plane focusing of the beam if it is inclined non-perpendicularly to the plate edge. The idea is then to put the permanent magnet objective lens on its side so that the deflected primary beam enters it horizontally, striking the specimen which is located inside it. The add-on lens can provide demagnification of greater than 10.

If the specimen is negatively biased to a value close to that of the beam energy (i.e. creating a retarding electric field) electrons emitted from the specimen will be accelerated back towards the deflector unit. The strong fields inside the lens will collimate the scattered electrons so that most of them will enter the deflector unit. On traversing the magnetic sector fields, the scattered electron will be bent in a direction away from the incoming primary beam. An auxiliary pair of magnetic sector plates then turn the scattered electrons in a preferred direction, typically towards the scintillator detector in the SEM. If now the strength of this auxiliary sector plates is ramped and a slit is put between the deflection unit and detector, it is then possible to acquire the energy spectrum of the scattered electrons.

A test experiment is performed in a conventional SEM to investigate the add-on spectrometer concept outlined above. The setup is shown schematically in Figure 1. The deflector unit is controlled by four electromagnetic sector plate pairs. Focusing conditions and the direction of the outgoing beam is determined by individual currents in each of the electromagnetic coil

pairs. In-plane focusing comes from the combined deflection of magnetic fields in sectors 1, 2 and 3. Out-of-plane focus on the other hand is mainly determined by the ratio of the magnetic field strength in sector 1 to that in sector 2 and similarly magnetic field strength in sector 3 to that in sector 2. The magnetic field strength of plates 4 is ramped in time and the normal SEM scintillator/photomultiplier detector (not shown) is used to acquire the scattered electron spectrum.

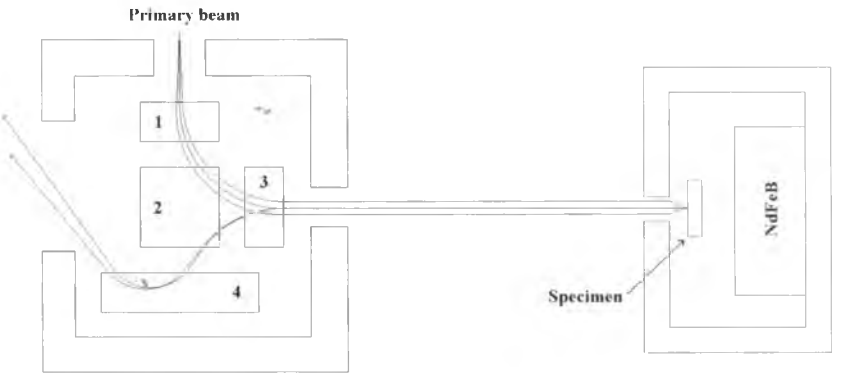

Figure 1: Schematic of the spectrometer/lens unit setup. 1) pre-deflection plates, 2) main deflection plates, 3) post-deflection plates and 4) auxiliary plates.

In the initial experiments, a JEOL JSM5600 tungsten gun SEM is operated with 6 keV primary beam energy. It is found that a magnetic field roughly three times stronger in sectors 1 and 3 compared to sector 2 gives a stigmatic free image. By varying the cross-over position above the deflector unit and at the same time adjusting the magnetic field strengths in the deflection plates, the focal position of the primary after traveling through the deflection unit can be varied. So far it has been operated as a projector lens, resulting in a parallel beam entering the add-on lens, as shown in Figure 1.

Initial results from the add-on SEM spectrometer/lens unit operating inside a conventional SEM will be presented at the conference.

References

[1] A. Khursheed, N. Karuppiah, and S. H. Koh, Scanning, **23**, (2001) p204-210.
[2] R. M. Tromp et al., Surf. Rev. Lett. **5**, (1998), p1189-1197

SYSTEM PERFORMANCE OF A DEDICATED LOW ENERGY FOCUSSED ION BEAM SYSTEM

Michael Rauscher and Erich Plies

Institute of Applied Physics, University of Tuebingen, Auf der Morgenstelle 10, D-72076 Tuebingen, email: michael.rauscher@uni-tuebingen.de

Low energy ($\leq$ 3 keV) focussed ion beam milling can provide a useful tool for the preparation of cross-sectional samples for transmission electron microscopy, for example for *in-situ* reworking of amorphisized specimens in the TEM [1]. Due to the increasing influence of the chromatic aberration spot size contribution in low energy operation some effort has to be made in order to keep the total spot size sufficiently small and the corresponding spot current density sufficiently large, respectively.

The design and favourable mode of operation of a dedicated low energy focussed ion beam system based on immersion optics is presented. The beam is accelerated using a gun lens and the intermediate lens space is on high potential [2]. Beam retarding is accomplished within the objective lens. With this design the target is field free and can be kept on ground potential. This indeed is very similar to the basic operation principle of many modern scanning electron microscopes [3]. As all deployed voltage-levels are comparatively low, both condenser as well as objective lens can easily be operated in the internal acceleration mode, consequently improving their general optical performance [4]. In order to keep the working distance to a minimum and avoiding the technical difficulties of dynamic electrostatic deflection on high potential, beam scanning is realised using a split final objective lens electrode. Figure 1 shows an outline of the system design together with a sketch of the potential distribution.

Figure 2 shows the system performance in terms of spot size d vs. beam current I for a beam energy of 3 keV and an immersion ratio (ratio of booster potential to final beam potential) of $\Phi_{booster}/\Phi_i = 8/3$. Both, the results of third order optical analysis (using the RPS-algorithm [5]), as well as data from direct ray-tracing (obtained using the IMAGE software package [6]) with and without Coulomb interactions are shown. As expected, the influence of interactions is a major limiting factor for the achievable minimum spot size. Further analysis of this effect will be presented.

References:

[1] P. Gnauck, Dissertation, University of Tuebingen, 2000.

[2] K. Pak, I. Saitoh, N. Oshima, H. Yonezu, J. Crystal Growth 140, 244 (1994).

[3] S. Beck, E. Plies, and B. Schiebel, Nucl. Instr. Meth. Phys. Res. A 363, 31 (1995).

[4] W. Driesel, Ultramicroscopy 52, 65 (1993).

[5] J.E. Barth, P. Kruit, Optik 101, 101 (1996).

[6] Programs used for calculations: OPTICS and IMAGE packages by MEBS Ltd.

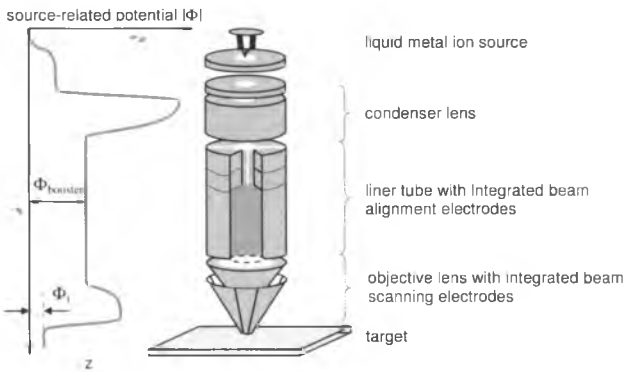

Figure 1: Schematic drawing of immersion optical system and source-related axial potential Φ.

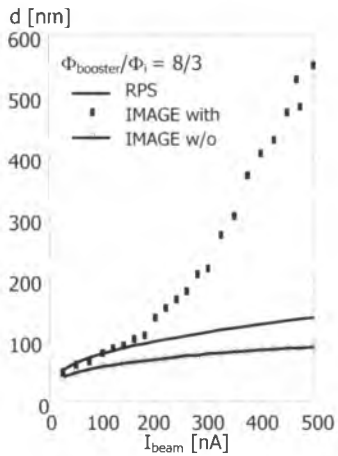

Figure 2: System performance in terms of spot size d vs. beam current I for the immersion optical focussed ion beam system at a final beam energy of 3 keV and a working distance of 15 mm. Source data assumed for the calculation: source size 50 nm, angular intensity 10 μA/sr, full energy width 5 eV.

THE ULTIMATE ACCURACY OF THE BEM FOR ELECTROSTATICS

Frank H. Read

Department of Physics and Astronomy, University of Manchester, Manchester M13 9PL, UK
e-mail address: Frank.Read@ieee.org

In the present study we consider the limitations to the ultimate accuracy of the BEM (Boundary Element Method) for 3D electrostatic systems, with and without space-charge. It seems useful to do this because the BEM (also known as the Integral Equation, Surface Charge or Charge Density Method) is known to be usually faster and more accurate for such systems than other methods. Some evidence for this is provided by a comparison of 8 different benchmark tests carried out in 1997 and 1999 [1,2] when it was shown that for computing times of the order of 1000s on a 100MHz Pentium PC the BEM program CPO [3] was of the order of 10 to 100 times more accurate than the best FDM (Finite Difference Method) or FEM (Finite Element Method) programs [4-6] available at that time.

The sources of inaccuracy for systems that do not involve a cathode or space-charge are (1) the finiteness of the number N of segments into which the electrodes are subdivided, (2) imperfections in the shapes of the segments, (3) imperfections in the distribution of charge density on the segments, (4) the existence of field singularities, (5) the approximations used in evaluating the potentials and fields due to the segments, (6) numerical inaccuracies in inverting the relevant matrix and (7) machine inaccuracies.

Additional sources of inaccuracy for systems that involve a cathode and/or space-charge are (1) the finiteness of the number M of trajectories, (2) the inaccuracies in simulating the space-charge cloud in front of a flat thermionic cathode, (3) the approximations used in generalizing to a cathode that is curved or not fully saturated, (4) the inaccuracies in assigning the space-charge of trajectories and (5) the inaccuracies in calculating the potentials and fields due to the space-charges of the cathode and trajectories.

These sources of inaccuracy will be carefully considered for a variety of electrostatic problems, including (1) calculations of capacitances and associated singularities, (2) comparisons of potentials and fields with known analytic solutions, (3) calculations of lens parameters and (4) calculation of the parameters of energy and mass spectrometers and ion traps.

References

[1] D. Cubric, B. Lencova and F. H. Read, Electron Microscopy and Analysis 1997, Institute of Physics Conference Series vol. **153** (1997) 91.
[2] D. Cubric, B. Lencova, F. H. Read and J. Zlamal, *Nucl. Instrum. Meth.* **A427** (1999) 357.
[3] CPO programs, available on the web site http://www.electronoptics.com/
[4] SIMION Program, information available at http://www.srv.net/~klack/simion.htm
[5] SIM3D Program, information available at http://fyzika.fme.vutbr.cz/~zlamal
[6] ELENS Program, information available at http://www.isibrno.cz/~bohunka

SIMULATION OF ELECTRON AND ION SOURCES

Frank H. Read[a] * and Nicholas J.Bowring[b]

[a]Department of Physics and Astronomy, University of Manchester, Manchester M13 9PL, UK
[b]Department of Engineering, Manchester Metropolitan University, Manchester M15 6BH, UK
*e-mail address: Frank.Read@ieee.org

Simulation of thermionic cathode space charges when the Langmuir-Child law is valid

In the simulation of cathodes by the Boundary Element Method (BEM) the surface of the cathode is effectively replaced by a sheet of charge that lies on the surface and that is subdivided into segments. We now describe for the first time the technique used in the CPO programs [1] since 1994 to simulate the behavior of thermionic cathodes.

The simplest example is the space-charge limited current of a planar diode when the cathode temperature T is zero and the current density is given by the Langmuir-Child Law [2,3]. The essence of the present method is to divide the total charge Q in a cathode region of depth d into N regions that each have the charge Q/N and then to replace these distributed charges by thin sheets of charge at the centres of the regions. This is illustrated in Fig. 1, for $N = 4$. The only description of a similar technique seems to be that of Andretta *et al* [4] who used a single sheet that carries the whole charge density Q, placed at the cathode itself.

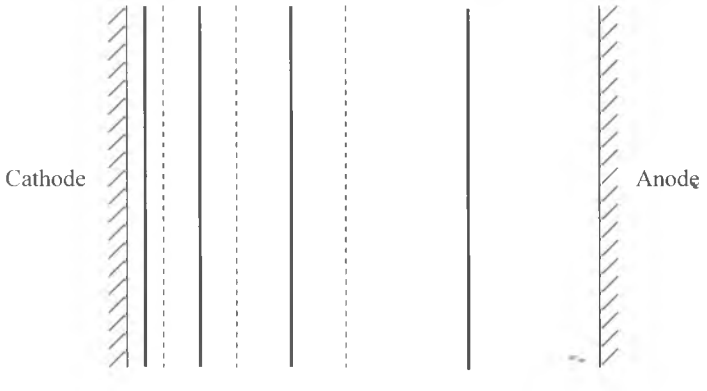

Figure 1. Schematic illustration of the positions of 4 charge sheets, indicated by bold lines, that replace the space charges in the regions enclosed by the broken lines. In practice the first sheet would lie much closer to the cathode than indicated here.

The field produced by the N sheets is piece-wise linear between the cathode and anode and it can be shown that the values of the field, and also of the potential, are correct at the boundaries of the regions.

In the practical implementation of this [1] the full simulation of a system that contains cathode and other space-charges is of course iterative. The trajectories in any given iteration use the space-charges, including those in the cathode region, produced in the preceding iteration.

Another aspect of the practical implementation is that the planar cathode surface is subdivided into triangular or rectangular segments. The procedure outlined above is followed separately for each of the cathode segment. The corresponding sheets of charge for a given cathode segment then have the same size and shape as the parent segment. Non-uniformities in the field applied to the cathode can therefore easily be dealt with.

Treatment of curvature of cathode surface

We distinguish three regions: the first is the 'inner cathode region' that contains the cathode space-charge segments discussed above, the second is the 'intermediate cathode region' that contains a further set of segments and the third is the 'outer region' that contains the space-charge cells or tubes that hold the space-charges of the trajectories for the whole of the rest of the system being simulated. This is illustrated in Fig. 2.

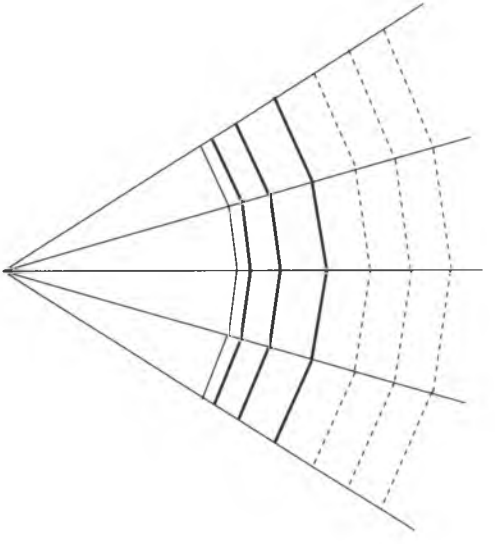

Figure 2. The transverse thin, bold and dashed lines represent the segments of the cathode itself, the 'cathode space-charge' region and the 'intermediate space-charge' region respectively.

The segments in the inner cathode region have the same shapes as their parent cathode segments but are expanded to fill the same solid angle subtended by the parent segment. By solving Poisson's equation for a cylindrical or spherical diode we have been able to generalise the above treatment for planar cathodes to obtain the charges on these segments.

The intermediate cathode region exists only for convex cathodes. Its purpose is to match the inner cathode region to the outer region, which is essential when the cathode radius is much smaller than the dimensions of the space-charge cells or tubes. If a trajectory crosses one of the segments in this region then the appropriate charge is assigned to the segment.

Simulation of thermal energy effects

Langmuir [5] has given a careful treatment of the effects of the initial thermal energy spread of the emitted particles on the space-charge distribution and current from planar cathodes. In general the space-charge cloud in front of the cathode creates a potential minimum V_m that reflects electrons of lower energy back into the cathode surface and thus reduces the current that reaches the external region. This minimum becomes the effective source and is known as the virtual cathode.

We use an iterative procedure to obtain a self-consistent solution of the Langmuir equations to establish the current density and the depth and position of the potential minimum. Then the charge in each sub-region is integrated and assigned to the corresponding cathode space-charge segment. The velocity distribution of the trajectories that pass the potential barrier V_m -*ie* that are emitted by the virtual cathode- is assumed to be Maxwellian.

An example of the near-cathode potential distribution obtained by this procedure is shown in Fig. 3. Here a planar diode is simulated for a cathode that has $kT = 0.1eV$ and for a field that is $10V/mm$ in the absence of space-charge The results obtained with three different values of the number N of cathode space-charge segments are shown. At the highest value of N used here the potential and position of the virtual cathode have converged approximately to the values obtained by applying Langmuir's method analytically. Another test of the technique is of course the value of the current density j that reaches the anode. Here j is approximately 1% larger than the accurate value obtained analytically.

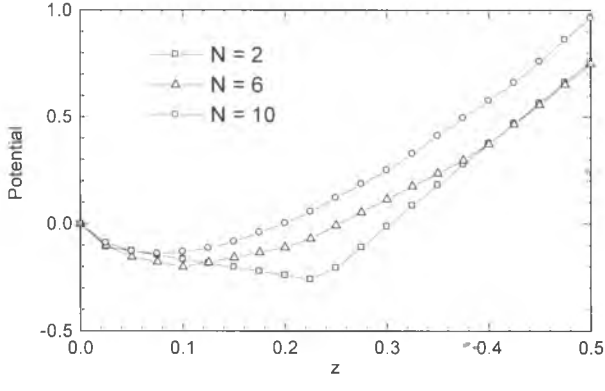

Figure 3. Potential distribution as a function of the distance z, in *mm*, in front of a planar cathode that has $kT = 0.1eV$, obtained with the CPO3DS program, showing the existence of the virtual cathode. Results are shown for three values of the number N of cathode space-charge segments.

Simulation of liquid metal ion sources

These sources are capable of producing currents of a few μA from source diameters of a few *nm* [6] but the effects of stochastic ion-ion scattering tend to increase the final energy spread by several eV. We have used the CPO3DS program to model the stochastic scattering,

using a generalization of the technique described previously [7,8] for stochastic scattering of electrons in field-free regions.

In the first example we have modeled a liquid gallium source of radius $5nm$ that has a field of $10V/nm$ at its surface. The space-charge in front of the cathode is of course of negligible importance at such high fields but there are some other effects that cause this modeling to be exceptionally difficult..

The principle difficulty is that the conditions in front of the cathode change very quickly with distance. Within the first $5nm$ the ion velocity increases by a factor of approximately 5 and the charge density decreases by a factor of approximately 20. The most violent ion-ion scattering events therefore take place mostly within the first few *nm*. In this region it is therefore necessary to use short step lengths for trajectory integration, small radii for the space-charge tubes that contain the trajectory charges and small distances for averaging the space-charge density that is needed for the calculation of stochastic scattering. As the ions recede from the cathode surface these various lengths must be allowed to increase appropriately, so that the total number of trajectory steps is not excessive and the space-charge averaging remains sufficiently accurate. In this first example these various lengths have been increased in 9 controlled stages between the cathode and anode.

The results of this simulation will be presented at the conference.

References

[1] CPO programs, available on the web site http://www.electronoptics.com/

[2] P. W. Hawkes and E. Kasper, "Principles of Electron Optics," Academic Press, New York, 1989

[3] M. Szilagyi, "Electron and Ion Optics," Plenum Press, New York, 1988

[4] M. Andretta, M. Marini and G. Zanarini, IEEE Trans. El. Dev. **ED-13** (1986) 1084-1089.

[5] I. Langmuir, *Phys. Rev.* **21** (1923) 419-435.

[6] J. Orloff, *Rev. Sci. Instrum.* **64** (1993) 1105.

[7] F.H. Read and N.J.Bowring, *Rev. Sci. Instrum.* **74** (2003) 2280-2287.

[8] F.H. Read and N.J.Bowring, *Nucl. Instrum. Meth.* **A519** (2004) 196-204.

ELECTROSTATIC LOW ENERGY SCANNING ELECTRON MICROSCOPE FOR AUGER ANALYSIS

V. Romanovský, M. El-Gomati, L. Frank*, I. Müllerová*

Department of Electronics, University of York, York YO10 5DD, vr3@ohm.york.ac.uk
*Institute of Scientific Instruments AS CR, Brno, Czech Republic

A scanning low energy electron microscope (SLEEM) was realized with a cathode lens in which the negatively biased specimen is used as the cathode. In this arrangement, electrons pass through the microscope at high energy and are decelerated to low energy before landing on the sample. Signal electrons are accelerated back to the detector, which is part of the column. This design brings plenty of signal even in the landing energy range of tens or units of eV. This is comparable with the known LEEM method. In many cases the contrast itself and its variation, as a function of electron energy, does not bring enough data for reliable image interpretation. Moreover, exploitation of low-energy electrons enables observation of differently doped semiconductor regions [1]. However, the use of the primary electrons with low energy brings some problems e.g. low source brightness, increased aberrations and sensitivity to stray fields (i.e. defocusing the probe by SE collecting field) [2]. The scanning Auger microscopy (SAM) is well-established experimental method. Surface elemental mappings in SAM could be affected by artifacts due to surface topography and subsurface atomic number variations. A combination of SAM and SLEEM in one device would therefore provide a sufficient tool to solve the problems inherent in these individual methods. Although much has already been achieved in the area of detection of slow electrons, none of the methods currently known is suitable to be built into a scanning illumination column for Auger microprobe analysis.

Fig. 1. New scanning low energy electron microscope accommodated in the CMA

Figure 1 shows the high resolution and fully electrostatic mini-column accommodated inside the cylindrical mirror analyser. The column has a diameter of only 45 mm and is 85 mm long. Operating beam voltage is up to 10 kV. A Schottky emitter is used as the source. The cathode, suppressor and extractor are constructed as one pre-aligned module with dimensions 20×20 mm (provided by YPS [4]). This configuration insures very high precision of mechanical alignment. In the middle of the column is a built-in detector for low energy electrons, which consists of a mirror lens, microchannel plate and detection electrodes. The detector is shown in Fig. 3. It is divided into six equal segments covering 360° angle. In the middle of the mirror lens is a small aperture with two important functions: deflecting signal electrons onto the detector and acting as the primary beam-limiting aperture. Between the cathode module and mirror lens is another lens with a system of alignment deflectors. This allows the microscope to be used in two different modes. In the high-resolution mode, the

crossover is created before the limiting aperture and only electrons on the axis are used for imaging. In the high current mode the crossover is created in the aperture and nearly all the electrons hit the sample. In this mode we can deliver sample current around 45 nA. For the scanning, an 8-pole electrostatic, double stage deflection system is used, giving field of view around 1 mm for working distance of 5 mm.

All six segments of the detector are connected with special preamplifiers by subminiature gold plated relays. These relays are driven by a microprocessor and allow channels to be joined together in any possible combination. The amplifiers float on a potential and are connected through opto-isolation amplifiers directly with a high-speed computer card. Maximum scanning resolution is 4096×4096 points. All inputs have resolution of 16 bits. They are able to resolve over 65,000 levels of input signal. The new software displays all six channels at the same time. It is possible to observe large differences in images from each channel, especially for low energy imaging. Fig. 5 shows an image of gold particles on a carbon substrate in RGB mode. Signals from opposite channels were subtracted [3], each result was converted to a different RGB colour and the results combined to form a colour image. Micrographs created in this way highlight edge effects in different colours depending on which detector they face. A large increase in topographic contrast can be observed in comparison with Fig.4 which shows the same sample imaged using summation of signals from all six channels in RGB mode. Figure 2 shows the Auger spectra taken with CMA from the same sample.

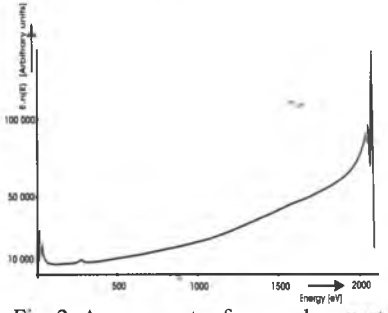

Fig. 2. Auger spectra from carbon part of the sample on Fig 4, E_p=2100eV

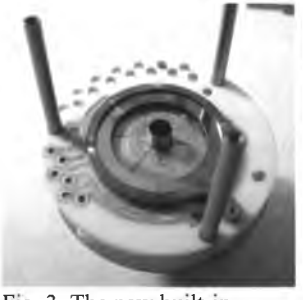

Fig. 3. The new built-in 6-channel detector.

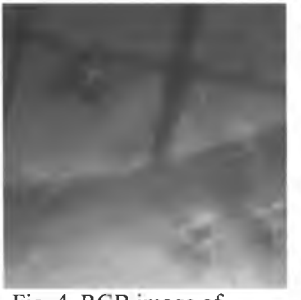

Fig. 4. RGB image of summed signals from all channels, Au/C testing specimen, energy 500eV, field of view 0.5 mm.

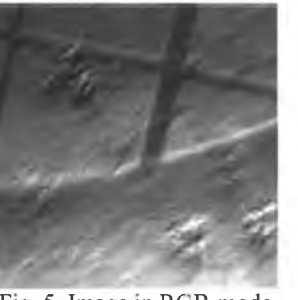

Fig. 5. Image in RGB-mode showing increased topographic contrast.

[1]. Perovic, D.D. et al, Ultramicroscopy 58 (1995) 104.
[2]. Frank, L., Mullerova, I., El-Gomati, M., Ultramicroscopy 81 (2000) 99.
[3]. Reimer, L.: Scanning Electron Microscopy, Springer 1998, p.230.
[4]. York Probe Sources Ltd. http://www.yps-ltd.com
This project was supported by the Royal Society (UK).

EXPERIMENTAL AND SIMULATIVE METHODS FOR SCINTILLATION DETECTOR OPTIMIZATION

P. Schauer and R. Autrata

Institute of Scientific Instruments, AS CR, Brno, Czech Republic, petr@isibrno.cz

In S(T)EM an image is formed using a focused electron beam, which is scanning across a very small part of the specimen surface. A scintillation detection system consisting of a scintillator, light-guide and photomultiplier (PMT) processes only one pixel of the image at any given moment. Not only efficiency, but also kinetic properties of such a system are of great importance. Scintillation detectors can show a noticeable difference in detective quantum efficiency (DQE) due to the bad electron-photon energy conversion and/or light losses in the optical part of the detector. Up to now, some studies were engaged in measurement of S(T)EM detectors performance ascertaining very low DQE for some detectors, but no suggestion has been made to optimize the detector set-up. To find the neck of a detection system, one must examine the whole detection path (Figure 1) step by step.

Electron-photon conversion optimization

The main component of a scintillation detector is the scintillator. The scintillator provides energy conversion from electrons to photons. It has to be very fast, possess high efficiency of electron-photon conversion, and it has to emit the light in the spectral region of high PMT sensitivity. To optimize the scintillator one must use a direct excitation method and measure its cathodoluminescent (CL) properties, i.e. its energy conversion efficiency, decay time and spectral emission characteristics. These CL properties can be measured using the equipment built in our laboratory [1]. The excitation unit of this equipment is formed by a column of an electron microscope with an electrostatic deflection system and a blanking diaphragm, so the continuous properties (CL efficiency) as well as kinetic properties (rise and decay times) can be measured. The equipment is controlled and the data are processed by a personal computer using IEEE-488 (GPIB) interface bus. Some tens of different single crystal materials were measured at our laboratory [2]. Of these, single crystals of YAG:Ce, YAP:Ce and P47 were chosen as the most interesting ones for S(T)EM applications. Alternatively, the transparent sintered YAG:Ce ceramics with optically good isotropy and pore-free structure (as presented by Ikesue [3]) seem to be interesting.

Optical properties optimization and PMT choice

In the separate step of optimization the materials of the light-guide, photocathode, conductive and reflective films and of the optical cement have to be evaluated. Optical characteristics (such as optical transmittance, position and width of the emission band, spectral response of and matching to PMT photocathode sensitivity) have to be utilized at this step of optimization. In fact, the PMT choice, including its photocathode matching, is a relatively simple task, because PMTs are well developed commercial components with precise data sheets.

Photon collection and system geometry optimization

Design of the system including geometry is the most demanding step of optimization. The efficient geometry is dependent on a lot of optical quantities of all components used, and no simple method is available for this step. To determine the photon transport efficiency, the Monte Carlo simulation method has been developed [4]. In Figure 2, the significance of this step of optimization is demonstrated by presenting the efficiency of the bad and good geometry of the BSE scintillation detector for the S 4000 Hitachi SEM. The good system possesses transport efficiency of about 400 % compared with the bad one.

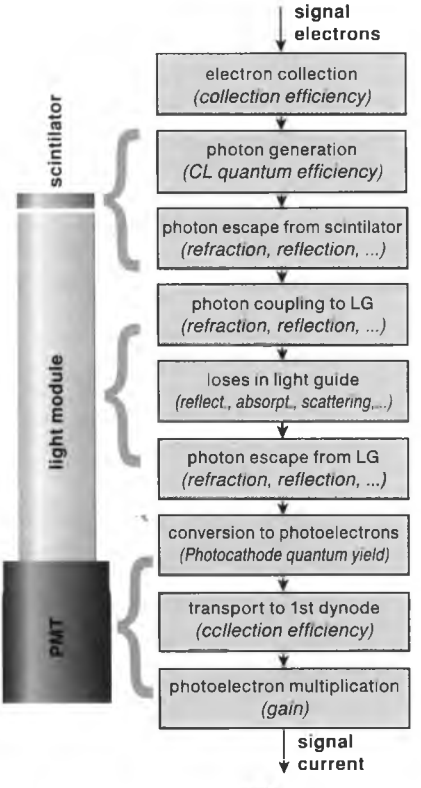

Fig. 1. Outline of detection path in a S(T)EM scintillation detector. To find the neck of a detection system, one must examine the whole detection path step by step using experimental and simulative methods for individual parts and/or assemblies of the detector.

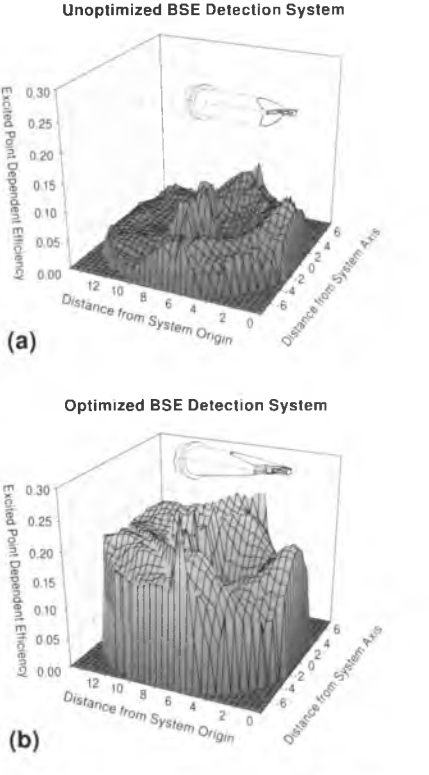

Fig. 2. Monte Carlo simulation of the efficiencies of the photon transport through scintillation detection systems possessing (a) the bad (b) the good geometry. 3D graph presents the dependence of the photon transport efficiency on the coordinates of the excitation point at the surface of the scintillator.

Detector configuration, position, and electron collection optimization

The previous steps of optimization are not related to the detector surrounding, which substantially influences collection of signal electrons. Interesting results of collection efficiencies of scintillation detection systems have been published using simulation of secondary electron trajectories [5].

This work was supported by the grant No. 102/04/2144 of the Grant Agency of the Czech Republic.

References

[1] Schauer, P.; Autrata, R.: *Proc. of ICEM 15*, Durban, South Africa, 2002, **Vol. 3**, p.337.
[2] Autrata, R. and Schauer, P.: *Scanning Microsc.* **Suppl. 9** (1996), 1.
[3] Ikesue, A. : *J. Ceram. Soc. Jpn.* **108** (2000), 1020.
[4] Schauer, P.; Autrata, R.: Proc. *EUREM 12*, Brno, Czech Republic, 2000, **Vol. 3**, p. I 455.
[5] Balasubramanyam, M.; Munro, E.; Taylor, J.: *Nucl. Instrum. Meth. Phys. Res. A*, **363** (1995), 270.

PICOSECOND DYNAMICS OF MAGNETIZATION PROCESSES OBSERVED USING TIME-RESOLVED X-PEEM

G. Schönhense, A. Krasyuk, D. Neeb, A. Oelsner, S. Nepijko, H. J. Elmers

Institut für Physik, Johannes-Gutenberg-Universität, D-55099 Mainz, Germany
(schoenhense@uni-mainz.de)

A. Kuksov, C. M. Schneider

Institut für Festkörperforschung IFF-6, Forschungszentrum Jülich, D-52425 Jülich, Germany

1. Introduction

The development of a dynamic imaging technique with time-resolution in the sub-nanosecond regime is driven by the need for methods to explore and control the fast dynamic response of magnetic thin film elements. This knowledge is paramount for industrial applications, e.g. for new magnetic storage devices such as hard disks with a greater storage density or magnetic RAM and spintronics elements. When the dynamic behaviour comes into play, high storage densities are inevitably correlated to fast data transfer rates and therefore short switching times of the order of a few nanoseconds down to below one nanosecond.

The majority of methods for magnetic imaging with high lateral resolution work on the basis of scanning-probe techniques. The sequential scanning of lines along the sample surface contradicts a high temporal resolution. There are optical methods to achieve the desired temporal resolution like magneto-optical Kerr microscopy, but the lateral resolution is limited by diffraction of light and therefore not sufficient to investigate devices with critical dimensions of the order of 100 nm. A highly promising approach is the method of X-ray excited photoemission electron microscopy (X-PEEM) because the required precise timing is achieved by exploiting the excellent time-structure of Synchrotron radiation. To our knowledge this method so far provides the fastest kind of electron microscopy with a resolution of presently 14 ps and potential of further improvement.

2. Experimental technique

As high-speed probe we employed short Synchrotron radiation pulses at BESSY (Berlin) and the ESRF (Grenoble) in the soft X-ray range. Very short probe-pulses down to $\Delta t \approx 1.6$ ps length were achieved in the novel "low-alpha" operation mode at BESSY [1], for many experiments the typical lengths of 50-100 ps of the standard modes proved to be sufficient. Fast magnetic field pulses have been generated by passing short current pulses through coplanar waveguide devices with magnetic structures being lithographically prepared on the stripline surface, see Fig.1. A stroboscopic pump-probe set up [2] with a variable delay (few ps step width) between field pulse and Synchrotron (probe) pulse allowed to take snapshots of the dynamic response of the magnetic domain structure as a function of delay time. X-ray magnetic circular dichroism XMCD yields magnetic contrast with the magnetization component along the photon beam (horizontal component) showing up as grey value [3].

Results presented in section 3 have been taken at moderate time resolution at the ESRF in 16-bunch mode (photon pulses 105 ps, period 176 ns), those of section 4 in the "low-alpha" mode of BESSY (1.6 ps pulses at a period of 2 ns). Permalloy (FeNi) structures were prepared on a Cu micro stripline. The current pulse I through the stripline gives rise to a magnetic field pulse H (cf. Fig. 1), determined in situ via a transient change of image size caused by the electric pulse when travelling across the field of view [4]. The rise time of the magnetic field pulse (more precisely, the slope of the temporal field profile) governs the dynamic response, because it determines the strength of the Fourier components in the frequency spectrum of the pulse. The slope was about 1 mT / 500 ps and twice that value in the section 3 and 4 experiments, respectively.

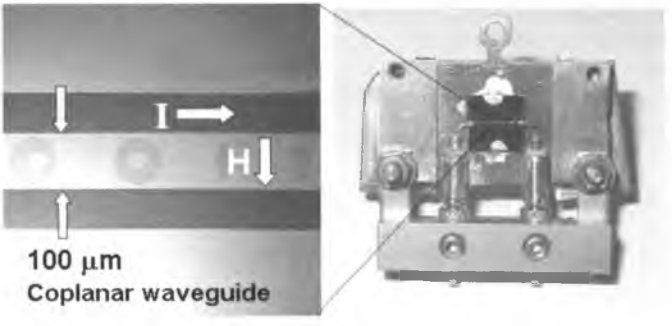

Fig. 1: *Optical microscope image of the coplanar waveguide with magnetic microstructures of Permalloy (left) and photograph of the UHV-exchangeable sample holder with microwave plugs (right).*

3. Coherent and incoherent magnetization rotation

Figures 2 and 3 show results for a microstructured Permalloy ring (80 μm o.d., 32 μm i.d., thickness 30 nm). The series of snapshots have been taken during application of a unipolar field pulse of about 2 mT amplitude and 7.5 ns duration. For reasons of intensity the exposure times were typically 120 s corresponding to averaging over 7×10^8 cycles. The 0 ps image reflects a metastable state after previous series of field pulses have been applied. The other snapshots correspond to the leading edge of the field pulse as marked in the pulse profile. Arrows denote the local magnetization direction, H indicates the field pulse, the photon beam is oriented horizontally. The simulated domain pattern has been obtained by a dynamical calculation based on the Landau-Lifshitz-Gilbert equation using the OOMMF code [5].

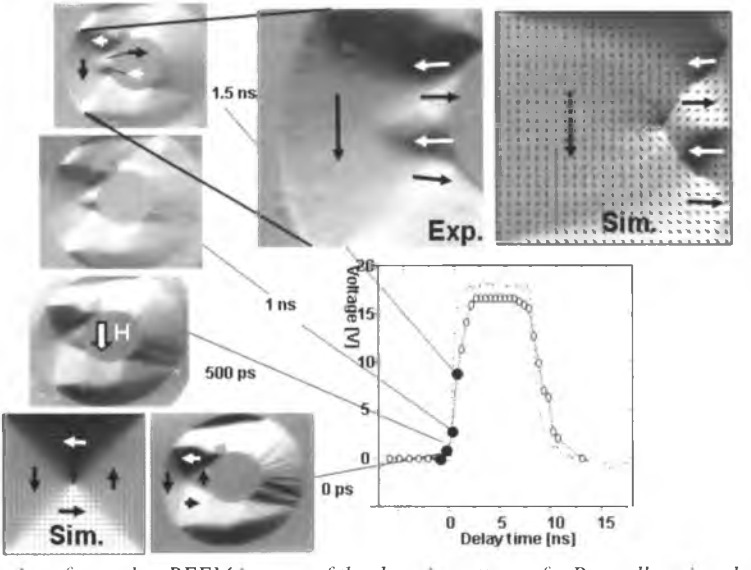

Fig. 2: *Series of snapshot PEEM images of the domain pattern of a Permalloy ring during the leading edge of a unipolar magnetic field pulse H. Magnetic contrast is due to XMCD at the Ni L_3 edge. (data from [4])*

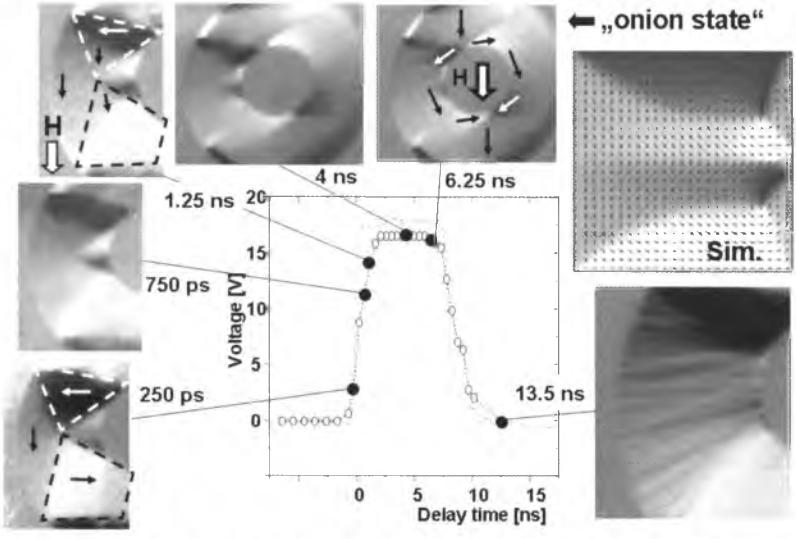

Fig. 3: *Same as Fig. 2 but taken during the plateau region and at the trailing edge of the magnetic field pulse. (data from [4])*

The Landau-type feature (flux closure structure, see lower left image in Figs. 2 and 3) visible on the left-hand side of the ring is disturbed by the field pulse resulting in an increase of the "down" domain, as anticipated from the field direction H. The "up" domain reacts by forming stripes perpendicular to H (see top images in Fig. 2). This behaviour was verified in the simulation and is obviously caused by the tendency to minimize the magnetic stray field energy in the transient state. In the plateau region the average grey level suggests a predominantly downward magnetization. The fact that the magnetic flux runs from top to bottom through the ring leads to the formation of a so-called "onion state" as indicated in the top row of Fig. 3.

Diffuse domain boundaries give evidence of deviations from a strictly periodic switching behaviour (averaging over 7×10^8 cycles in the stroboscopic mode). However, the structure always ends up in the same final domain configuration as is clear from the relatively sharp pattern at the foot of the trailing edge of the field pulse (right image in Fig. 3). Even at zero field the pattern is not yet fully relaxed, visible by comparison with the image at the foot of the leading edge. It shows characteristic stripes in the region of the Landau structure. Restoring the Landau pattern (driven by minimization of the stray field) obviously needs more time. The simulation reveals that this slow relaxation is caused by vortices being pinned close to the right hand side of the pattern; see "Sim." in Fig. 3. The simulated pattern is considerably smaller than the experimental structure so that the number of vortices is different.

4. Observation of magnetic modes

In the high time-resolution measurements at BESSY the field pulses were shorter and had a higher slope. At these conditions eigenoscillations of the magnetic structure, so-called magnetic modes are excited. The characteristic frequencies of these modes lie in the range of several GHz, i.e. their observation requires a time-resolution in the region of a few ps. Figure 4 shows first results revealing a magnetic mode in a Permalloy structure of 15 μm x 30 μm.

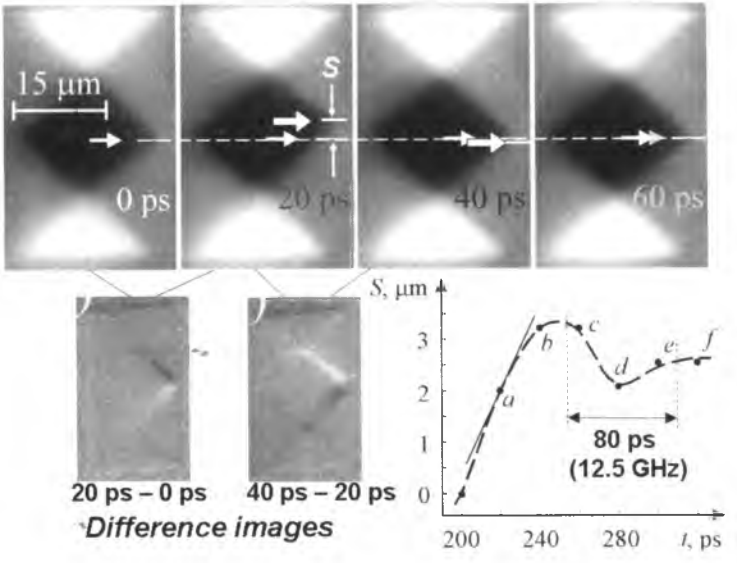

Fig. 4: *Snapshots of a magnetic mode, i.e. a domain oscillation at an eigenfrequency of about 12.5 GHz as estimated from the displacement curve S versus t.*

The diamond-shaped dark domain in the centre of the images exhibits a (damped) oscillation about its equilibrium position. The increment of the time-delay of 20 ps clearly was too large to follow the oscillatory movement of the domain boundary continuously. Only snapshots at certain times (i.e. certain phases of the oscillation) are visible.

In conclusion, we have presented novel results of an experiment for stroboscopic imaging of fast magnetization processes. The data at a time resolution of 125 ps reveal transient states due to dynamical effects on the sub-ns scale. A micromagnetic simulation could explain basic features that are absent in the slow-field-pulse (i.e. quasi-static) regime. The final example taken at improved time resolution (about 14 ps) gives evidence of a magnetic mode at an eigenfrequency of about 12.5 GHz. This result reflects the potential but also the present limitations of the method. The latter are not of principal nature but rather due to technical constraints that will be overcome in the near future.

References / Acknowledgement

[1] www.BESSY.de and K. Holldack, private communication
[2] A. Krasyuk et al., *Appl. Phys.* A **76** (2003) 863-868 and *Appl. Phys. A* (2004) publ. online 23 march; A. Oelsner et al., *J. Electr. Spectr. Rel. Phenom.* (2004) in print
[3] C. M. Schneider and G. Schönhense, *Rep. Progr. Phys.* 65 (2002) R 1785-1839
[4] D. Neeb et al., submitted
[5] M. J. Donahue and D. G. Porter, *OOMMF Users's Guide*, http://math.nist.gov/oommf/.

We thank the staff of BESSY and the ESRF for excellent support and cooperation. Financial support by BMBF (grants 05KS1UM1/5, 05KS1BDA/9 and 03N6500) as well as DFG through "Schwerpunktprogramm Ultraschnelle Magnetisierungsprozesse SPP 1133" is gratefully acknowledged.

THE ANALYSIS OF SIMION-7.0 FIELD ERRORS IN ION TRAP SIMULATIONS

Mikhail Sudakov* and Sumio Kumashiro

Shimadzu Research Laboratory Ltd.,
Wharfside, Trafford Wharf Road, Manchester, M17 1GP, UK
* corresponding author: m.sudakov@srlab.co.uk

In a typical ion trap operation cycle ions are trapped within fast oscillating quadrupole field for more than 10ms in presence of neutral buffer gas. Comparatively low voltage periodic excitation fields are used to excite motion of trapped ions mass selectively with the use of resonance phenomena. Ion trap performance in terms of resolving power and scan speed is sensitive to small distortions of trapping potential. Correct ion trap simulation should be able to reproduce accurately the effects of ion collisions with buffer gas and the influence of small deviations of the trapping potential from a pure quadrupole field.

The influence of several simulation parameters on the accuracy of ion trap simulation with the use of SIMION-7.0 was investigated. Prediction for the secular frequency of ion in a RF trapping field was used as a criterion of simulation accuracy. It was found that the secular frequency of ion oscillations with the use of SIMION potential arrays could differ from theoretical prediction by few percent. Three possible reasons for that were investigated: 1) insufficiently small integration step; 2) errors in electrical field interpolation from potential grid (numerical differentiation); 3) errors in field solution by finite difference (FD) method. It was found that simulation with the use of standard 4-th order Runge-Kutta procedure with integration step 0.01 of the RF period provides prediction for secular frequency with accuracy better than 1 ppm (in a pure quadrupole field). Errors due to numerical differentiation were estimated to be below 10ppm for geometries of practical interest. Finally investigation was concentrated on the quality of SIMION field solution.

Errors in field solution from SIMION appear from tree major factors: 1) field faults due to different boundary conditions; 2) errors due to finite difference approximation of Laplass operator; 3) errors due to stepwise approximation of the electrode shape. According to SIMION-7.0 manual [1] potential array is refined with "insulator" boundary conditions. Due to this SIMION cannot reproduce field solution accurately for problems with other boundary conditions such as, for example, "free space". Fortunately for ion trap simulations the area enclosed by electrodes is of importance. It was found that field faults due to incorrect boundary conditions for axially symmetric ion traps with hyperbolic electrodes (theoretical geometry) are below 5 ppm, provided that the size of the array covers at least 2ro, where ro is an inscribed radius of the quadrupole field. Errors due to finite difference approximation of the Laplass operator were estimated using a model of 2D quadrupole with circular electrodes. A 10-digit accurate field solution for the same problem [2] was used for comparison. Potential array was created with a step 0.01ro and grid potentials were assigned to correct values taken from accurate solution. In order to avoid boundary condition problems all boundary points were replaced by electrodes with potentials from accurate solution. Although the grid potentials in this case were correct to at least 10 digits the refine procedure is triggered by the difference between continuous Laplass operator and it's FD analogue. Potential array was refined with convergence objective of 1e-7. The absolute difference between accurate field solution and SIMION field was found to be below 5ppm within entire simulation volume. Finally, the errors due to the stepwise shape of electrodes were analysed. The same potential arrays as previously were used, but with electrode points assigned to constant voltages. By

comparison with accurate solutions it was found that the difference is proportional to a grid step and can be as big as few percent for rough arrays (grid step below 0.01ro). Field errors can be described as a combination of high order multipole components, which can be responsible for hardly predictable nonlinear phenomena in ion trap simulations.

An example of complete ion trap simulations for a Digital Ion Trap is provided.

As a result of analysis the SIMION field solution was found to be quite accurate for typical ion trap geometries, provided the grid step is sufficiently small. Field errors of FD method can be evaluated and taken into account in order to achieve prediction with accuracy over 100ppm. Simulation based on SIMION potential arrays can reproduce experimental situation better than simulation based on electrodes of perfect shape. At the same time user should be aware of possible nonlinear behaviour of ions with high vibration amplitudes, which may not take place in the actual instrument.

Literature

[1] D.Dahl, *Simion 3D Version 7.0 User's Manual*, Idaho NEEL, 2000, p.E1-E5

[2] M.Sudakov and D.Douglas, *Linear quadrupoles with added octopole field*, Rapid Comm. Mass Spectrom., **v.17**, 2003, pp.2290-2294

DESIGN OF THE LOW-VOLTAGE SEM

I. Vlček, B. Lencová and M. Horáček

Institute of Scientific Instruments, AS CR, Královopolská 147, 612 64 Brno, Czech Republic. E-mail: iv@isibrno.cz.

Our aim is to redesign the low-energy SEM (a scanning LEEM) in an UHV apparatus designed in our institute [1] to allow the detection of the angular distribution of signal electrons. For this purpose we have to separate the signal electrons from the primary beam with a Wien filter [2] and project the image of the back-focal plane of the objective lens on an area-sensitive detector (a back-illuminated CCD [3]). Therefore we have to design a new electrostatic optics working in UHV.

The arrangement of the key parts is shown in figure 1. The crossover of the primary 5 keV electron beam from a Schottky gun is imaged with the electrostatic objective lens/cathode lens on the specimen. For the beam scanning a two-stage deflection system is positioned in the lens. The beam aperture must be placed above the Wien filter so that it does not limit the signal beam.

The Wien filter is producing magnetic dipole fields with eight poles of equal size, which are electrically insulated and serve also as electrodes for electrostatic dipole field. This arrangement guarantees a perfect overlap of the two mutually perpendicular dipole fields. The Wien filter is stigmatic for the primary beam if we superimpose a suitable electrostatic quadrupole field on its electrodes. For our application the deflection of the signal beam can be as low as 15 degrees. Its minimum value is given by the requirement to position transport optics close to the Wien filter. By changing the orientation of the fields in the filter, it is possible to direct the signal on several detectors.

Another advantage of the Wien filter is that it has straight axis, so that the microscope can be operated with the filter switched off, e.g. in the standard SEM mode. The aberrations introduced by the filter are demagnified by the objective lens. In order to eliminate the effect of energy dispersion for high-resolution imaging, an intermediate crossover must be placed in the center of the Wien filter.

In the SEM mode the objective lens works as a unipotential lens and the conical shape of its outer electrode allows enough space in the sample region. In the low-energy mode we put high voltage on the insulated sample. The action of the cathode lens decreases the beam landing energy on the sample without much sacrifice on spot size. The values of image-side axial aberration coefficients on beam landing energy are given in figure 2 for the working distance 1.5 mm. With the cathode lens switched on, we have C_s=0.9 mm and C_c=0.15 mm at 100 eV, at 5 keV C_s=47.3 mm and C_c=18.3 mm, respectively. The signal electrons are accelerated into the lens and a diffraction pattern is formed in the back-focal plane. The back-focal plane is then imaged with transfer lenses on the CCD element used as a fast position-sensitive detector, whose output is then used to form the SEM image [4].

[1] I. Müllerová and L. Frank, Adv. Imag. Electron Phys. **128** (2003), p. 309.
[2] B. Lencová and I. Vlček in "Proceedings of the 12th European Congress on Electron Microscopy", ed. L. Frank and F. Čiampor, (CSEM, Brno) (2000) Vol. III, p. I87.
[3] M. Horáček, Review of Scientific Instruments **74** (2003), p. 3379.
[4] Supported by the Grant Agency of the Czech Republic, grant no. 202/03/1575.

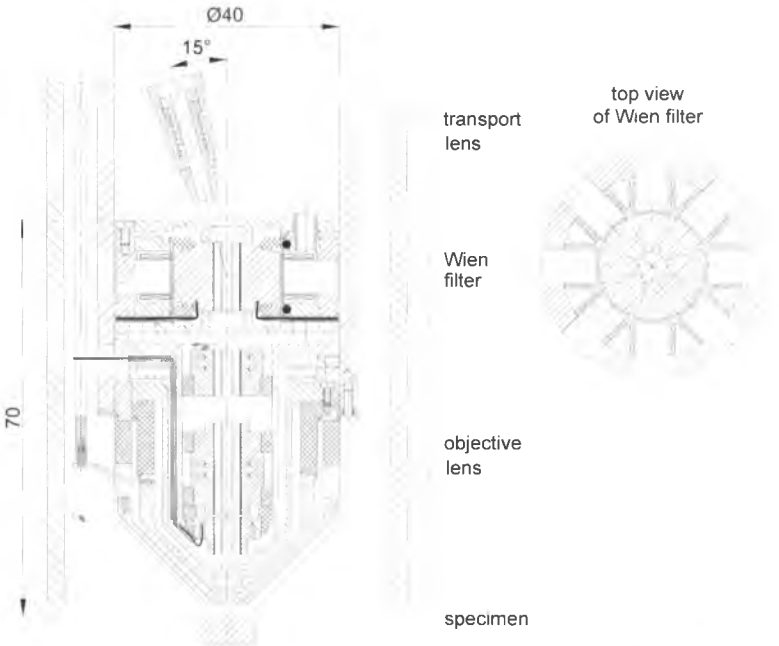

Figure 1. Key parts of proposed LESEM – the objective lens and the Wien filter as a separator.

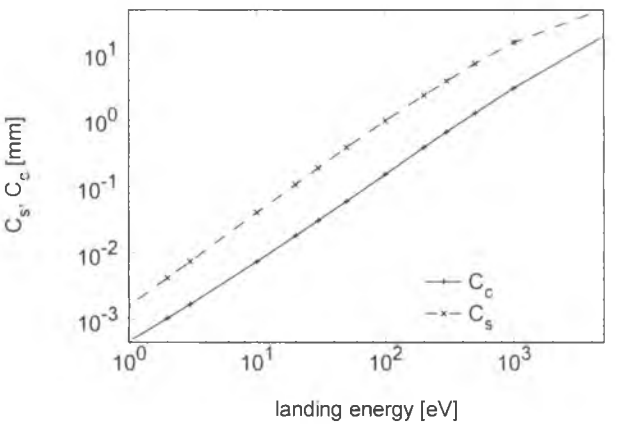

Figure 2. Dependence of the aberration coefficients Cs and Cc on landing energy for our objective lens (primary beam energy 5 keV, working distance 1.5 mm). The microscope resolution is expected 6 nm at 5 keV and 11 nm at 100 eV.

TRAJECTORIES OF SIGNAL ELECTRONS IN LOW-VOLTAGE BSE DETECTOR

P. Wandrol, R. Autrata

Institute of Scientific Instruments AS CR, Brno, Czech Republic, wandrol@isibrno.cz

Nowadays the development of the image formation in scanning electron microscope (SEM) is oriented to the use of scanning electron microscopes with low accelerating voltage of the primary beam (LV SEM).

Secondary electrons (SEs) for topographical contrast observation and backscattered electrons (BSEs) for material contrast observation are the main components of the detected signal in LV SEM. While the secondary electrons (SEs) can be detected either by Everhart-Thornley scintillation detector [1] or by the "in lens" SE detector, the detection of backscattered electrons (BSEs) in LV SEM is an unsolved problem yet.

The scintillator-photomultiplier detection system installed under the pole piece of the objective lens represents the most efficient BSE detector in SEM. However, the initial energy of the BSEs of 0.5-3 keV is the energy, on which the light yield of scintillators decreases. Therefore, it is necessary to accelerate the BSEs energy by electrostatic field before they reach the scintillator. By this electrostatic field both BSEs and SEs are accelerated to the scintillator and the image is a mixture of material and topographical contrasts. It is necessary to separate SEs by an energy filter or an immersion magnetic lens for the true material contrast observation.

The electrostatic field for the signal electrons acceleration is created by a high positive bias of 3-5 kV of the conductive layer, which is applied on the scintillator. The energy filter for the SEs separation is represented by a retarding grid with negative bias of around -100 V. This potential is sufficient to deflect the essential part of SEs. Another possibility of the SEs separation is the installation of the detector under the pole piece of an immersion magnetic objective lens, where the SEs are focused by a strong magnetic field into the objective lens and only BSEs are collected by the scintillator.

The described low voltage BSE detector and its electrostatic field was simulated by the software package Simion 3D [2] (see Figure 1). The scintillator covered by a conductive layer is placed in a shielding casing, below the scintillator is the retarding grid and the primary beam is shielded by a tube on a ground potential located in the hole in the centre of the scintillator. Figures 2 and 3 represent simulations of low energy BSE and SE trajectories in the electrostatic field of the detector. It is evident that the computed trajectories certify the theoretical predictions. When there is a bias of 3 kV is on the scintillator and a negative bias of -100 V on the grid, the BSEs, with their energies of 0.5-3 keV, are not affected by the negative bias of the grid and continue on straight trajectories to the scintillator (see Figure 2). SEs, with an energy of 5 eV, are deflected from the detector by an electrostatic field of the grid (Figure 3).

A strongly excited magnetic immersion objective lens is another possibility of SEs separation. The immersion objective lens, low voltage BSE detector and signal electron trajectories were simulated by software packages MLD, ELD and TRASYS [3]. A magnetic field created by this lens affects the SEs so that approximately 95% of SEs with an energy of 5 eV are focused on helical trajectories into the objective lens (see Figure 4) and there they can be detected by the "in lens" SE detector. BSEs are also influenced by this strong magnetic field, but owing to their higher energy, they are not focused into the objective lens. They are spinning around the primary beam trajectory and they can be detected by a low voltage BSE detector.

The study of BSE and SE trajectories demonstrated, that above mentioned detector can be used for the BSE deteetion in LV SEMs, which are not equipped by the immersion objective lens. Then it is necessary to apply a negative bias on the retarding grid. In LV SEMs with an immersion objective lens no bias on the retarding grid is needed.

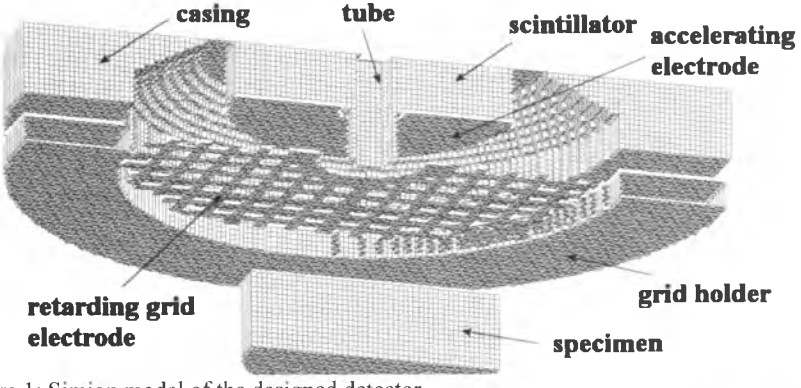

Figure 1: Simion model of the designed detector.

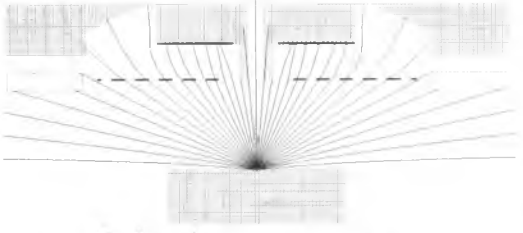

Figure 2: Trajectories of 1 keV BSEs. Electrode on the sintillator 3 kV, retarding grid -100V.

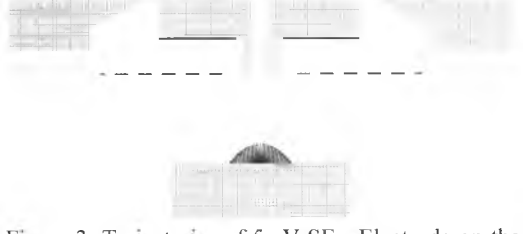

Figure 3: Trajectories of 5 eV SEs. Electrode on the sintillator 3 kV, retarding grid -100V.

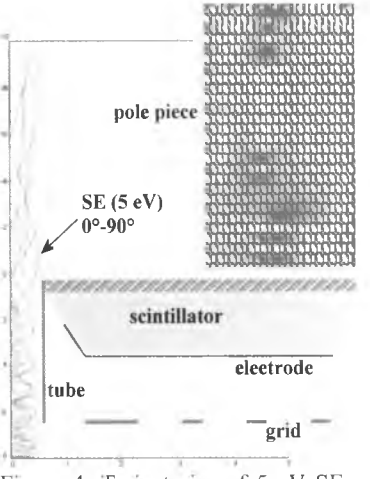

Figure 4: Trajectories of 5 eV SEs in the magnetic field of the immersion lens. Electrode on the scintillator 3 kV, retarding grid 0V.

[1] Everhart T. E., Thornley R. F. M.: Wideband Detector for Micro-microampere Low-energy Electron Currents. J. Sci. Instrum. 1960, vol. 37, p. 246-248.

[2] Dahl D. A.: Simion 3D version 6.0. In Proceedings of 43rd ASMS Conf. on Mass Spectroscopy and Allied Topics. Atlanta, 1995, p. 717

[3] Lencová B., Wisselink G.: Program package for the computation of lenses and deflectors. Nucl. Instrum. Meth. Phys. Res. A298. 1990, p. 56-66

[4] This work is supported by the Academy of Sciences of the Czech Republic, grant No. S2065102.

SIMULATION OF MULTIPOLE SYSTEMS BY DIFFERENTIAL ALGEBRAIC METHOD

Liping Wang, Haoning Liu, John Rouse, Eric Munro and Xieqing Zhu

Munro's Electron Beam Software Ltd, 14 Cornwall Gardens, London SW7 4AN, England
Tel & Fax: +44 20 7581 4479
E-mail: mebs@compuserve.com

Electrostatic and/or magnetic multipole elements are widely used in electron optical systems, which, in combination with round lenses, usually act as aberration correctors. Numerical simulation of multipole systems is very important in designing such systems. Here we present the differential algebraic (DA) method for aberration analysis of electrostatic and/or magnetic multipole systems. The DA method [1] is a smart and effective way to compute the aberrations of electron optical systems, theoretically up to arbitrary order, with very high accuracy. A novel technique, implementing this method using C++ classes, has been introduced by Wang et. al. [2] Recently, in order to simulate realistic optical systems, we have enhanced our DA software by combining it with Hermite fitting of the practical lens fields. [3]

The conventional method of analyzing aberrations of multipole systems is to first obtain the paraxial properties and then obtain the aberrations order by order by successive approximations. This involves enormous effort in deriving complicated aberration formulae, which will become increasingly unbearable. In 2002, an extensive aberration theory, up to secondary aberrations, for multipole focusing and deflection systems was developed by Liu et al. [4], which can handle systems consisting of electrostatic round lenses, electrostatic and/or magnetic multipoles, as well as deflectors. Recently, this theory has been extended to multipole systems including magnetic round lenses.

By contrast, the principle of the DA method is based on a non-standard analysis methodology. For the aberration analysis of electron optical systems, the core of the DA method is simply to trace a single ray. It is similar to conventional direct ray-tracing, but instead of on the conventional real space R, it is carried out on a non-standard extension of R, namely ${}_nD_v$, with the initial position, slope, etc. transformed as DA variables. The space ${}_nD_v$ has many remarkably similar properties to real space, but has some unusual and striking features, such as the existence of *infinitesimals*, which are *nilpotent*. [2] After numerically solving the general trajectory equation, the results are DA quantities which simultaneously provide information about the optical properties, including the aberrations, up to any required order. After performing the single raytrace, the aberration coefficients, in their conventional form, can be extracted from the DA quantities by simple algebraic formulae.

As an example, a multipole system including a magnetic round lens, four electrostatic quadrupoles and two electrostatic deflectors (as shown in Figure 1), has been calculated by the DA method, and the results have been compared with the results of the conventional aberration theory. In Table 1, the values of the third order imaging aberration coefficients are given, which shows that DA results agree with the conventional theory. The beauty of the DA method is that it is trivial to extend it to compute the higher order aberrations.

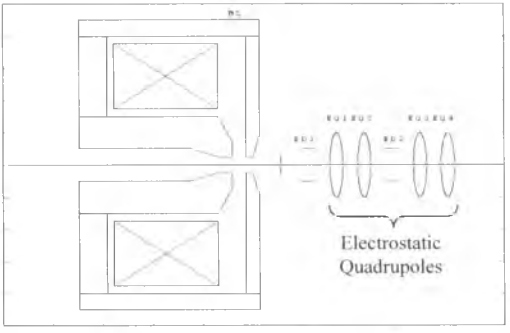

Figure 1. System with a magnetic round lens, four electrostatic quadrupoles and two electrostatic deflectors.

	Functional dependency	Aberration Integral results		DA results		Relative deviations
		Isotropic	Anisotropic	Isotropic	Anisotropic	
Aperture Aberrations	A A Ac	838.036	951.445	838.039	951.445	0.000250%
	A A A	0.000072	-0.000062	-0.00098	0.00090	-
	Ac Ac Ac	-392.729	-266.108	-392.725	-266.108	0.000927%
	A Ac Ac	-0.00021	0.00024	0.0016	-0.0026	-
					Average =	0.000588%
Coma	A A Bc	5962.41	6756.34	5962.42	6756.33	0.000197%
	A B Ac	11899.1	13535.3	11899.2	13535.3	0.000327%
	A A B	-349.593	236.88	-353.913	239.815	1.237%
	Ac Ac Bc	-8457.44	-5730.66	-8457.35	-5730.65	0.000893%
	B Ac Ac	298.513	-338.91	297.381	-337.629	0.379%
	A Ac Bc	567.388	-644.171	565.126	-641.613	0.398%
					Average =	0.336%
Field Curvature and Astigmatism	A B Bc	85044.5	96553.4	85046.8	96555.6	0.00244%
	A B B	-5019.02	3400.82	-5080.87	3442.81	1.233%
	A Bc Bc	4072.92	-4624.1	4056.59	-4605.59	0.4005%
	B B Ac	42431.7	48327.8	42431	48326.7	0.00202%
	Bc Bc Ac	-60868.4	-41243.7	-60866.2	-41242.6	0.00332%
	B Bc Ac	8358.6	-9489.74	8325.92	-9452.7	0.391%
					Average =	0.339%
Distortion	B B Bc	304554	346229	304564	346238	0.00294%
	B B B	-18029.1	12216.3	-18250.4	12366.5	1.228%
	Bc Bc Bc	-146401	-99199.6	-146388	-99191.7	0.0086%
	B Bc Bc	44662	-50706	44486.2	-50506.6	0.3934%
					Average =	0.408%

Table 1. Comparison of third order imaging aberration coefficients (in SI units).
(In functional dependency: $A=w_o'$=complex initial slope ; $B=w_o$=complex initial position; Ac= complex conjugate of w_o'; Bc= complex conjugate of w_o.)

References

[1]. M. Berz, *Particle Accelerators*, **24**, 109-124, 1989.
[2]. L.-P. Wang, T.-T. Tang, B.-J. Cheng et. al., *Optik*, **113**, 181-187, 2002.
[3]. L.-P. Wang, J. Rouse, H. Liu, E. Munro, and X. Zhu. *MNE 2003*, Cambridge, Sep 2003.
[4]. H. Liu, E. Munro, J. Rouse, and X. Zhu, *Ultramicroscopy*, **93**, 271-291, 2002.